Controlling Nanomaterial Assembly to Improve Material Performance in Energy Storage Electrodes

By

Landon Oakes

Dissertation

Submitted to the Faculty of the

Graduate School of Vanderbilt University

in partial fulfillment of the requirements

for the degree of

DOCTOR OF PHILOSOPHY

in

Interdisciplinary Materials Science

December, 2016

Nashville, Tennessee

Approved:

Cary Pint, Ph.D.
Rizia Bardhan, Ph.D.
Yaqiong Xu, Ph.D.
Jason Valentine, Ph.D.
Paul Laibinis, Ph.D.

ACKNOWLEDGEMENTS

I would like to express my biggest appreciation to my advisor, Prof. Cary L. Pint, for his excellent guidance, profound patience, and continual interest in my success.

I am also grateful to the members of my committee, Prof. Rizia Bardhan, Prof. Jason Valentine, Prof. Yaqiong Xu, and Prof. Paul Laibinis for their guidance, support, and excellent insight during the most momentous periods of my graduate career.

Thanks to my group members: Adam Cohn, Rachel Carter, Nitin Muralidharan, Anna Douglas, Keith Share, Andrew Westover, Mengya Li, and Shahana Chatterjee, without their many insightful suggestions my work would not by nearly the same quality it is today. Thanks also to the Rizia Bardhan group: Will Erwin, Joe Webb, and Holly Zarick for teaching me how to use all of their fancy chemistry equipment and for helping me gather data for many of my projects.

Thanks to all of the undergraduates that helped with this work: Trevor Hankin, William Yates, Dzul Zulkifli, Hafiz Azmi, JP Elizondo, and Jeff Holzgrafe for their dedication and continued assistance that greatly improved the quality and speed of the many projects contained in this dissertation.

I would like to thank all of the Vanderbilt Institute of Nanoscale Science and Engineering staff, specifically Ben Schmidt, Tony Hmelo, and Dmitry Koktysh for teaching me how to use many useful instruments and for taking the time to fix them after the many times I broke them.

A special thanks to Dan Fang for her patience as I worked for weeks on end, for her guidance in teaching me how to write good, and for her positive spirit that kept my life in Nashville fun and full of unforgettable experiences.

Finally, thanks to my family, the Oakes clan, for keeping life exciting and always reminding me to take time and enjoy the present. To my brothers for capturing me on weekends and forcing me to have fun, and to my sisters for always arranging the family gatherings that produced some fantastic memories. Thanks especially to my parents, for teaching me how to learn and instilling a passion for knowledge throughout my many years of homeschooling.

TABLE OF CONTENTS

Page

Chapter

Appendix

LIST OF TABLES

LIST OF FIGURES

LIST OF ABBREVIATIONS

ACN – acetonitrile
CNH – carbon nanohorns
CNS – carbon nanosheet
CNT – carbon nanotube
CV – cyclic voltammetry
DLS – dynamic light scattering
EIS - Electrochemical impedance spectroscopy
EMIBF4 - 1-ethyl-3-methylimidizolium tetraflouroborate
HOPS – high-order polysulfides
Li-ion – lithium ion
Li-O – lithium oxygen
Li-S – lithium sulfur
LOPS – low-order polysulfides
MoS_2 – molybdenum disulfide
NMP – 1-methyl-2-pyrrolidone
NS – nanosheets
OCV – Open circuit voltage
PMMA – polymethylmethacralate
R2R – roll-to-roll
SEM – scanning electron microscope
SWCNT – single-walled carbon nanotube
TMD – transition metal dichalcogenides
XPS – X-ray photoelectron spectroscopy
XRD – X-ray diffraction

LIST OF PUBLICATIONS

Portions of this dissertation have been drawn from the following publications:

1. **Oakes, L.**; Carter, R.; Muralidharan, M.; Pint, C.L., Isothermal Sulfur Condensation into Carbon Scaffolds: Improving Sulfur Loading, Performance, and Scalability of Lithium Sulfur Battery Cathodes. submitted to *Nano Letters*.

2. **Oakes, L.**; Carter, R.; Pint, C.L.; Controlled Defect Engineering of Lithium-Sulfur Battery Composite Cathodes for Improved Performance. submitted to *Nanoscale*.

3. **Oakes, L.**; Muralidharan, M.; Cohn, A.P.; Pint, C.L.; Morphology Matters in Electrode-Scale Catalyst Layers for Lithium-Oxygen Batteries. submitted to *Nanotechnology*.

4. **Oakes, L.**; Carter, R.; Hanken, T.; Cohn, A. P.; Share, K.; Schmidt, B.; Pint, C. L., Interface strain in vertically stacked two-dimensional heterostructured carbon-MoS_2 nanosheets controls electrochemical reactivity. *Nature Communications* **2016,** *7,* 11796.

5. **Oakes, L.**; Hanken, T.; Carter, R.; Yates, W.; Pint, C. L., Roll-to-roll nanomanufacturing of hybrid nanostructures for energy storage device design. *ACS Applied Materials & Interfaces* **2015,** *7* (26), 14201-14210.

6. **Oakes, L.**; Zulkifli, D.; Azmi, H.; Share, K.; Hanken, T.; Carter, R.; Pint, C. L., One batch exfoliation and assembly of two-dimensional transition metal dichalcogenide nanosheets using electrophoretic deposition. *Journal of The Electrochemical Society* **2015,** *162* (11), D3063-D3070.

7. **Oakes, L.**; Cohn, A. P.; Westover, A. S.; Pint, C. L., Electrophoretic stabilization of freestanding pristine graphene foams with carbon nanotubes for enhanced optical and electrical response. *Materials Letters* **2015,** *159,* 261-264.

8. **Oakes, L.**; Westover, A.; Mahjouri-Samani, M.; Chatterjee, S.; Puretzky, A. A.; Rouleau, C.; Geohegan, D. B.; Pint, C. L., Uniform, homogenous coatings of carbon nanohorns on arbitrary substrates from common solvents. *ACS Applied Materials & Interfaces* **2013,** *5* (24), 13153-13160.

9. **Oakes, L.**; Westover, A.; Mares, J. W.; Chatterjee, S.; Erwin, W. R.; Bardhan, R.; Weiss, S. M.; Pint, C. L., Surface engineered porous silicon for stable, high performance electrochemical supercapacitors. *Scientific Reports* **2013,** *3*.

CHAPTER 1

Introduction

A global energy dependence satisfied by renewable sources is essential to combat global warming and provide a self-sustaining energy economy. To accomplish this goal energy storage capabilities must be improved to satisfy the requirements of portable technologies and to use the intermittent energy produced by renewable sources efficiently. According to the International Energy Agency, a sustainable energy future requires at least three-fourths of all vehicle sales be electric by 2050, and an additional 150 GW of grid-scale energy storage be introduced o meet the expected demand from renewable energy production.[1, 2] Meeting these demands of a sustainable future requires the cost of energy storage systems be reduced while simultaneously improving the energy density.

The challenges presented by present-day lithium-ion (Li-ion) technology preclude such dramatic advances and demand entirely new materials and battery chemistries be implemented. Today's Li-ion technologies utilize a graphite anode and a layered transition metal oxide cathode with a limiting energy density of approximately 250 Wh/kg and a cost of production exceeding 400 $/kWh. As Table 1.1 shows, this performance falls drastically short of the required 350 Wh/kg at 100 $/kWh to make electric vehicles (EVs) competitive with traditional combustion engines. In order to overcome these limitations, laboratories around the world have been intensely researching new energy storage materials that go beyond the traditional graphite/metal-oxide systems and have demonstrated exceptional performance on the lab-scale that meet the required energy density of future battery systems. By moving to material systems with sulfur and oxygen as the active component, energy densities exceeding twice that of Li-ion batteries can be easily achieved and at a dramatically reduced cost. However, the use of these materials in battery electrodes presents an entirely new set of challenges for materials design and electrode manufacture that are not addressable through current material technology or fabrication processes. While the advent of nanomaterials adequately addresses the material challenges presented by sulfur and oxygen active materials, current methods of battery electrode manufacture are ill-suited to fabricate electrode materials capable of maximizing the potential of nanoscale materials when assembled into macroscopic films. In order to mitigate the degradation of material performance that results when nanoscale components are assembled into electrode-scale films, new methods of material manufacture must be developed that are both precise and cost-effective in nanomaterial assembly.

Table 1.1. Battery Performance metrics outlined by the United States Advanced Battery Consortium Goals for Advanced Batteries for EVs 2020 Commercialization.

Parameter (units)	**Goal**	**Current Level**
Specific Energy (Wh/kg)	350	250
Energy Density (Wh/L)	750	500
Calendar Life (Years)	15	10
Life Cycles	>1000	>1000
Selling Price ($/kWh)	100	400-500

1.1 Introduction to Battery Systems

Batteries store energy through chemical reactions and convert the stored chemical energy into electricity as a source of on-demand power. A battery consists of a positive (cathode) and negative (anode) electrode separated electrically by a separator and connected chemically by an electrolyte solution. A conventional Li-ion battery stores chemical energy by reacting lithium ions in the electrolyte with the anode during charge and with the cathode during discharge. The capacity of this system is limited by the total amount of lithium ions that can be stored in each electrode material, and the power density is determined by the rate at which these ions can be reacted.

The current limitation in energy density for commercialized battery systems stems from the low limiting capacity of the graphite anodes (~372 mAh/g) and metal oxide cathodes (~100-200 mAh/g) used to fabricate the full-cell battery (see Appendix A for details on battery performance metrics). Thus far, much research has centered on commercializing metallic lithium for use as the anode due to its high theoretical energy capacity of ~3,860 mAh/g, over 10x greater than current anode technology.[3] In order to fully realize the high capacity promised by elemental lithium, however, a suitable cathode material with comparable energy density must be implemented. For cathode materials, the frontrunners to replace traditional metal oxide materials are sulfur and oxygen, both of which have a theoretical capacity of ~1,675 mAh/g -- the highest of any cathode material reported to date. [4, 5] The mechanism of improved energy densities for these two new battery chemistries can be understood by considering the working principle of energy storage for each.

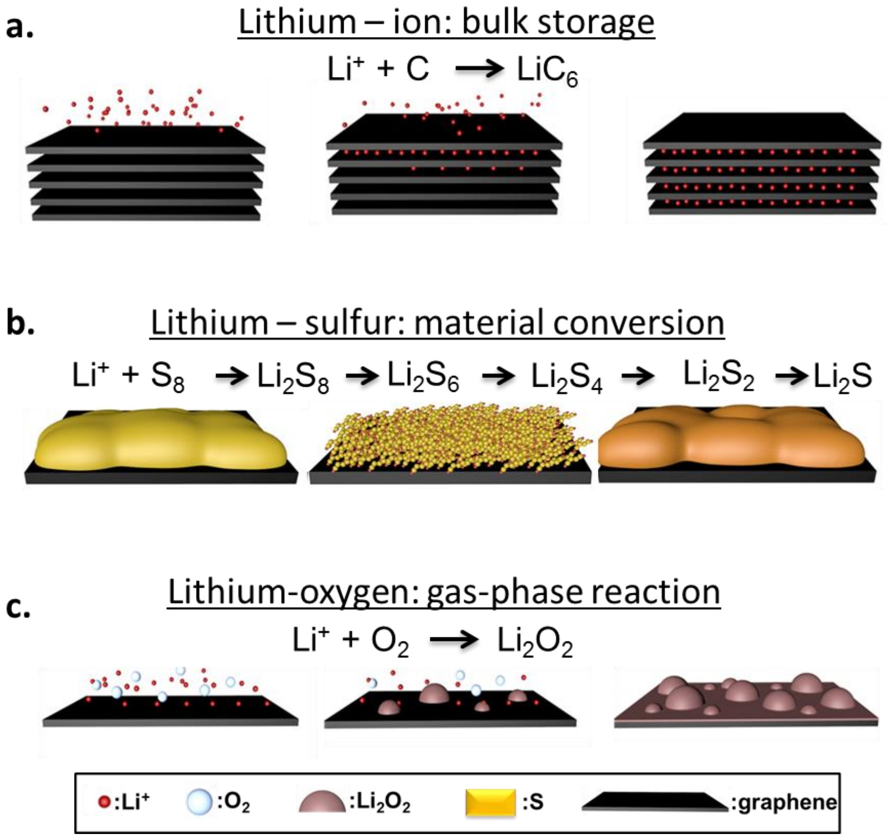

Figure 1.1. Schematic illustration of the working mechanisms for lithium-sulfur and lithium-oxygen batteries, two systems currently under investigation to replace lithium-ion batteries.

1.2 Challenges in Li-S and Li-O systems

Figure 1.1 above represents schematically the nature of charge storage in both lithium-sulfur (Li-S) and lithium-oxygen (Li-O) systems. The working principles of both Li-S and Li-O batteries rely on a chemical conversion process in which the mechanism of lithium storage dramatically changes both the morphology and the chemistry of the fully reacted electrode material. In the case of Li-S systems, a complex multi-phase reaction generates a whole host of intermediary reaction products with unique structures and chemistries compared to the initial elemental sulfur starting material, all of which culminates in the formation of an insulating lithium sulfide discharge product. In Li-O systems, an initially gaseous oxygen cathode is converted into a solid product of lithium peroxide through subsequent reductions of the oxygen molecules. These working mechanisms differ drastically from traditional Li-ion batteries in which the capacity is limited by the ability of the bulk structure to accommodate intercalated or alloyed lithium ions and does not require any intermediary phase changes or the formation of electrically insulating discharge products. The working mechanisms of traditional bulk systems severely limit their storage capability, as graphite is capable of storing only one lithium ion for every six carbon atoms, and a traditional metal oxide cathode (e.g. $LiCoO_2$) can only store one lithium ion for every two molecules of the cathode. In Li-O and Li-S systems, however, these performance limitations are overcome by a conversion reaction process that enables every atom of the active material to be paired with one or more lithium ions, thereby dramatically improving the energy densities of these systems.

Unfortunately, the discharge products that enable such exceptional energy densities are heavily insulating, and intelligent material design is needed to pair these materials with a conductive current collector that is capable of retaining sufficient electronic conductivity of the composite during operation. Unlike traditional Li-ion batteries, which react the bulk of an already conductive material to host lithium ions, the chemical conversion process required by Li-S and Li-O batteries rapidly deactivates material that is not in simultaneous contact with both the electrolyte and the current collector.

In order to maintain the necessary interconnectivity within the composite during the conversion process and its associated volumetric expansions and contractions, interfacial contact between the current collector and the active material components must be controllably maximized. In this regard, nanomaterials represent the most promising candidate to achieve the complete utilization of a given active material, since their high surface-area-to-volume ratio enables sufficient interfacial contact during conversion processes. Additionally, the conductive current collector material which interfaces with these materials must be chosen carefully to preserve the exceptional gravimetric performance promised by these unique material chemistries. On this front, carbon nanomaterials are the material-of-choice due to their exceptionally high conductivity, low weight, chemical inertness, and the recently developed ability to manufacture few- to single-atom thick structures of these materials on the large scale. Thus, the ideal electrode composite to maximize the potential of these next-generation battery chemistries is comprised of a collection of nanoscale sulfur or oxygen electrocatalyst material optimally interfaced with a conductive carbon network.

The fabrication of such a material system requires a controlled assembly approach that exercises fine control over individual particle placement in order to construct macroscopic films that maintain a high surface area of active material in contact with the liquid electrolyte and while remaining anchored to a conductive carbon substrate. Such fabrication presents three primary manufacturing challenges: (1) the fabrication of a high surface area carbon current collector, (2) controllable integration of active materials with the assembled current collector that preserves the properties of the carefully engineered nanoscale components, and (3) the ability to satisfy both of these conditions on a large-scale, high-throughput system. Addressing these three manufacturing challenges is the focus of this dissertation, which presents a technique for manufacturing improved Li-ion, Li-O, and Li-S electrodes from nanomaterials on a large-scale, high-throughput system.

1.3 Challenges in Assembling Nanoscale Electrode Materials

The practical incorporation of nanostructured materials into emerging applications such as energy storage systems is limited by the challenge of achieving low-cost, high-throughput, and highly replicable scalable nanomanufacturing techniques to produce functional materials. Liquid-phase processing presents a promising approach to control the assembly of nanomaterials due to its ability to effect single, isolated nanomaterials in bulk quantities. With the correct choice of solvent or solution additive, individual structures with different compositions may be suspended together homogenously in solution, thus providing the ideal starting condition for film assembly. However, in order to maximize the solubility of nanostructures, the mechanism of solubilization must be preserved until the moment of film formation in order to preserve the carefully engineered solution properties and ensure an acceptably homogenous mixture of nanomaterials within the film that closely mimic those in solution.

A description of the nanomaterial suspension process will illustrate the intermolecular forces available to ensure solubility and direct particle assembly. Traditionally, colloidal stability has been described using the DLVO theory, named after the scientists that formulated the theory, Derjaguin, Landau, Verwey, and Overbeek.[6] DLVO theory ascribes colloidal stability to the delicate balance between electrostatic and van der Waals interactions that occur between two particles in the same solution system (Figure 1.2). Electrostatic interactions are provided by the charge imparted on the surface of a particle as electrochemical equilibrium is established within the suspending solution through numerous charge transfer reactions. Van der Waals forces are engendered by the fundamental dispersion forces that attract any two materials together due to the fluctuating or permanent dipoles present on the atomic level. In a solution, if the repulsion between like particles is greater than the attractive force, the suspension is considered stable.

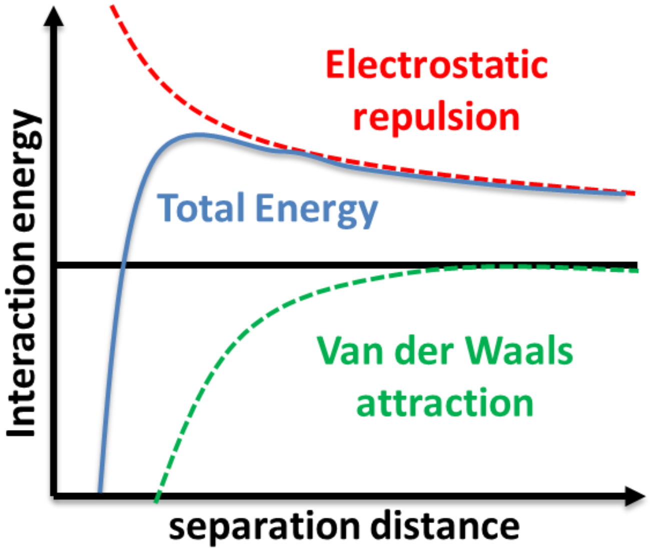

Figure 1.2. Graphical representation of the intermolecular forces present in solution. When the interaction energy is positive, suspended materials repel each other and contribute to a well-dispersed solution. When the interaction trends toward negative values, attractive forces dominate and aggregates of material are formed within solution.

Charged surfaces on a particle may occur through a number of mechanisms, including the dissociation of surface groups, charge-transfer reactions with the solvent molecules, selective solubility of individual components, or the introduction of polymer functional groups. Using these mechanisms, electrostatic charges may be controllably imparted to a particle during the formation of a suspension. In order to maintain isolated, well-dispersed nanostructures in solution, the concentration of material within the suspension must remain low enough such that the electrostatic repulsion between particles presents a suitable barrier to the statistically dependent aggregation stemming from the thermal motion of particles in solution. Thermodynamics dictates this limiting concentration, since an increase in the number of particles drives an increase in the free energy of the solution/solute system that may be reduced through the formation of aggregates. True solutions of nanomaterials are obtained when the enthalpy of mixing, for a specified amount of nanomaterial, remains negative. Recent work in applying well-known polymer suspension solubility rules to the solubility of nanomaterials has identified a concentration-dependent aggregation limit that may be determined by the solvent properties in conjunction with the volume fraction and aspect ratio of the suspended nanomaterials.[7-9] For nanostructures such as single-walled carbon nanotubes (SWCNTs), this solubility limit can be as low as 20 mg/l of solution.[10] However, traditional techniques for film formation, such as a dip-coating or blade-casting, that are currently used in industrial settings to coat battery materials require highly concentrated suspensions of active material that exceeded 20 g/l; these techniques are known to result in severe aggregation and local viscosity disturbances that inhibit the homogeneity of the assembled material and the uniformity with which it is spread onto the electrode. A recent, thorough investigation of the effect these defects in film formation have on the electrochemical performance of battery electrodes has emphasized the dramatic shortcomings of current battery manufacturing methods in addressing the fabrication challenges present for next-generation energy storage systems.[11] Therefore, a new approach is required to assemble well-dispersed mixtures of nanomaterials for Li-S and Li-O electrode architectures. The ideal technique to accomplish this assembly should utilize the molecular forces inherent to dispersions of nanomaterials in order to assemble thick films of material from well-suspended solutions and to maintain the solubility of the nanostructured materials up until the point of film formation.

In this regard, an assembly approach that harnesses the electrostatically charged surfaces of nanomaterials in solution represents an attractive approach to accomplish this formation of nanomaterial films. By electrostatically directing the assembly of individual nanoscale components, conformal coverage across large areas of a conductive surface may be achieved, and the relatively dilute suspensions of nanomaterials that are required to ensure acceptable solubility can result in the assembly of meaningful masses of materials onto electrodes regardless of the initial concentration in solution. Additionally, the motion of particles along electric field lines enables this coating process to be applied to arbitrary substrate geometries. Assembling particles from solution in this manner is referred to as electrophoretic deposition (EPD) and will be a primary focus throughout the remainder of this thesis.

1.4 Introduction to EPD

EPD is a widely used coating technique due to the exceptional control, when compared with conventional coating processes, that can be exercised on an individual particle level for materials suspended in a liquid. EPD enables additive-free manufacturing of materials into complex substrate geometries with fine control over film thickness, composition, and formation rate. Common industrial applications of EPD involve the coating of auto body parts or the formation of ceramic coatings on geometrically complex substrates; however, the utility of this approach as it applies to nanomaterial suspensions is only beginning to receive widespread attention.[12] EPD offers all of the desirable qualities inherent to traditional liquid-phase manufacturing, but with the added benefit of single-particle control and site-selectivity. These unique advantages enable the formation of lightweight, high-surface-area materials that are ideally suited for energy storage applications. The method begins by dispersing a material in a solution and then uses an electric field to move the particles into a desired arrangement on the electrode surface. There are three steps in the EPD process: (1) formation of a stable suspension of particles, (2) migration of the particles toward the depositing electrode through the application of an electric field, and (3) deposition of the particles on the electrode surface. A schematic of these steps in the EPD process is presented in Figure 1.3.

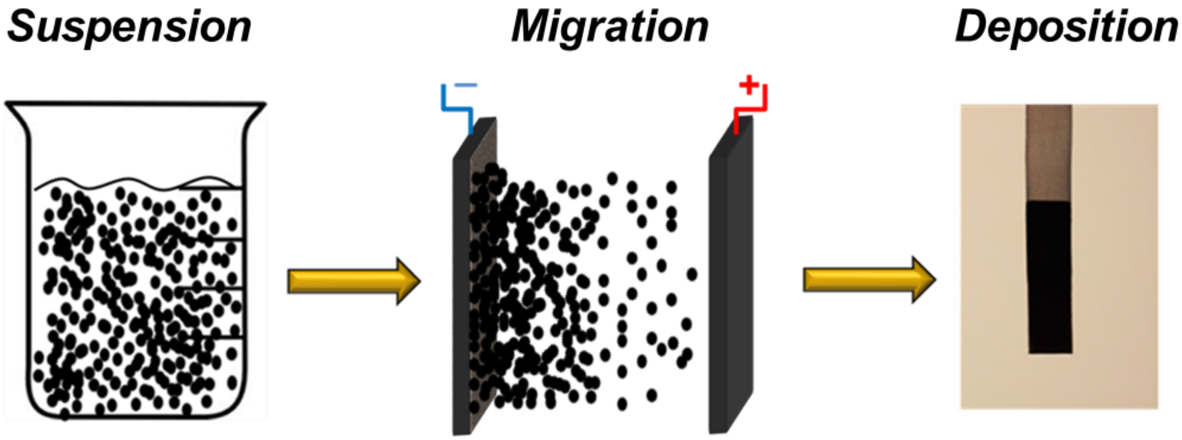

Figure 1.3. Schematic illustration of the EPD process highlighting the three steps that require careful process engineering to accomplish effectively.

1.5 Solution Formation

The first step in the process of EPD is important for all methods of liquid processing: the formation of a suspension of particles. The primary difficulty in forming a suitable suspension arises from the attractive forces between particles suspended in a solution that seek to precipitate out large aggregates. Due to the difference in dielectric properties between the particles and the solvent, there exists a short-range attractive dispersion force (a.k.a van der Waals force) between the particles that causes particles which pass within a few nanometers of each other to cohere with sufficient energy relative to the thermal energy of the solvent that strives to break them apart. For this reason, a stabilizing force is needed to keep the particles separated in solution. There exist two primary mechanisms for producing this stabilizing force, namely electrostatic and polymeric stabilization.

Electrostatic stabilization requires a charge separation between the dispersing solvent and the surface of the suspended particles. The charged surface of particles in solution creates a layer of polarized solution immediately surrounding the particle that provides a net repulsive force when two particles with similarly polarized surfaces approach each other. On the other hand, polymeric stabilization uses a polymer coating on the suspended particles to screen the attractive dispersion forces that exist between like particles in solution. This method relies on a polymer coating that has dielectric properties similar enough to those of the solvent to prevent sufficient attractive forces between polymer coatings. Typically, a dissociation of functional groups on the polymer ends provides a sufficient build-up of electric charge to make these particles susceptible to migration under the influence of an applied electric field.

1.6 Migration and Deposition

In order to measure the charge imparted to materials in suspension, dynamic light scattering (DLS) techniques are implemented to measure the mobility of particles under the application of a known electric field and, provided with appropriate solution parameters, can calculate an important quantity known as the zeta potential. The zeta potential, used to estimate the stability of a given solute-solvent system, is an indirect measurement of a particle’s surface charge when in equilibrium with the surrounding solution. The charged surface of a particle attracts subsequent layers of oppositely charged ions in an immediately adjacent region of solution through the formation of what is commonly referred to as “the double layer.” A schematic illustration of this double layer formation is presented in Figure 1.4. As a particle moves through solution, a portion of the double layer remains in contact with the particle while the rest is carried away due to retardation effects that vary with solution composition. The zeta potential measures the difference in electrostatic potential between the surface of the particle and the surface of shear within the double layer. This value is directly proportional to the mobility of a particle as it pertains to the EPD process. Values exceeding +/- 30 mV are considered to be stable, mobile solutions while values less than this typically result in particle aggregation and poor assembly kinetics.

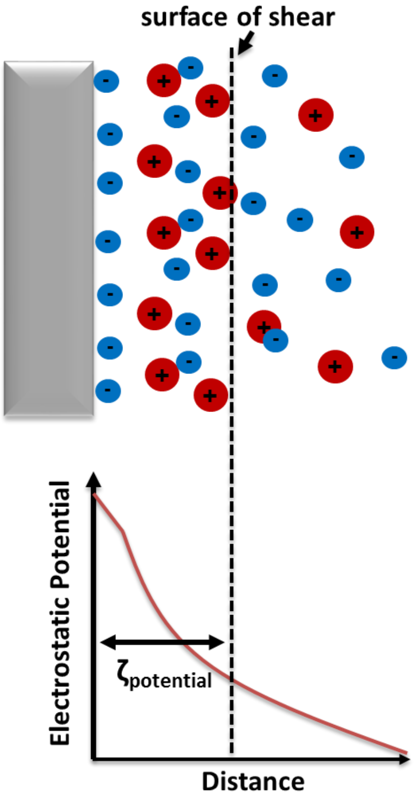

Figure 1.4. Schematic illustration of the zeta potential. The potential measured at the surface of shear as the particle and the surrounding double layer move through solution is referred to as the zeta potential.

After formation of a suitable suspension, charged particles are exposed to an applied electric field to achieve migration in a desired direction. When an electric field is applied to the suspension, charged particles migrate towards the oppositely charged electrode and accumulate in concentrations that greatly exceed those present in the bulk of the solution. In order to achieve deposition onto the electrode surface, the interparticle repulsion that maintains the stability of the suspension must be overcome. To accomplish this stability, a number of processes occur simultaneously to contribute to the nucleation of a compact, solid film directly from the solubilized state. The exact working mechanism for a specific particle type and solvent composition varies greatly from system to system; however, deposition universally occurs as a result of four main processes. A schematic illustration of the processes contributing to deposition is depicted in Figure 1.5.

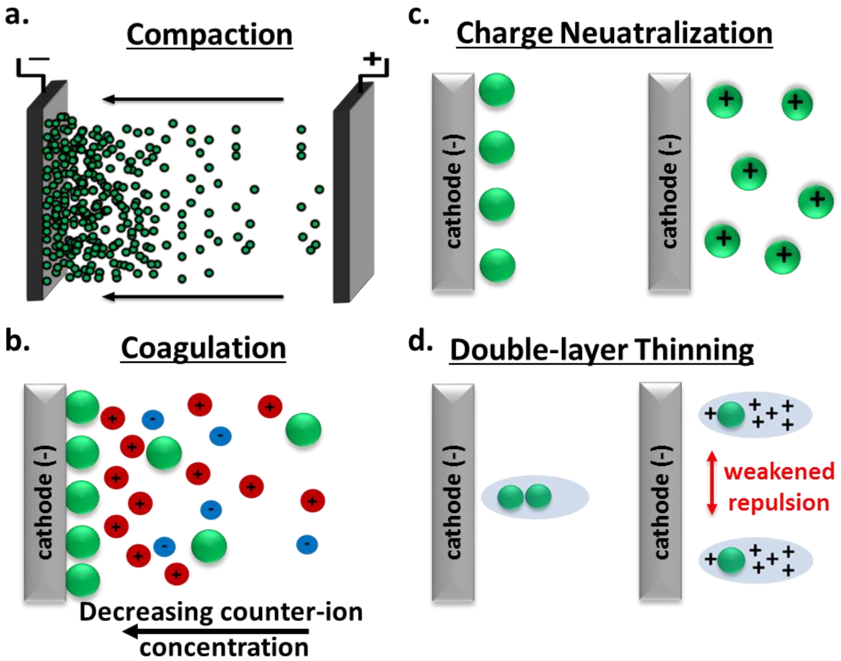

Figure 1.5**.** Mechanisms of depositions during EPD. Film formation as a result of (a) the increase in nanomaterial concentration near the electrode surface, (b) electrolyte concentration changes near the surface of the electrode, (c) charged particle neutralization on the surface of deposition and (d) double layer distortion as a result of the applied electric field.

The first process, flocculation by particle accumulation, can be understood as an electric-field driven sedimentation process. As particles accumulate at the surface of the electrode, pressure exerted by particles on the outermost regions of the accumulating deposit results in sufficient force to overcome the interparticle repulsion in the innermost layer resulting in deposition from solution (Figure 1.5a). The second process, electrochemical particle coagulation, occurs as a result of electrolyte concentration changes near the electrode surface (Figure 1.5b).

Due to the presence of an electric field, ions of opposite charge are present in drastically diminished concentrations near the surface of the electrode when compared with the bulk, thereby hindering the ability of a charged surface to form a double layer in solution. The third and more obvious contribution to film formation is charged particle neutralization (Figure 1.5c). This process typically occurs with conducting particles in solution and refers to a neutralization of the particle surface from direct contact with the oppositely charged electrode. This neutralization of charge inhibits the magnitude of electrostatic repulsion between particles and promotes film formation. Finally, the effects of the electric field on ion concentrations within the double layer change the magnitude of repulsion locally between two particles by changing the shape of the surrounding double layer (Figure 1.5d). As a particle and its double layer approach an electrode surface, ions of opposite sign are attracted toward the electrode while those of same sign are repelled, resulting in a thinning of the double layer on surfaces parallel to the electrode surface. As a result of these competing processes that stem from the application of an electric field, particles in solution are able to transition from a fully solubilized state to an assembled film state within the vicinity of the deposition substrate.

1.7 Conclusion

The ability to solubilize homogenous dispersions of nanomaterials represents an attractive approach for nanomanufacturing. Traditional film coating processes are not equipped to assemble nanomaterials, for they have little-to-no control over individual particle placement and often implement concentrations exceeding the solubility limits of nanomaterials. EPD addresses these shortcomings and is the superior method of film fabrication for nanomaterial composites. EPD utilizes the mechanism of solution stability as the driving force for assembly by harnessing the power of electrochemical equilibria to drive film formation. Using this approach, homogenous films of nanomaterials may be assembled from solutions ideally engineered for nanomaterial assembly.

1.8 Thesis Organization

In this thesis, I present a method for the controllable manufacture of nanomaterials that enables the production of energy storage electrodes. Through solution engineering, I stabilize homogenous dispersions of multi-component solutions and utilize the mechanism of stabilization to assemble films directly from solutions that contain a controlled mixture of conductive and active nanomaterials. By applying these films as electrodes in Li-ion batteries, I demonstrate the scaleable fabrication of material systems using the process of EPD that outperform traditional Li-ion battery materials. Similarly, I find that the use of EPD can result in the creation of Li-S and Li-O electrode materials that outperform identical materials fabricated through conventional approaches.

In Chapter 2**,** I use EPD processing to assemble carbon nanomaterial films and develop models to simulate this EPD process. Through a careful consideration of solution parameters near the electrode surface, I present models that accurately predict the assembly kinetics of both single- and multi-component solutions. This chapter concludes by using EPD to engineer all-carbon electrodes with tunable reactivity in an electrochemical system.

In Chapter 3**,** I extend the results of Chapter 2 to demonstrate a scaleable assembly process based on EPD that produces electrodes directly from solution using a high throughput roll-to-roll (R2R) system. Both anode and cathode materials can be fabricated by applying this system to an engineered solution comprised of carbon nanomaterials and high-capacity Li-ion battery materials. Specifically, using silicon nanoparticles and MoS_2 nanosheets, a full-cell lithium ion battery can be fabricated in less than 30 seconds via this R2R platform that significantly outperforms traditional Li-ion battery materials.

In Chapter 4**,** as a cost-effective solution for nanomaterial assembly, I present a method to produce functional films of 2-D nanosheet materials, such as the cathode films of MoS_2 from Chapter 3, directly from bulk starting materials. . By implementing a one-batch synthesis and assembly process, I achieve the fabrication of films with a meaningful mass of material when starting from purified, ultra-dilute solutions of a tunable size distribution. Through the correct choice of solvent, optimized liquid-phase exfoliation processes of bulk transition metal dichalcogenides are engineered with optimized EPD assembly kinetics to produce cost effective assemblies of nanostructured Li-ion battery cathode materials.

In Chapter 5**,** I apply novel methods of strain engineering to the MoS_2 materials fabricated in Chapter 4 in order to optimize the performance of these films in full-cell Li-ion batteries. Through the application of an ultrathin carbon layer, interfacial strain is harnessed to modulate the energetics of the MoS_2 conversion reaction in order to make these materials compatible with conventional anodes. Using this approach in combination with the results of Chapters 2-4, I demonstrate how EPD assembly can be used to produce lithium-ion battery anode and cathode materials with superior electrochemical properties compared to present-day Li-ion technologies.

Chapter 6 demonstrates the potential of this EPD technique to tackle the challenges presented by next-generation energy storage systems by introducing the capability of EPD to fabricate 3-D freestanding structures of carbon nanomaterials that can serve as scaffolds for active electrocatalyst or sulfur species. EPD can be used to stabilize graphene foam structures by coating an optimally thick layer of SWCNTs conformally on the surface of the foam structure. Comparing this method of stabilization with traditional methods incorporating polymer stabilizers demonstrates how these all-carbon materials are ideally suited for electrochemical applications.

Chapter 7 extends these results to Li-O systems by producing optimized cathode materials through the integration of nanoparticle electrocatalyst assembly with the fabrication processes developed for 3-D nanocarbon structures. The use of EPD in assembling the catalyst layer generates improved characteristics when compared to conventional dip-coating processes. In-situ electrochemical impedance measurements elucidate the mechanism of improvement and demonstrates that the use of EPD in catalyst film assembly results in more compact, interconnected structures that retain their macroscopic interconnectivity upon repeated cycling of the Li-O battery.

Chapter 8 introduces the utility of this approach for Li-S batteries. Through the development of a novel sulfur-coating technique, I demonstrate a mechanism whereby an optimized carbon current collector may be interfaced with sulfur films in order to fully utilize the morphology of the nanocarbon structure. By using capillary condensation to nucleate the coating of sulfur films, sulfur material is placed within geometrically and chemically favorable locations on the carbon surface. Using this approach, cathode materials are found to exhibit improved capacity and cyclability in comparison with cathodes of identical composition assembled using a conventional melt-infiltration process to produce the sulfur film.

Finally, in Chapter 9, I apply the novel coating process developed in Chapter 8 to all-carbon films assembled using EPD. By using hybrid depositions of graphitic and reactive carbon nanomaterials, the chemistry of the carbon skeleton is optimized to produce one of the best performing Li-S cathodes ever reported. The integration of this novel coating process with the R2R assembly approach of Chapter 3 foretells the exciting manufacturing capability of this nanomanufacturing system.

CHAPTER 2

Manufacturing Carbon Nanomaterials

2.1 Introduction

The most basic component of any energy storage system is the conductive material that enables the collection or transfer of current produced by the device. In order to optimize the energy density of these systems, the weight of conductive material must be minimized while preserving mechanical and electrical interconnectivity. Carbon nanomaterials, which are exceptionally conductive, lightweight, and mechanically strong, excel as a current collector material and are ubiquitous in battery materials today. Current Li-ion batteries contain an anode comprised solely of graphitic carbon and a cathode containing insulating metal oxide particles interfaced with a conductive carbon network. These material systems exhibit an energy storage capacity dependent on the morphology and chemistry of their carbon structures. When manufacturing Li-ion battery materials on a large scale, the precise assemblage of carbon structures over large areas is essential for maximizing the energy storage capacity of engineered electrode materials. In particular, the capacity obtained by next-generation Li-S and Li-O batteries is particularly sensitive to the design of the carbon network that interconnects the insulating sulfur and electrocatalyst species. The advent of carbon nanomaterials has enabled the production of electrodes with comparable energy densities to fossil fuels; however, in order to maximize the energy density in these systems, the morphology and chemistry of the carbon component must be carefully controlled.

The recent development of a wide array of carbon nanomaterial chemistries and structures presents a unique opportunity to optimize the carbon structure for a specific application. Depending on the application, the presence of a reactive or inert carbon surface is required while maintaining an electrically conductive matrix. The reactivity of carbon materials may be controlled through the concentration of defects or edges on the carbon surface. Edge sites and defects in the carbon structure terminate with a more reactive sp^3 hybridized carbon-carbon bond due the local coordination of these atoms in the carbon lattice. These sp^3 sites react with oxygen-containing chemical groups when left under standard atmospheric conditions resulting in the formation of a functionalized, polar surface. Thus, by tuning the defect density in these carbon structures, both the conductivity and reactivity may be controlled.

Substantial advancements have been made in fabricating highly graphitic or highly reactive carbon nanostructures in bulk-scale quantities. By combining a controlled amount of these various optimized structures together in a composite, the defect content of the entire assembly may be controlled. Table 2.1 presents a representation of some of the most common forms of carbon nanostructures and highlights the properties of these materials that may be harnessed for battery applications. Depending on how these materials are assembled together, it is possible to design composites with a specified degree of conductivity, reactivity, or mechanical interconnectivity through a tuning of the ratio of the selected carbon structures.

Table 2.1 Properties of the most common forms of carbon nanostructures with additional columns depicting mixtures of these materials optimized for a specific application.

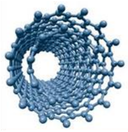

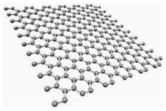

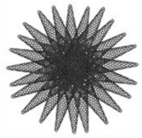

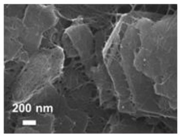

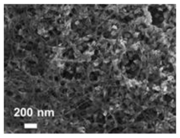

Property	CNTs	Graphene	Defective carbon	Conductive Hybrid	Reactive Hybrid
Mechanical Strength	High	Medium	Low	High	High
Electrical/thermal conductivity	High	Medium	Low	High	High
Specific surface area	Low-medium	High	Medium	High	High
Chemical Reactivity	Medium	Low-Medium	High	Low	High

2.2 Experimental Methods

For single component materials, a solution of 0.5 mg/ml HiPco SWCNTs (Unidym) or 0.5 mg/ml single-walled carbon nanohorns were dispersed in 1-methyl-2-pyrolidinone (Aldrich, 99.5%) was prepared and left to sit overnight. For hybrid materials, a starting solution of 0.5 mg/ml SWCNT in NMP was mixed with the other carbon nanomaterials, namely, single-walled carbon nanohorns,[13-16] carbon nanosheets (grade 4, cheaptubes.com), and carbonized silicon nanoparticles (US Research Nanomaterials, Inc) at a concentration of 0.5 mg/ml and left to sit overnight. Prior to deposition, all solutions were ultrasonicated for 1 hr before placement into the roll-to-roll system's reservoir.

EPD of carbon-based nanomaterials was performed in a vertical EPD cell with a separation of 4 mm between a 0.5 x 0.5 cm stainless steel counter electrode and a 0.5 cm x 0.5 cm working electrode. Monitoring of current and the application of voltage was performed using a LabView-operated Keithley 2602A Sourcemeter. After film deposition, the battery electrodes were dismounted from the system and left to dry horizontally overnight on glass slides covered by a Kimwipe. After drying, materials were weighed and then assembled into a coin cell utilizing a half-cell configuration with a lithium metal foil counter electrode, a 1 M $LiPF_6$ ethylene carbonate/dimethyl carbonate (Sigma Aldrich) electrolyte solution and a Celgard battery separator. Assembly was performed in an Argon-filled glovebox with O_2 levels <0.5 ppm (MBraun). Electrochemical testing was performed using a Metrohm Autolab multichannel testing system which performed both cyclic voltammetry and galvanostatic charge discharge measurements. Raman analysis was performed using a Renishaw inVia Raman microscope with a 532 nm excitation**.** Zetasizer measurements were carried out using a Malvern Zetasizer Nano ZS instrument**.**

2.3 EPD of Carbon Nanomaterials

The integration of the aforementioned carbon nanomaterials into functional applications depends on the ability to either grow the materials in functional templates, or assemble them from bulk nanomaterials posthumously. This requirement has led to a significant amount of effort focused on the growth of carbon nanotubes (CNTs) and graphene in functional three-dimensional architectures that are viable for a broad range of applications[17-21]. The high temperature processing methods that result in the growth of primarily sp^2 hybridized carbon nanostructures enables a wide range of templating possibilities through a tailoring of the growth substrate geometry. Whereas the majority of such studies have focused on CNT and graphene materials, defective carbon materials with controlled porosity such as carbon nanohorns (CNHs) are also a promising nanostructure that offers complimentary properties to other forms of nanocarbons.[13, 22, 23] CNHs exhibit a high surface-area architecture that, unlike CNTs and graphene, hosts a large number of reactive *sp*^{3} carbon edge sites that makes them ideal for anchoring discharge products to the conductive carbon skeleton during electrochemical operation. However, since it is not currently feasible to directly grow CNHs in self-assembled architectures, liquid-based processing and manufacturing routes must be developed to enable CNHs as a viable nanomaterial for applications. In this light, EPD processing presents a viable approach to make this material compatible with processing of other forms of carbon nanomaterials.

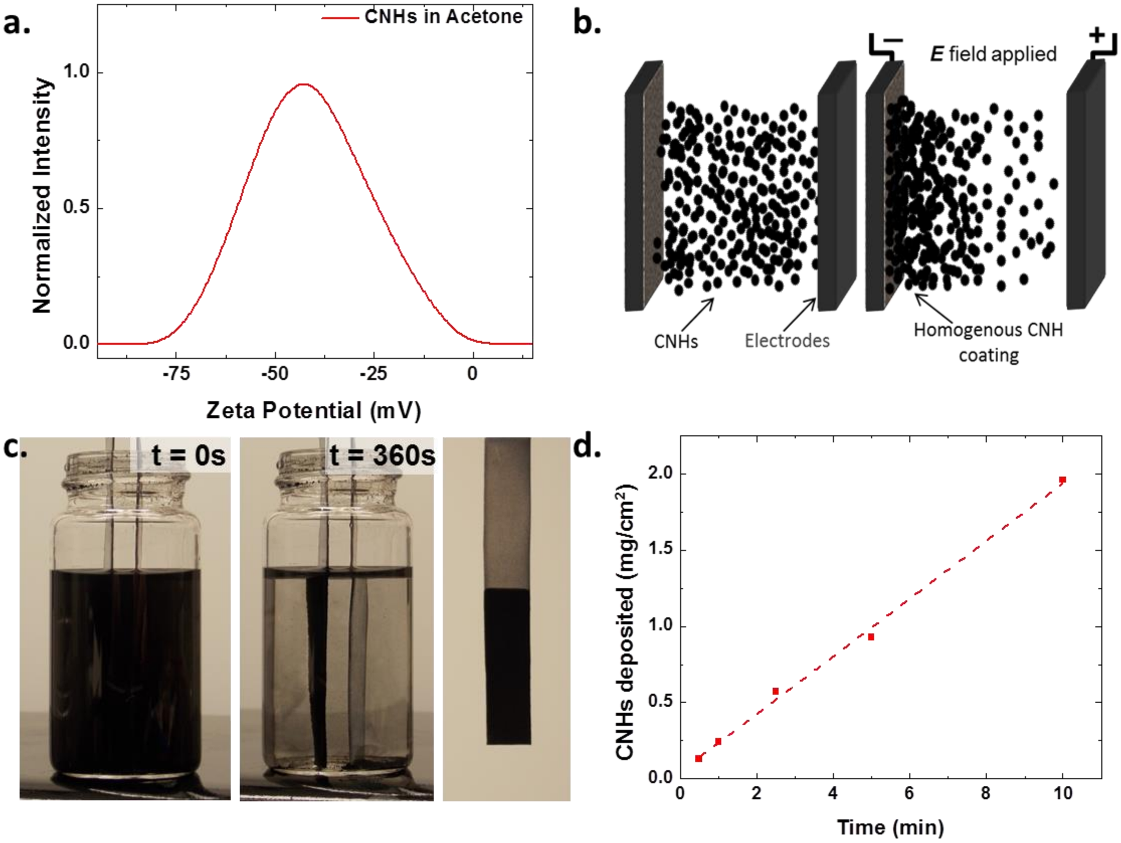

Figure 2.1. (a) Zeta potential measurements of CNHs suspended in acetone. (b) Schematic illustration of the EPD process used to assemble CNHs from solution. (c) Time study of the EPD process for CNHs from acetone and (d) accumulated CNH mass as a function of time for an application of 40 V.

One of the most critical parameters for EPD processing of a chosen material is the zeta potential, which provides a general representation of the net charge on a particle dispersed in a solution. Due to the high reactivity of these CNH nanostructures, the solubility of these materials in common organic solvents is easily achieved and Figure 2.1a characterizes the zeta potential of these materials in the common organic solvent acetone. The surface charge of these materials is attributed to the dissociation of carboxylic functional groups that leave behind a negatively-charged, oxygen terminated structure when H^+ is dissociated from the hydroxide terminal group. As a gauge of dispersion quality, materials exhibiting a zeta potential with a magnitude exceeding +/- 30 mV are typically considered stable. In acetone, suspensions of CNHs yield an average zeta potential of -41.1 mV. With the development of a sufficient surface charge, these materials become susceptible to the EPD process depicted schematically in Figure 2.1b. To fabricate the EPD system, stainless steel electrodes were immersed in the solution at a separation of 0.3 cm and a voltage of 100 V was applied across the electrodes using an Agilent DC power supply.

For EPD processing, the rate at which a particle moves to an electrode under an applied electric field is referred to as the electrophoretic mobility and is represented below by the Smoluchowski approximation:

$$\mu = \frac{V\varepsilon\varepsilon_0\zeta}{4\pi\eta D} \qquad \text{(equation 2.1)}$$

For ε the dielectric constant of the liquid, ε_0 the permittivity of free space, ζ the zeta potential of the particles, η the viscosity of the liquid, *V* the applied voltage and *D* the electrode separation. Due to the high mobility and low viscosity of these material-solvent systems, the deposition of these materials can occur very rapidly with complete assembly of dispersed material in less than 6 min (Figure 2.1c). A study of the mass accumulation over time yields an insight to the mechanism of assembly (Figure 2.1d). The total mass deposited during EPD as a function of time, *t*, may be predicted using the widely accepted Hamaker approximation for the deposition rate of inorganic particles under an applied electric field, represented by the expression:

$$w(t) = \int_{t_1}^{t_2} f\mu E A c_s \, dt \qquad \text{(equation 2.2)}$$

which relates the weight of deposited material, *w*, to the product of the electrophoretic mobility μ, electric field strength *E*, electrode surface area *A*, and particle concentration in suspension c_s. The efficiency factor *f* accounts for the fact that not all particles which migrate to the electrode surface will contribute to the formation of the deposit and has a value of 1 for the case in which all migrating particles deposit on the electrode surface. A fit to the mass accumulation data is presented as a dotted line in Figure 2.1d and sufficient agreement between experiment and theory is confirmed. The films assembled using this approach are extremely uniform with minimal aggregates observed due to the effective dispersion of these materials in the solvent as emphasized in Figure 2.2.

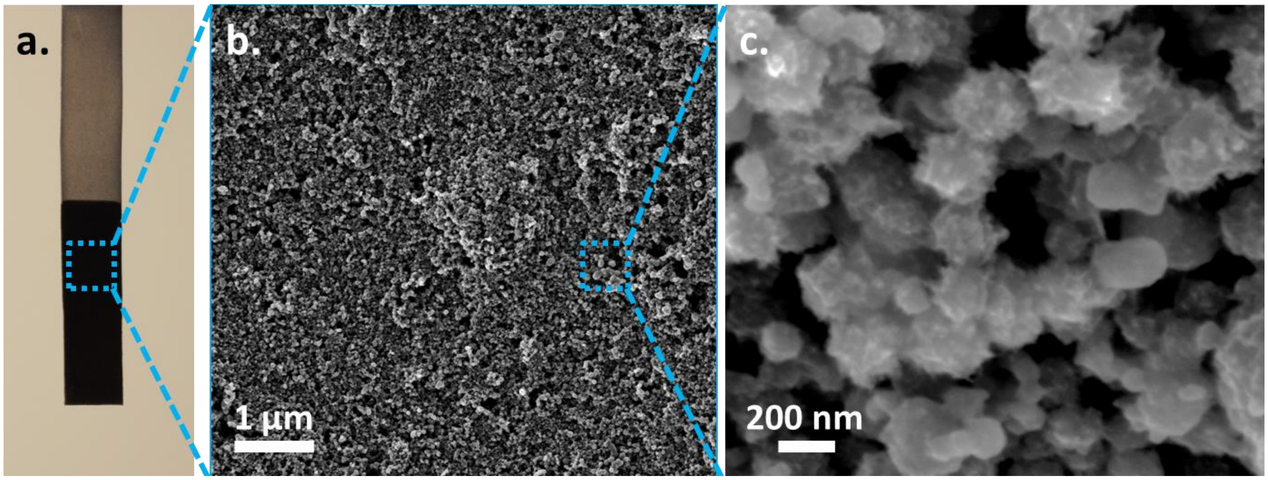

Figure 2.2 (a) Optical photograph of a film of CNHs assembled on an aluminum current collector (b) SEM imaging of the CNH film with a higher magnification image in (c) emphasizing the absence of substantial aggregates.

2.4 Assembly of Hybrid Solutions of Nanocarbon Materials

Although CNHs represent an ideal material with which to introduce the concept of EPD for nanocarbon materials, macroscopic assemblies of these materials present numerous challenges for direct implementation as a stand-alone current collector for electrode applications. The low conductivity that arises from their highly defective structure and the mechanical instability resulting from the low contact surface area requires a hybridization of this material with additional carbon materials to impart the necessary structural and electrical stability to the carbon film. Figure 2.3 below emphasizes the poor conductivity and interconnectivity of these films through I-V measurements and scanning electron microscopy (SEM) images of macroscale films.

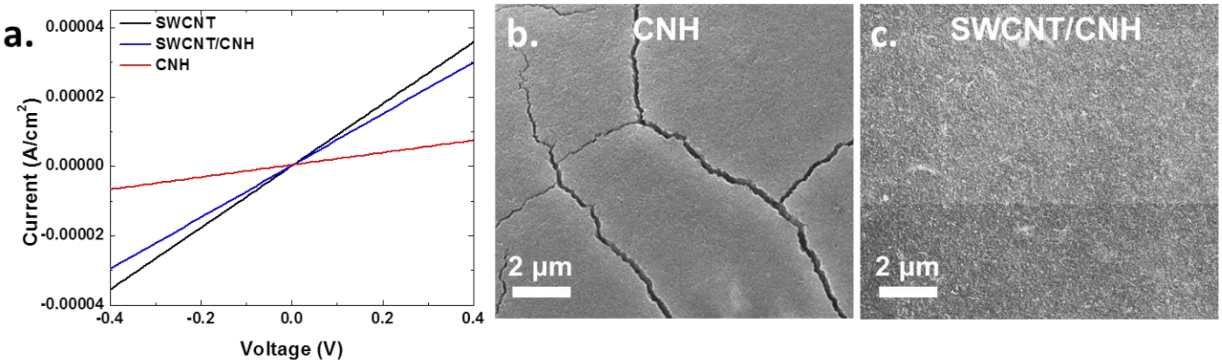

Figure 2.3. (a) I-V measurements of carbon films comprised of SWCNTs, a mixture of SWCNTs and CNHs and solely CNHs. SEM characterization presented in (b) and (c) emphasize the poor mechanical stability characteristic of thick films of CNHs.

Due to the highly polar nature of defective carbon materials, many different types of solvents are able to effectively solubilize CNH materials. However, in the case of graphitic, sp^2 carbons such as SWCNTs or carbon nanosheets (CNSs), the high aspect ratio, strong van der waals attraction, and graphitic nature of these structures prohibits solubility in most solvents. The low content of defective, sp^3 hybridized carbon atoms in SWCNTs and CNSs may be evidenced through Raman spectroscopy measurements presented in Figure 2.4a. In the Raman spectra, the peak at ~1350 cm^{-1} (referred to as the ‘d-peak’) corresponds to a signature produced through sp^3 hybridization while the peak at ~1600 cm^{-1} (referred to as the ‘g-peak’) corresponds to graphitic *sp*^{2} carbon atoms. The relative intensity of the d-peak to the carbon g-peak yields a qualitative estimation of the defect concentration for a given material. From the plot in Figure 2.4a, it is evident that both SWCNTs and CNSs possess primarily graphitic carbon while CNHs comprise mostly of defective carbons.

Whereas numerous combinations of these different nanostructures could be studied, SWCNTs make up an essential component for all hybrid composites due to the web-like nature of ensembles of these materials that can empower a hybrid material with improved electrical and mechanical connectivity between the individual components. To this end, substantial progress has been made in solubilizing SWCNTs in surfactant-free solutions through the use of highly polar solvents or superacids[24, 25]. In this regard, 1-methyl-2-pyrrolidone (NMP) has demonstrated growing popularity for solution processing of individual carbon nanostructures due to its exceptionally high surface tension ($\gamma > 40$ mJ/m2) and highly polar nature[26]. Dispersions of SWCNTs in NMP were found to possess suitably charged surfaces for EPD as observed through zeta potentials with magnitudes > 30 mV. Figure 2.4 below highlights the dispersion quality of the three primary forms of carbon nanostructures in NMP through DLS measurements of their hydrodynamic diameter and zeta potential.

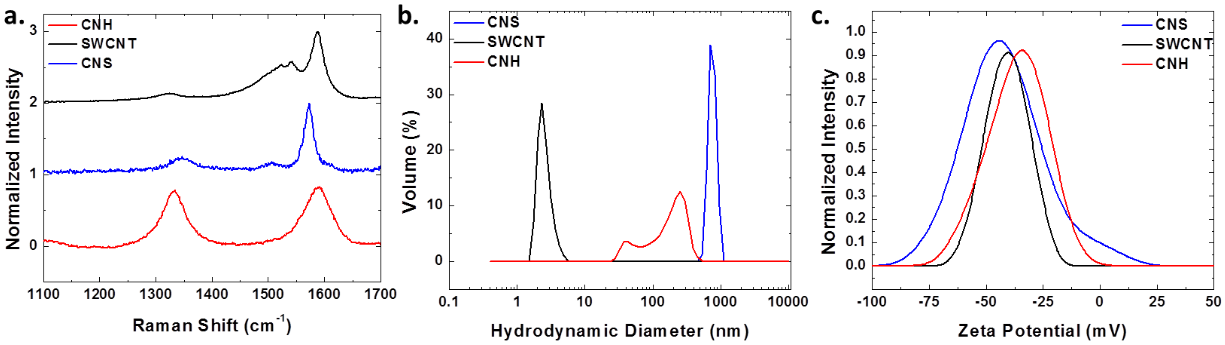

Figure 2.4. (a) Raman spectroscopy characterization of the various types of carbon structures used in this study. (b) Hydrodynamic measurements of the nanomaterial diameter and (c) zeta potential when suspended in NMP.

As evidenced by the above plots, efficient dispersion of SWCNTs in NMP solvent is achieved with a size distribution of less than 5 nm and a zeta potential in the range of -40 mV implying the formulation of a stable suspension. Similarly, efficient dispersions of the co-suspended nanomaterials, namely CNSs and CNHs were also achieved with small particle size distributions and large zeta potentials. For solutions with NMP, dispersed nanomaterials acquire a net negative charge through electron transfer reactions with the solvent molecules[27] and are subsequently attracted to the anode in an EPD process resulting in film formation. In this light, it is clear that NMP represents a suitable solvent to efficiently solubilize the various types of carbon nanostructures important for film formation.

A study of SWCNT EPD from NMP onto conductive substrates leads to unique mass deposition characteristics. An analysis of the mass deposited over time for SWCNTs is presented in Figure 2.5a. Notably, in this system, an exponentially decaying mass deposition rate is observed contrary to the mass accumulation results predicted by the Hamaker approximation. An attempted fit to this data using the conventional Hamaker model is provided as a red dotted line inset. Insights into the cause of this effect are obtained through a consideration of the solution properties of nanomaterial suspensions. When high aspect ratio nanoparticles are present in high concentrations in solution, a number of different considerations must be made that deviate from traditional suspensions of macroscale objects. When particles with high anisotropy are present in solution, the orientable nature of their contribution to solution viscosity and the high degree of interparticle interaction that arises from particles with large contact area presents substantial contributions to the solution viscosity at relatively low concentrations.[28] This implies that, due to the high aspect ratio of SWCNTs, the growing concentration of SWCNTs at the electrode surface locally increases the viscosity of the solution in the vicinity of the electrode thereby inhibiting migration as the electrophoretic mobility has an inverse relationship with solution viscosity.[29, 30] To confirm this effect, simulations were performed using a model similar to that developed by Sarkar *et al.* to simulate constant voltage depositions.[31] In constant-voltage EPD a variable mobility parameter, $\mu(t)$, is implemented to account for changes in particle mobility that arise from screening of the applied electric field by the growing, insulating deposit:

$$\int dW = f \iint dS\, \mu(t)\, C(t)\, dt \qquad \text{(equation 2.3)}$$

Where a weight dW is deposited on an area dS of the electrode. In this case, f represents the 'sticking factor' which varies as a function of the nanostructure used, $\mu(t)$ the particle velocity, and $C(t)$ the solution concentration. In the case of EPD of SWCNTs, however, it was found that the changes in particle mobility may be attributed to the drastic increase in solution viscosity near the vicinity of the electrode as SWCNTs represent a material which exhibits a significant concentration-dependent relationship with solution viscosity.[32-34] Due to the proposed "entanglement effect", viscosity changes within solution scale non-linearly with SWCNT concentration yielding dramatic changes over multiple orders of magnitude when SWCNTs comprise a significant fraction of the solution volume. During EPD, the imposed migration of SWCNTs creates a significant concentration in the vicinity of the electrode thereby substantially influencing the viscosity. To account for the changing viscosity, a deposition region extending 0.15 mm from the electrode surface was considered and the viscosity model developed by Halefadl et al.[35] was used to calculate the viscosity in this region under the assumption that all measured deposited SWCNTs were deposited in this region. This model utilizes a modified Maron-Pierce equation for suspensions of rigid rod-like particles in order to calculate the viscosity of SWCNT suspensions:

$$\mu_r(t) = \left(1 - \frac{\phi_a(t)}{\phi_m}\right)^{-2} \qquad \text{(equation 2.4)}$$

Where μ_r represents the relative viscosity of the solution, ϕ_m the maximum volume fraction of suspended nanotubes, and $\phi_a(t)$ the volume fraction of SWCNTs in the vicinity of the electrode. The value of ϕ_m was determined by the aspect ratio of the SWCNTs used and calculated to be 0.015[33]. A plot of the calculated viscosity during the deposition is provided in Figure 2.5b. Changes in particle mobility were accounted for by substituting the above time-dependent viscosity parameter into equation (1). Notably, the effects of film formation on changes in the applied field were neglected as the SWCNTs themselves form a conducting layer with similar conductivity as the electrode itself.[36]

When combining multiple structures of carbon nanomaterials in solution, the measured zeta potential represents a weighted average of the individual species. Likewise, for EPD assembly, the total mass deposited is the sum of the deposition of SWCNTs and the co-suspended material:

$$\int dW = f\,E \iint dS \frac{\varepsilon_0 \varepsilon \zeta_{CNT}}{\eta(t)}\, C_{CNT}(t)\, dt \;+\; f\,E \iint dS \frac{\varepsilon_0 \varepsilon \zeta_{particle}}{\eta(t)}\, C_{particle}(t)\, dt \qquad \text{(equation 2.5)}$$

Where ζ_{CNT} and $C_{CNT}(t)$ represent the zeta potential and concentration of SWCNTs, respectively, and $\zeta_{particle}$ and $C_{particle}(t)$ represent the zeta potential and concentrations for the co-suspended nanomaterials.

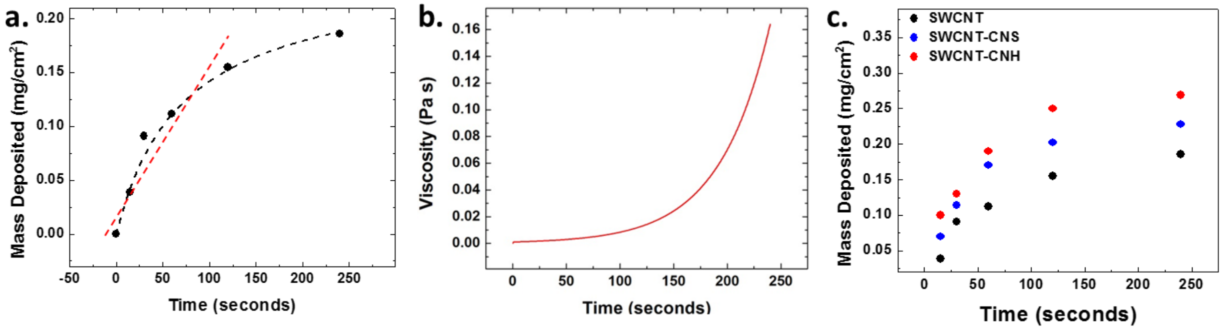

Figure 2.5. (a) mass deposition as a function of time for SWCNTs in NMP. The red dotted line represents a fit to the data using the traditional Hamaker approximation while the black dotted line represents fits to the data using the modified mobility approach. (b) calculated changes to

viscosity as a function of time as the SWCNTs migrate toward the electrode surface. (c) mass deposition profiles for all nanocarbon hybrid solutions used in this study.

In all cases, hybridized solutions of different nanostructures yield coatings containing hybrid nanomaterials (Figure 2.5c). This builds upon the notion that a polar solvent will screen excessive particle-particle interaction between dissimilar species, and hence EPD processing will lead to homogenous coatings of hybrid materials. This was observed to be the case and representative images of the hybrid materials formed in this process are shown in Figure 2.6a-c. Whereas numerous combinations of these different nanostructures could be studied, we chose SWCNTs to be a common component between all hybrid materials due to the web-like nature of the SWCNTs that can empower a hybrid material with improved electrical and mechanical connectivity between the nanostructures. The models developed in this section enable control over the deposition rate using changes to the EPD parameters.

2.5 Electrochemical Characterizations

After fabrications, the films were assessed for their electrochemical performance. The first step in this process is to assess the energetics of Faradaic chemical reactions occurring between the hybrid materials produced using this EPD technique in a half-cell configuration, with lithium metal as the anode. To accomplish this, cyclic voltammetry (CV) scans at a rate of 0.1 mV/s were performed in half cell configurations (vs. Li electrodes) and the results are summarized in Fig. 4. CV analysis of the SWCNT film emphasizes that a majority of the Faradaic charge-transfer reactions arising from storage on the SWCNT surface lies in a broad Faradaic storage peak between ~1-3 V vs Li/Li$^+$. For our system, this storage regime gives rise to a capacity of 658 mAh/g. Density functional theory calculations have emphasized that these reactions may be mediated through surface defective carbon sites,[37] as these do not occur in the same potential window as intercalation in graphite. Hybrid SWCNT-SWCNH materials, which exhibit an exceptionally high defect density, yields substantial enhancement to charge stored in this regime evidenced through higher peak current values during CV scans as well as greater capacities during device cycling yielding a maximum capacity of 884 mAh/g. For CNSs, a material with low defect density, little-to-no enhancement in this regime is observed, however, additional capacity is provided at lower potentials through the intercalation of lithium between graphitic sheets yielding an improved capacity of 978 mAh/g.

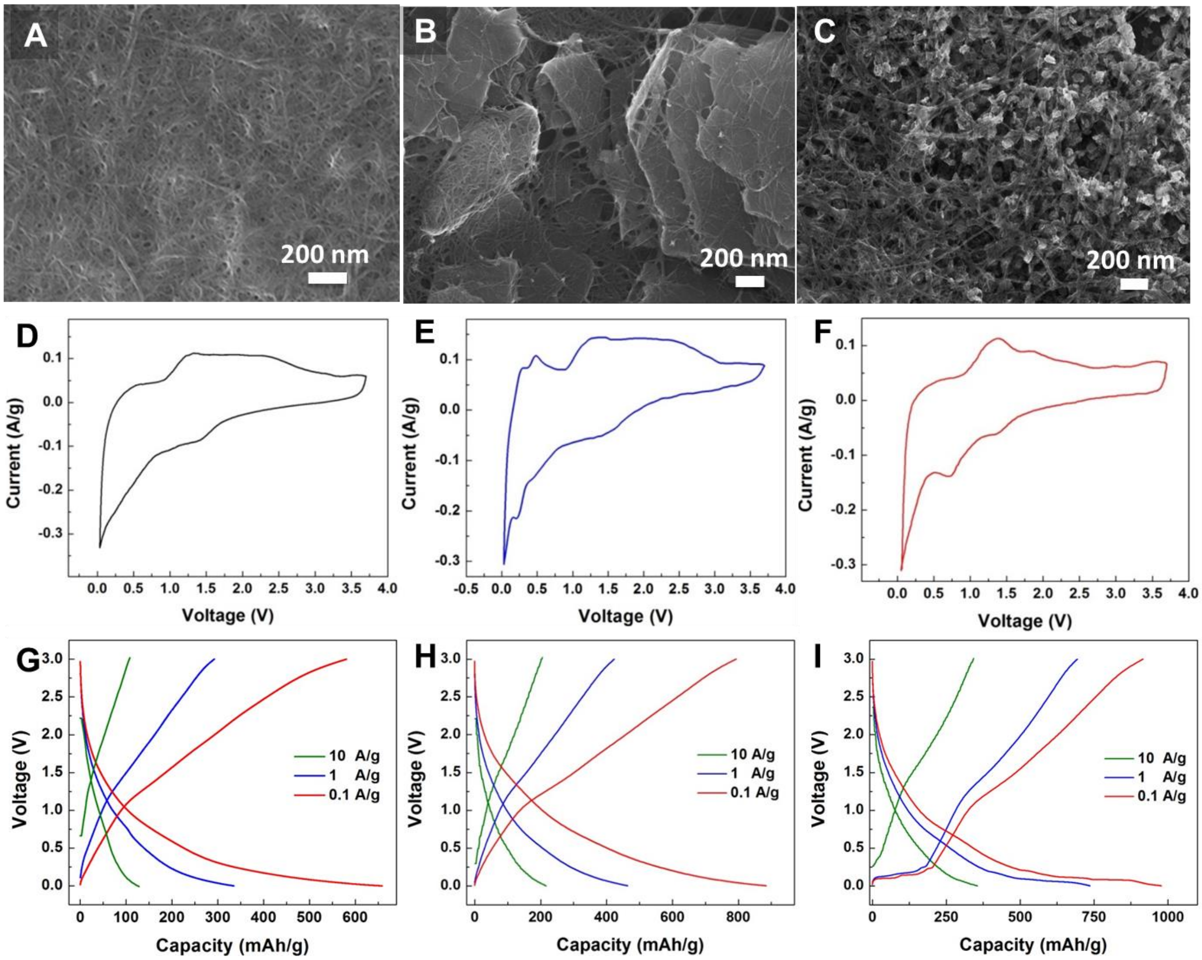

Figure 2.6. SEM characterization of (a) SWCNT (b) SWCNT-CNS (c) SWCNT-CNH along with the respective CV curves in (d)-(e) and galvanostatic charge-discharge curves in (g)-(i).

From the above plots, it is evident that the use of hybrid forms of different types of carbon nanomaterials enables a control over the reactivity of the electrode for Li-ion batteries. Unfortunately, however, a full-cell fabricated from these materials is not practical due to the poor operating voltage obtained between the lowest intercalation voltage (CNS, ~0.3 V vs. Li/Li+) and the highest intercalation voltage (CNHs, ~1.5 V vs. Li/Li+). Using these materials as an anode and cathode material yields a poor operating voltage of less than 1.2 V and a maximum energy density that lags behind that of more traditional Li-ion battery electrode materials. In order to overcome these challenges, these carbon nanomaterials must be combined with better suited Li-ion materials that can obtain superior capacities and operating voltages and is the subject of the next chapter.

CHAPTER 3

Roll-to-Roll Production of Hybrid Nanomaterials for Full-Cell Battery Production

3.1 Introduction

Whereas the last chapter demonstrated the feasibility of EPD for carbon nanomaterial assembly, the ability to merge these assembly processes with that of nanostructures composed of varying compositions is essential in ensuring the applicability of this manufacturing technique to practical electrode materials. Whereas nanostructures are consistently lauded for improved performance in applications at the laboratory scale, fabrication processes and costs for industrial processing often limit near-term commercial impact of many nanomaterials for Li-ion battery electrodes. Unlike bulk materials, the physical and chemical properties of materials composed of nanostructures are strongly correlated to impurities that interact with the nanostructures and the transport paths between adjacent nanoscale building blocks in the material. This provides two extremes for nanomaterial fabrication: (i) highly precise, expensive fabrication routes carried out in clean environments (*e.g.* ultraviolet or electron-based lithographic techniques), or (ii) large-scale, low-cost "coarse" material processing that relies on the use of liquid processing with surfactants (*e.g.* colloidal processing such as blade coating and/or electrophoretic deposition, or EPD). The results presented in this chapter aim to explore the medium existing between these two processing routes where scalability and control or precision can be simultaneously achieved for the fabrication of battery anode and cathode materials.

Significant research has been carried out to study the performance of various materials as anodes for lithium ion batteries, with silicon being distinguished for its ability to maintain high capacities (10X greater than conventional carbon anodes[38-40]). Alternatively, transition metals are conventionally used as cathodes, due to the ability to achieve high voltage when paired with graphite anodes and inhibit degradation under Li^+ oxidation and reduction reactions. However, a challenge for innovation in battery research is to not isolate the performance of a single component (anode, cathode, or electrolyte) of a battery, but instead to harness the versatility to engineer all working components simultaneously and thus engineer the performance of full-cell material systems.[41] Accomplishing this requires versatility in the materials processing approach that goes beyond applications based assessment of individual materials using a discovery-driven approach.

In this chapter, methods to overcome these challenges is presented by demonstrating the operation of a benchtop roll-to-roll platform to produce high-throughput, clean coatings of hybrid materials that can facilitate battery design applications. To demonstrate this approach, focus is maintained specifically on hybrid materials composed of single-walled carbon nanotubes (SWCNTs), MoS_2 nanosheets, and silicon nanoparticles. EPD from polar solvent solutions containing mixtures of these nanostructures is demonstrated in order to form homogenous coatings that are comprised of hybrid nanostructured materials. These coatings are then assessed for their composition-dependent lithium reduction/oxidation energetics, which leads to a full-cell battery design with electrodes produced in less than 30 seconds with an optimized design that incorporates pre-lithiated silicon nanoparticles as an anode, and MoS_2 nanosheets as a cathode.

3.2 Experimental Methods

The roll-to-roll (R2R) system was assembled by mounting gear motors (4 RPM, Servo City), powered by a 12V, 2.5A power supply (Servo City), onto a custom designed Teflon reservoir. The Teflon reservoir contained a 90cm x 20cm square well across which two Teflon rollers were mounted and at the bottom of which a 65cm x 20cm steel plate was mounted. The roll was composed of a 1cm x 1m aluminum strip (Grainger) mounted on both ends to either gear motor. A bias was applied between the aluminum roll and the steel plate using a Keithley 2400 Sourcemeter.

R2R electrophoretic deposition of carbon-based nanomaterials was performed in a vertical EPD cell with a separation of 4mm between a stainless steel counter electrode and the working electrode. For the fabrication of battery films a 316 stainless steel disc (Pred Materials) was mounted to a biased brass roller and rolled through the reservoir containing the depositing solution and stainless steel counter electrode using a 4RPM gear motor (Servo City). For mass deposition studies, a 3cm x 1.5cm aluminum strip of known mass was mounted to the brass roller using Teflon clips, mechanically moved into position above the counter electrode, and left to rest in this position for the specified time and applied electric field. To demonstrate continuous operation of the coating process, an aluminum roll of dimensions 1m x 1.5cm was mounted to either end of the system and continuously moved through solution at a rate of ~1.5cm/s under an applied electric field of 500 V/cm. Monitoring of current and the application of voltage was performed using a LabView-operated Keithley 2602A Sourcemeter.

After film deposition the battery electrodes were dismounted from the system and left to dry horizontally overnight on glass slides covered by a Kimwipe. After drying, materials were weighed and then assembled into a coin cell utilizing a half-cell configuration with a lithium metal foil counter electrode, a 1 M $LiPF_6$ ethylene carbonate/dimethyl carbonate (Sigma Aldrich) electrolyte solution and a Celgard battery separator. Assembly was performed in an Argon-filled glovebox with O_2 levels <0.5 ppm (MBraun). Electrochemical testing was performed using a

Metrohm Autolab multichannel testing system which performed both cyclic voltammetry and galvanostatic charge discharge measurements.

3.3 Roll-to-Roll Electrophoretic deposition

Underlying the ability to produce scalable coatings of pristine, hybrid nanostructures is the necessity to develop a platform that overcomes the "beaker-scale" processing limitations of most materials processing approaches. In order to achieve this, a fully automated, benchtop roll-to-roll (R2R) system is developed that builds upon the widely known process of EPD in the framework of industrial-scale roll-to-roll process design. The operating principle of this system (Figure 3.1a) utilizes a roll of material (with a composition that can vary across a wide range of conductive foils and substrates[15, 31]), that is rolled through a pool of solution, coated in a controllable manner, and then collected in a roll on the opposing side. In traditional beaker-scale EPD systems, both an anode and cathode are biased in a solution to drive the migration and deposition of nanostructures dispersed in the liquid onto an electrode with a polarity that opposes the overall charge of the particles in solution. In this case, the same process is achieved, except the conductive foil (aluminum foil) is biased through a wire brush contact with a bottom electrode that is maintained at a fixed distance beneath the roller. Therefore, when the foil is submerged in the liquid, an electric field is applied between the top and bottom electrode that generates a constant electric field, despite the continuous movement of the top foil electrode. A photograph of the benchtop R2R system developed for this study is presented in Figure 3.1b, with an empty liquid reservoir for the purposes of visualization. Notably, this system was constructed and operated with cost of parts and equipment totaling under $300.

Coatings of various dispersed nanomaterials were fabricated with this system by applying an electric field of 100 V/cm between a stainless steel counter electrode (immersed in solution) and an aluminum foil roll that is extended between the two rollers. A coated foil showing the clear demarcation point when the voltage is turned "on" and a scheme of the deposition process are shown in Figures3.1c and 3.1d. In this system design, faster deposition rates per unit electrode area can be achieved both by increasing the electric field intensity or decreasing the rolling rate of the electrode. This provides an advantage of the roll-to-roll design over the conventional beaker-scale system, in that control over deposition can be tuned more precisely, and automated process parameters can be modulated in real-time based on increasing or decreasing the rolling rate and/or potential. This is generally illustrated in Figures 3.1e and 3.1f, where deposited mass of coatings containing SWCNTs or hybrid coatings of SWCNTs combined with silicon nanoparticles (Si NP) and exfoliated MoS_2 nanosheets is demonstrated as a function of absolute voltage and total deposition time. From Figure 3.1e, the mass deposited is observed to exhibit a nearly linear relationship with the applied voltage in all cases. Figure 3.1f indicates further that the total mass deposited is a nonlinear function of the total deposition time. Notably, the capability to engineer deposition process parameters by decoupling these two parameters of deposition time and voltage is unique to the roll-to-roll system, and can't be achieved in conventional "beaker-scale" processes straightforwardly. In both cases of Figure 3.1e and 3.1f, as well as throughout the study presented here, the nanostructures are dispersed in 1-methyl-2-pyrolidinone (NMP) at concentrations of 0.5 mg/mL and hybrid solutions involve equal mass ratios of each nanostructured species. Due to its polar nature, NMP has been demonstrated as an excellent solvent for native dispersion of nanostructured materials, many of which can only otherwise be suspended using surfactant solutions. Recent efforts have demonstrated that EPD of SWCNTs from NMP polar solvents yields materials where electrochemical and thermogravimetric analysis confirms the pristine quality of the coatings, in comparison to processes carried out with surfactants that yield a significant (up to 50% by weight) mass due to impurities.[42] As the basis of EPD processing of nanomaterials has built on surfactant- or ion additive-enabled processes, our approach not only enables R2R capability, but simultaneously leads to an impurity-free coating process, which is critical toward the performance of nanostructured materials.

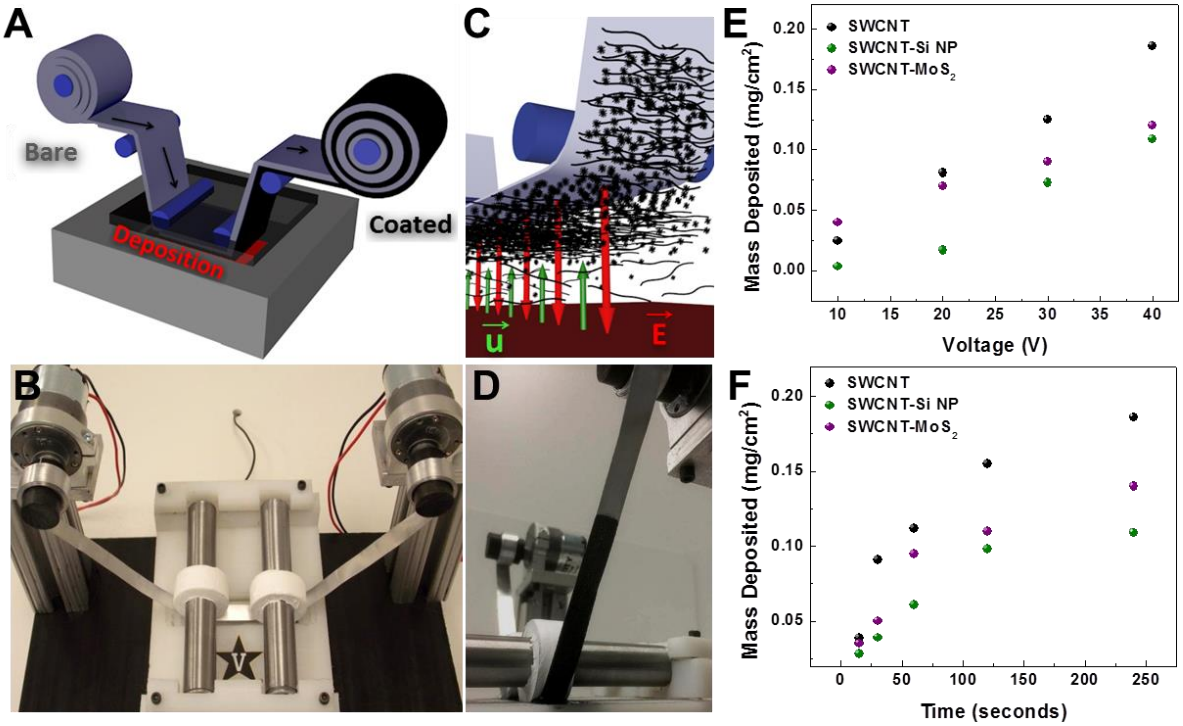

Figure 3.1. (a) Schematic of the roll-to-roll system used in this study (top) and the functional system used in this study (bottom). Uncoated material (blue) is rolled through a reservoir containing the active solution and a counter electrode under an applied bias of 40V (b) Mass deposited as a function of time for all hybrid material combinations (c) Mass deposited after a 240s exposure in the bath as a function of applied voltage. (d) Illustration of the EPD process (top), and a coated roll of aluminum leaving the deposition bath (bottom). Mass deposition profiles versus applied voltage are presented in (e) and versus applied time in (f).

For solutions with NMP, dispersed nanomaterials acquire a net negative charge through electron transfer reactions with the solvent molecules[27] (Figure 3.2a) and are subsequently attracted to the anode in an EPD process resulting in film formation. Notably, for hybridized solutions of nanostructures, the zeta potential values represent a weighted average of the individual species. In all cases, the rate of deposition is strongly dependent on the degree of electrostatic stabilization within solution and a strong correlation is observed between the limiting mass deposition rate and the zeta potential of the co-suspended particles (Figure 3.2b). While deposition rates vary with solution composition, uniform film formation and an exponentially decaying mass deposition rate is observed across all systems due to the presence of a significant fraction of SWCNTs.

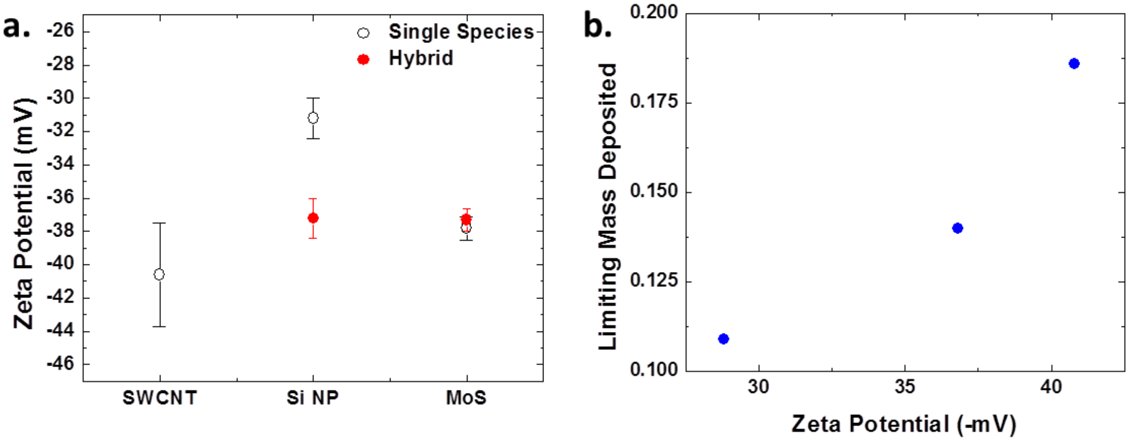

Figure 3.2. (a) Zeta potential measurements for the single component and hybrid species used in this study. (b) graphical illustration of the relationship between co-suspended material zeta potential and the limiting mass deposited.

Shown in Figure 3.3a-c are SEM images showing representative homogenous coatings of SWCNTs, SWCNT-Si NP, and SWCNT-MoS_2 hybrid materials, respectively. Furthermore, the chemical identity of the SWCNT-Si NP and SWCNT-MoS_2 species are identified through energy dispersive X-ray maps taken in the transmission electron microscope (TEM) in Fig. 3d and 3e. Notably, prior to dispersion of the Si NPs, a chemical vapor deposition process is utilized to catalytically stabilize the surface of the Si with a thin carbon layer, evident in Fig. 3e as a thin red shell around the Si core.

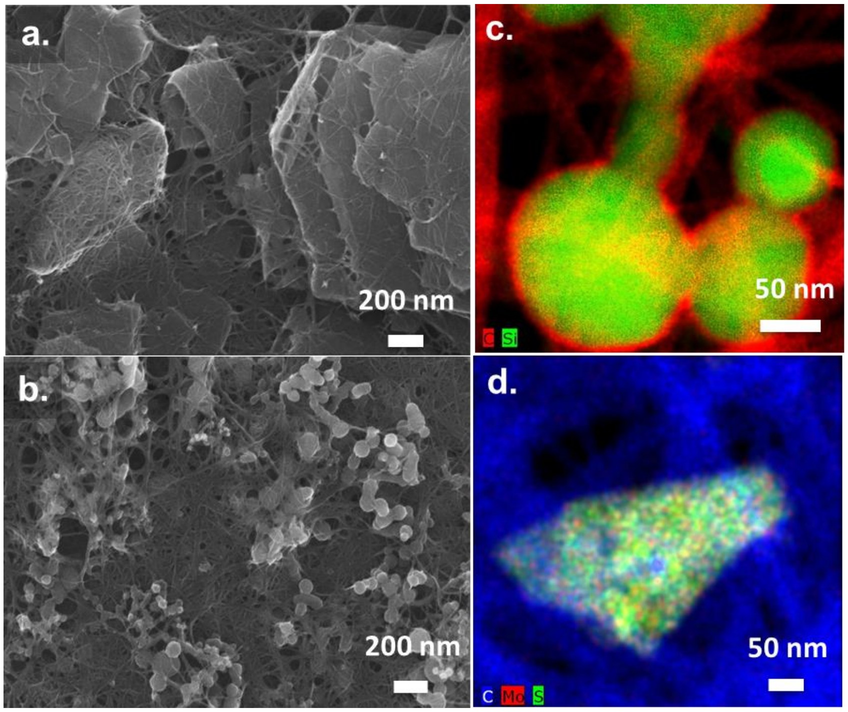

Figure 3.3. SEM images of hybrid films comprised of (a) SWCNT-MoS_2 and (b) SWCNT-Si NPs with elemental analysis acquired through TEM imaging in (c) for Si and (d) for MoS_2.

The presence of this carbon coating is important not only for silicon chemical stability in EPD processing, but also for stability in electrochemical devices and will be discussed at length in a later chapter[43]. Overall, the nature of the intense electric field confined within the diffuse electrostatic boundary layer near the electrode surface provides a natural leveling mechanism capable of giving rise to exceptionally uniform film density and coverage on regions of the electrode not disturbed by other steps in the processing (Figure 3.4). Drying effects, electrode surface roughness, and movement in and out of solution may often induce clumping effects, however, initial film formation is shown to be a highly uniform process.[44]

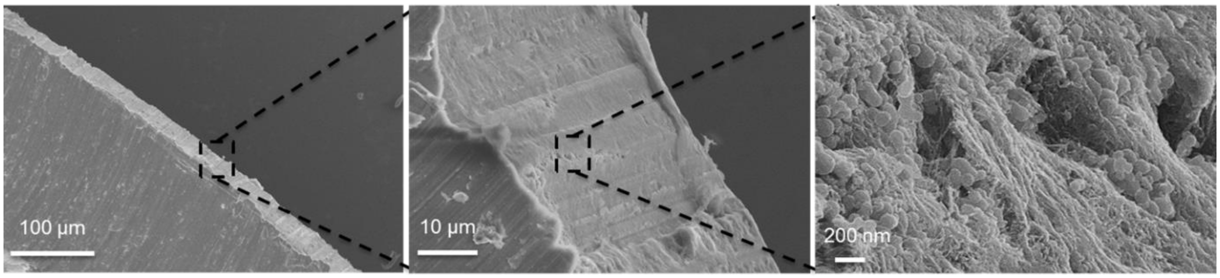

Figure 3.4. SEM image of a cross section of a typical coating produced using the R2R EPD system with insets describing higher magnifications.

3.4 Manufactured Li-ion Battery Performance

One of the key application areas where such nanomanufacturing routes could prove valuable is in the fabrication and optimization of battery materials. Conventional approaches to analyzing the oxidation and reduction energetics of Faradaic energy storage reactions often distinguish materials only by the chemical composition (e.g. carbon, silicon, etc.) and not by the nanostructured characteristics of the material. Furthermore, the challenge in any battery-focused effort, especially in lithium-ion or other metal-ion batteries, is the development of a full-cell architecture that involves optimized anode, cathode, and electrolyte combinations. This is challenging due to the codependence of both electrode chemical stability and metal ion storage potential of each individual component on the combination that is chosen. The focus of the remainder of this chapter is to demonstrate an effort whereby the high throughput R2R system discussed above enables a rational approach to battery design by overcoming both of these challenges and producing an operational full-cell battery from nanomanufactured hybrid nanomaterials produced in this study.

After fabrication, the films were assessed for their electrochemical performance. The first step in this process is to assess the energetics of Faradaic chemical reactions occurring between the hybrid materials produced using this EPD technique in a half-cell configuration with lithium metal as the anode. To accomplish this, cyclic voltammetry (CV) scans at a rate of 0.1 mV/s were performed in half cell configurations (vs. Li electrodes) and the results are summarized in Figure 3.5. For SWCNT-Si NP hybrids, whereas there is some indication of carbon storage that is chiefly attributed to the SWCNT hybrid material, exceptional capacity is observed in the low-voltage lithiation reactions in silicon. This is evident from the large peak currents observed in Figure 3.5a at low voltages vs. Li/Li^+ and a maximum capacity of 1,294 mAh/g for this electrode material (Figure 3.5c). By producing SWCNT-MoS_2 NS hybrid materials (Figure 3.5b), energy storage at high potentials was achieved due to the Li_2S storage mechanism previously defined for MoS_2 NSs yielding capacities as high as 867 mAh/g (Figure 3.5d).

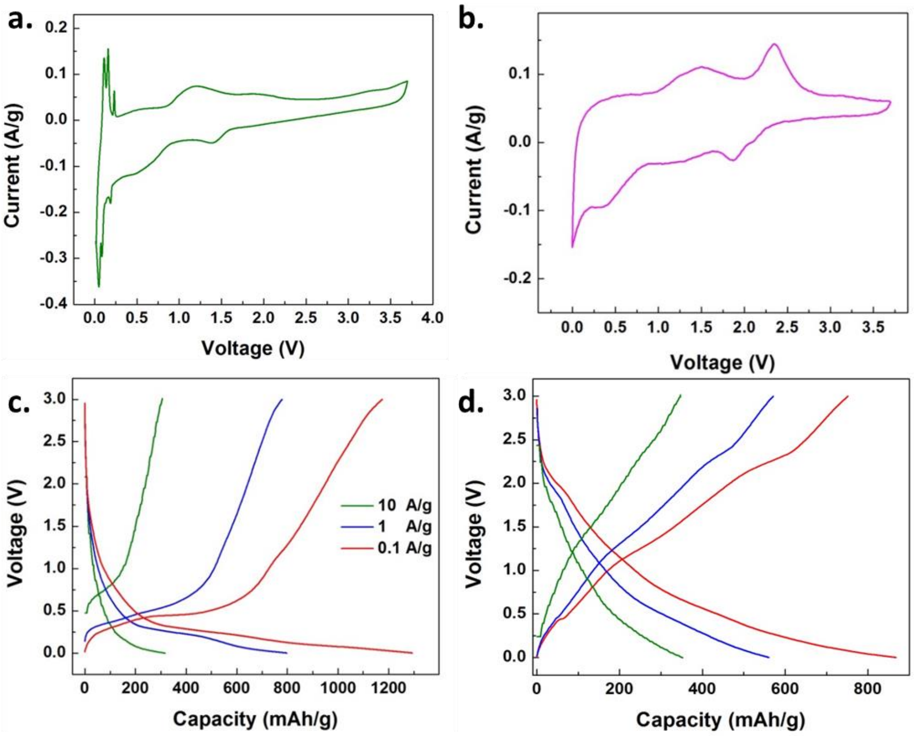

Figure 3.5. Cyclic voltammetry performed at a rate of 0.1 mV-s for (a) silicon and (b) MoS_2 hybrid materials. Galvanostatic charge discharge measurements determined the lithiation capacity of these materials at the specified rates for (c) Si and (d) MoS_2 materials.

As is evident in Fig. 5, the energetics for lithium insertion and removal can be tuned across the spectrum of the stability window of the electrolyte by using these different electrode materials. In all cases, these reduction and oxidation potentials, which are evident in CV scans, are measured against a lithium electrode. Since the use of pure lithium electrodes in full cell architectures leads to dendrite formation,[45, 46] a key challenge for constructing a full-cell battery is to maintain a > 1.5 V potential difference between redox potentials of either electrode (fixed by technological requirements, which are based on conventional alkaline batteries), while utilizing the same electrolyte. To accomplish this, information obtained from CV analysis was utilized to generate a diagram of observed redox potentials (Figure 3.6a), which is inferred from CV scans. In this case, the redox potential for the MoS_2 hybrid material is the highest due to Faradaic storage processes between Li and S species. The higher potential of this system makes MoS_2 a candidate for use as the cathode material in a full-cell architecture. Conversely, aside from lithium metal, the Si NPs exhibit a redox potential that is the lowest of those studied in this work. Therefore Si NPs are a practical choice for an anode material in a full-cell architecture. As Si NPs do not natively contain Li species, lithiation was achieved for anodes in a full cell configuration by placing SWCNT-Si NP electrode materials in direct contact with lithium foil for 3 hours (Figure 3.6b). As previously reported, silicon in direct contact with lithium foil will form a Li-Si alloy providing a facile mechanism to fabricate a source for lithium ions during device cycling.[47] In order to characterize the performance of this device, galvanostatic charge discharge measurements were performed at varying currents, with three representative curves for three currents of 100 mA/g, 1 A/g, and 10 A/g (Fig. 6C). Notably, at rates appropriate for conventional battery applications (100 mA/g), cell capacities of 225 mAh/g were observed, which is comparable to conventional battery systems. However, the nanostructured characteristics of the electrodes, which enable rapid ion insertion from the electrolyte, still enable over 20% of this capacity to be accessed at 100X faster cycling rates, which is not achievable in full-cell battery systems with bulk electrodes. In order to further quantify the cell performance, Ragone analysis was performed to assess the energy-power characteristics of the device based on the total cell mass (Figure 3.6d). The energy density was calculated based on integration of the galvanostatic voltage profiles, and power density was calculated as an average value based on the total energy released over the time duration of the discharge. A maximum energy density of 167 $Whkg_{cell}^{-1}$ was obtained corresponding to a capacity of 225 $mAhg_{cell}^{-1}$ when operated at 100 mAg_{cell}^{-1}. When operated at high charging currents of 10 Ag_{cell}^{-1}, power densities near 10,000 Wkg_{cell}^{-1} were measured, which is on par with the power capability of many modern day supercapacitors (Fig. 6D), while still boasting energy densities near ~ 40 $Whkg_{cell}^{-1}$. Whereas this performance is promising, the nanomanufacturing approach that underlies the ability to produce these electrodes is transferrable to many other applications, such as chemical sensing, optoelectronics, and energy conversion, where clean manufactured hybrid nanostructured materials could lead to improved or ideal performance in these platforms.

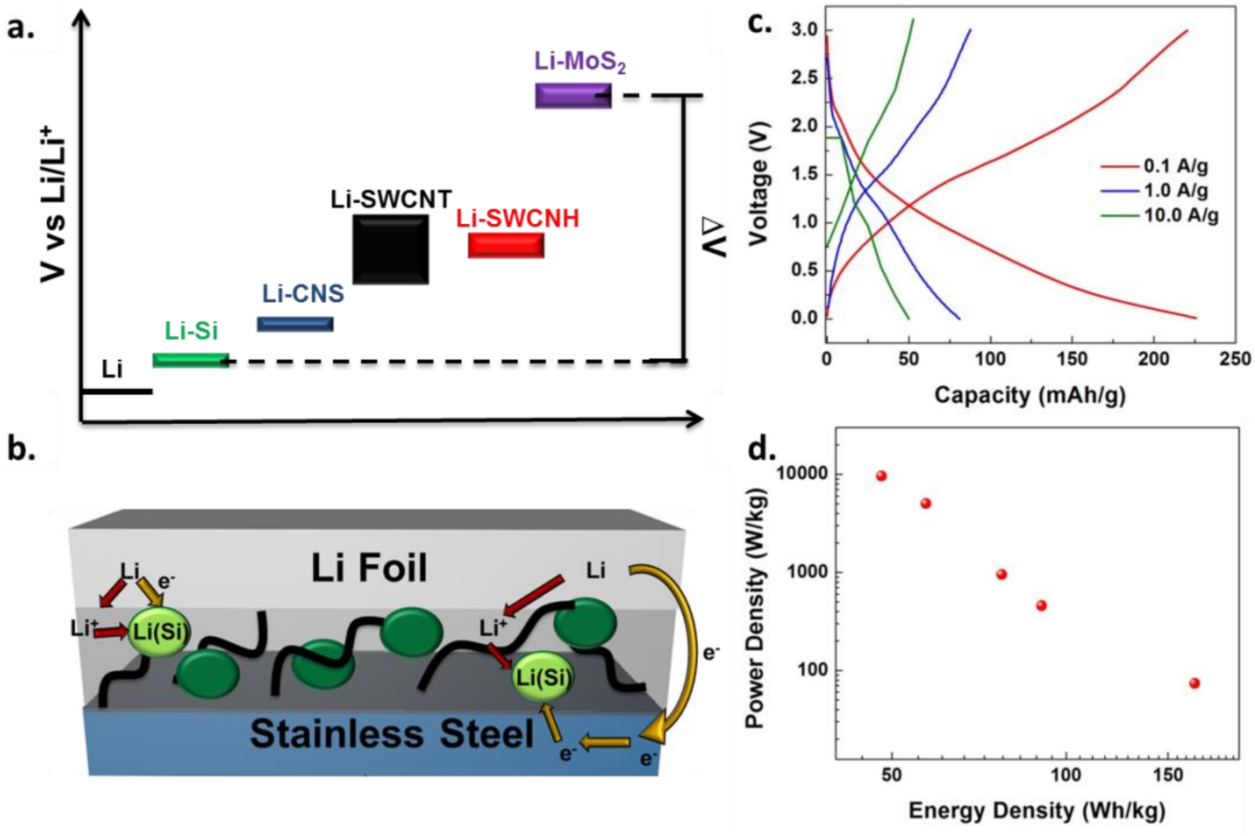

Figure 3.6. (a) Schematic illustration of the wide range of potentials capable of Faradaic lithiation reactions for the different nanostructures investigated. (b) Schematic illustration of the pre-lithiation process in Si NP-SWCNT films and (c) Charge-discharge characteristics of the full cell device fabricated with a pre-lithiated SWCNT-Si NP anode and SWCNT-MoS_2 NS cathode. (d) Ragone analysis of the full cell device.

3.5 Conclusion

This chapter demonstrates the ability to utilize a low-cost (sub-$300), benchtop roll-to-roll system for the rapid development of nanomanufactured hybrid nanostructured materials. This approach depends upon the utilization of surfactant-free NMP polar solvent solutions that both provide stable dispersions of hybrid nanostructure mixtures, and enable controllable EPD processing. Unlike conventional “beaker-scale” EPD routes, the roll-to-roll approach enables greater control over deposition parameters, empowers scalable processing conditions in a laboratory environment that intersects commercial applications, and provides the capability to assemble clean, functional hybrid materials that “bottom-up” fabrication routes are incapable of producing. This chapter specifically demonstrates the fabrication of homogenous hybrid nanostructured materials containing SWCNTs, Si NPs, and MoS_2 nanosheets, and demonstrates the application of these materials into electrodes for a full-cell lithium-ion battery design. Using electrodes that can be fabricated in as little as 30 seconds, a Si NP – MoS_2 all nanostructured material full cell battery was constructed that exhibits full cell capacities on par with conventional Li-ion batteries, but with improved power capability. As the bottleneck for many commercial applications of nanomaterials is a low-cost, reliable, and scalable processing route that builds the foundation for product development and design, this nanomanufacturing approach, which seems unlimited in versatility in the choice of materials, brings potential for many applications extending beyond energy storage into areas of energy conversion, sensing, catalysis, optoelectronics, protective coatings, and others.

CHAPTER 4

Integrated Synthesis and Assembly of Li-ion Cathode Materials

4.1 Introduction

The choice of materials used to comprise the electrodes in a full-cell Li-ion battery is essential in determining both the cost and performance of the final device. In order to achieve energy densities on par with or exceeding traditional technologies, materials exhibiting high capacities and wide operating voltages are required. As emphasized in the previous chapter, molybdenum disulfide (MoS_2) represents a class of two-dimensional nanosheet material that has exhibited exceptional promise as an electrode material for Li-ion batteries. Due to the sulfur-based storage mechanism in this material, efficient use of MoS_2 in a battery architecture can exhibit capacities competitive with state-of-the-art sulfur cathode materials as recent reports have demonstrated reversible capacities exceeding 1,100 mAh/g (or nearly 10x the capacity of conventional cathode materials).[48] Similarly, the emerging class of layered, 2-D transition metal dichalcogenides (TMDs), of which is MoS_2 is a member, has exhibited promising performance for many future battery chemistries such as sodium-ion or potassium-ion batteries. However, in order for this class of nanostructures to be monetarily competitive with traditional materials, the cost for acquiring nanoscale versions of these materials must be competitive with current material manufacturing approaches.[49] In this chapter, a one-batch assembly approach is presented to fabricate functional films of 2-D TMD nanosheets starting from a dispersion of bulk materials. Many of the advantages unique to EPD, such as assembly from dilute solutions, are demonstrated to be key requirements to the success of this process.

Current methods to produce high quality TMD materials for application pivot around high cost, energy intensive, and low-yield efforts such as chemical vapor deposition or mechanical cleavage.[50] These routes are not suited for producing vast quantities of material, and this is a significant challenge for applications that require assembled layers of thick and high quality TMD materials, such as in electrochemical devices, that require large amounts of mass to function appropriately. Therefore, processes that can maintain the chemical integrity of the pristine 2-D TMD NSs and produce functional, thick, and high-throughput coatings is an enabling feature to both extend lab-scale applications for TMD materials and develop routes for cost-effective scale-up of functional TMD coatings to industry scales.

4.2 Experimental Methods

Dispersions of exfoliated TMD nanosheets were obtained using suspensions of MoS_2 (Sigma Aldrich, 99%, ~2µm), $MoSe_2$ (Sigma Aldrich, 99.9%, ~325 mesh) and WS_2 (Sigma Aldrich, 99%, ~2µm) in 1-methyl-2-pyrollidone (Sigma Aldrich, 99.5%) and acetonitrile (Fisher, 99.8%). To form these suspensions, 20 mg of TMD powder was added to 40 ml of NMP or ACN before insertion of a probe sonicator to the solution. Sonication was performed for 30 minutes using a tapered-tip on a probe sonicator (Sonics, VCX750, 30% amplitude) with a 30 second on pulse and 30 second off pulse to avoid excessive heating. All solutions were left overnight before use. For studies using purified TMD material, exfoliated solutions were centrifuged at 2,000 rpms for 10 minutes and the upper 2/3 of the purified solution was harvested for further use.

EPD was performed using a Keithley 2400 Sourcemeter integrated with LabView data acquisition software to apply a constant voltage and record the flow of current. For deposition onto 2-D substrates, two 316 stainless steel electrodes of dimensions 1.0 cm x 3.0 cm were immersed into a beaker containing 20 ml of exfoliated TMD solution at a separation of 0.5 cm. A constant voltage was applied for 2 minutes and the resulting films were placed in a vacuum oven at 60 ^{o}C to dry overnight before measurement of the mass was performed. For deposition on 3-D substrates, a nickel foam (MTI, ~110 ppi) electrode of dimensions 1.0 cm x 3.0 cm was prepared and placed directly into 20 ml of exfoliated TMD solution at a separation of 0.5 cm to 2 identically sized counter electrodes on either side of the deposition electrode. Deposition was performed for 2 minutes at the specified voltage before removing the foam material to hang-dry overnight under ambient lab conditions. After a night of drying, the foam material was placed directly into a vacuum oven at 60^{o}C to ensure removal of any residual solvent.

To accomplish EPD at varying temperatures, 20 ml of exfoliated TMD solution was heated to the specified temperature on a hot plate. Temperature was recorded directly from solution using a K-type thermocouple. After reaching the desired temperature, two 316 stainless steel electrodes of dimensions 1.0 cm x 3.0 cm were immersed directly into the heated solution at a separation of 0.5 cm and left to rest for 5 minutes to obtain equilibrium with the solution before a constant voltage of specified magnitude was applied for 2 minutes. The resulting films were placed directly in a vacuum oven at 60 ^{o}C to dry overnight.

Absorption measurements were performed using a Varian Cary 5000 UV-VIS NIR spectrometer. To measure sedimentation, exfoliated solutions were sonicated for 5 minutes before placement into the UV-VIS. Spectra were then recorded once every minute for a period of 5 minutes. To measure absorption of solutions before and after EPD, purified solutions were first fabricated and then placed directly into the UV-VIS. EPD was then performed on the remaining material with stainless steel electrodes at a separation of 0.5 cm under an application of 200 V for 30 minutes. After removal of the electrodes, the remaining solution was bath sonicated for ~1 minute and then placed into the UV-VIS.

Zeta potential and particle size measurements were obtained from a Malvern Zetasizer Nano ZS instrument. Solutions were left to rest overnight to ensure removal of large sedimenting particles that complicate DLS measurements. The upper 1/3 of the solution was harvested and placed into a low-power bath sonicator for 30 minutes before placement into the Zetasizer. A Renishaw inVia MicroRaman system with a 785 nm excitation laser performed Raman characterization of the assembled films.

4.3 Liquid Phase Exfoliation of Layered Materials

MoS_2, and TMDs in general characteristically possess a unique layered structure in which covalently bonded planes of transition metals (e.g. Mo) and chalcogens (e.g. S) atoms are held together through weak van der Waals interaction. This unique atomic architecture enables facile exfoliation of the material to ultra-thin structures as small as one layer thick when starting with bulk materials and using the appropriate solvents.[51] In recent years, significant research progress has been made toward top-down liquid-phase dispersion of 2-D materials starting from commercially available bulk materials.[52, 53] Whereas chemical processing routes designed to exfoliate bulk 2-D materials are observed to chemically alter or degrade the intrinsic properties of the starting material,[54, 55] exfoliation routes relying on the use of mechanical (sonication) dispersion techniques in chemically-inert liquid media have indicated the ability to preserve the unique properties of 2-D layered materials such as MoS_2.[56] Despite significant advances in this area, liquid processing of MoS_2 nanosheets for many applications is challenged by substantial polydispersity in exfoliated materials that mandates purification and leads to low yields of thin nanosheets[57] in addition to the imposed requirement of subsequent assembly routes to form controllable and uniform macroscopic functional materials. In this regard, EPD represents an attractive route for the assembly of 2-D nanosheets due to the compatibility of EPD with a broad range of substrates and substrate topologies.[15, 31] Due to the inherit charge present on nanomaterials in solution, EPD presents a simple and expeditious assembly route which takes advantage of this natural charging mechanism to produce tightly packed, site-selective and size-scaleable films of nanomaterials stabilized by short-range van der Waals interaction. Furthermore, recent studies have emphasized the ability to perform EPD of low-dimensional nanostructures directly from polar solvent dispersions without surfactants or additives. [42, 58, 59] Therefore, EPD is a process that could be synergistically combined with exfoliation processes to enable assembly in a one-batch approach while also potentially overcoming limitations in current exfoliation processes, such as the low yields and poor selectivity of exfoliated nanosheets. This yields a road-map toward producing functional materials composed of 2-D building blocks with simultaneous optimization capability across parameters of assembly kinetics (throughput), exfoliation characteristics (quality), and solvent cost and reusability (scalability).

The general process for the exfoliation and assembly of MoS_2 nanostructured material is schematically presented in Figure 4.1a. Commercially available MoS_2 powders are dispersed in solvent and exfoliated through probe sonication to produce dispersions of exfoliated MoS_2 NSs. Electrodes are then placed in the resulting solution and EPD is performed on both 2-D (stainless steel) and 3-D (nickel foam) electrodes. This approach yields a one-batch process where exfoliation and assembly can occur sequentially with the two processes combined to directly produce and assemble functional TMD nanomaterials. EPD processes following solvent exfoliation leads to the capability to produce homogenous films that can be applied to both planar and 3-D porous substrates (Figure 4.1b). Scanning electron microscopy (SEM) characterization of MoS_2 films assembled on these two geometries is presented in Figure 4.1b,c. From these images it is evident that the films generated from this EPD process are uniform across the entire substrate and are composed exclusively of exfoliated 2-D TMD nanosheets.

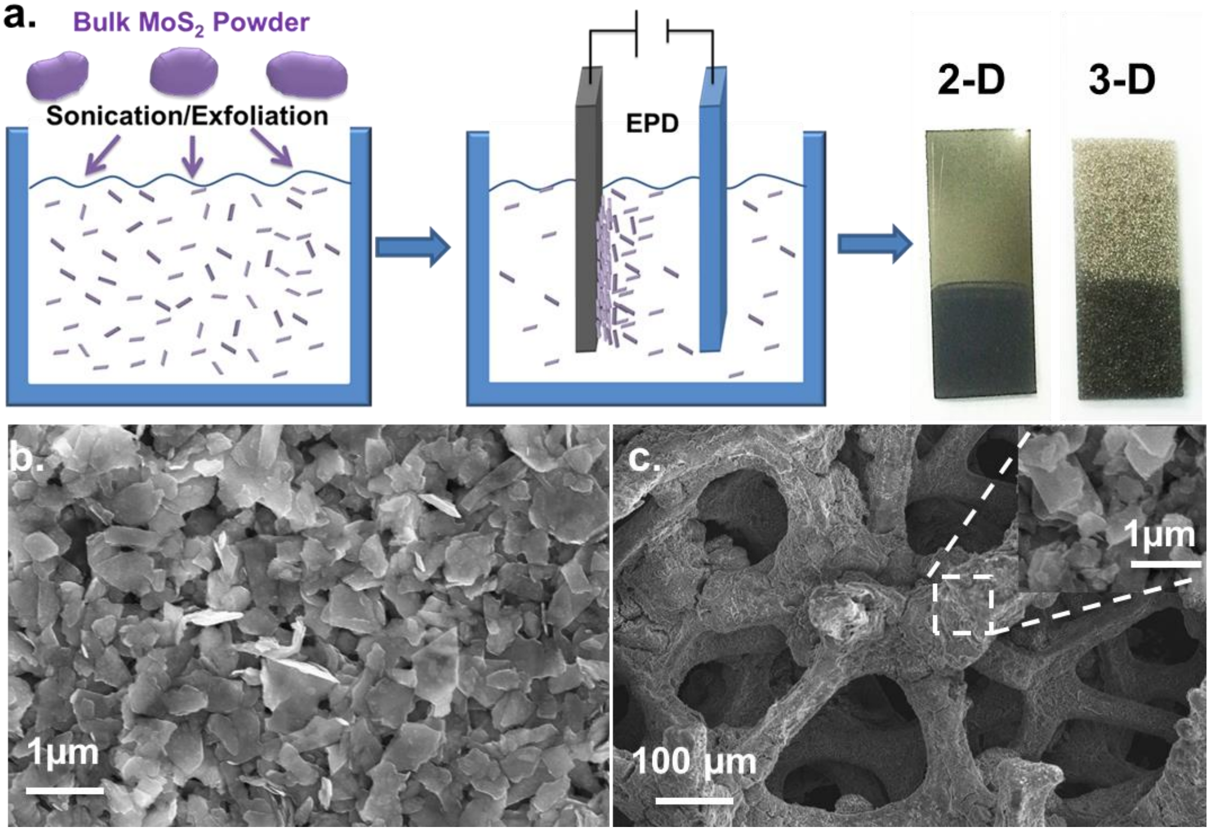

Figure 4.1. (a) Schematic of the exfoliation/assembly process. Bulk TMD powder is sonicated in solution to produce a dispersion of nanosheets which is then deposited on 2D and 3D substrates using EPD. (b) SEM characterization of TMD films assembled on 2D and (c) 3D substrates. The inset in (c) provides nanoscale characterization of the 3D assembled films.

In order to broadly assess the ability to combine the exfoliation and assembly steps for TMD materials, two solvents that are most commonly employed for exfoliation processes were identified. In general, solvents capable of exfoliating 2-D materials are characterized by surface tensions that coincide with the surface energy of the dispersed nanomaterial.[9, 52] In this manner, both NMP and ACN were chosen for this study due to the widespread use of NMP, a surface tension for both solvents that closely matches the majority of TMD materials studied thus far (~40.8 mN/m for NMP at 20 ^{o}C and ~29.3 mN/m for ACN at 20 ^{o}C), and previous studies that have identified these two solvents as capable exfoliating mediums.[60] Notably, previous studies have indicated both ACN and NMP as viable solvents for EPD processes without the use of surfactants or additives.[42, 61] Additionally, a series of three TMD materials including MoS_2, $MoSe_2$, and WS_2 were chosen which generally represent three of the most studied TMDs for electrochemical applications.[62, 63] Using this series of TMD materials and two commonly employed solvents for exfoliation, combined exfoliation and EPD was performed onto planar stainless steel surfaces for all cases. SEM images of the resulting films that indicate both the quality of the exfoliation as well as the effectiveness of EPD in forming homogenous coatings are shown in Figure 4.2a-f.

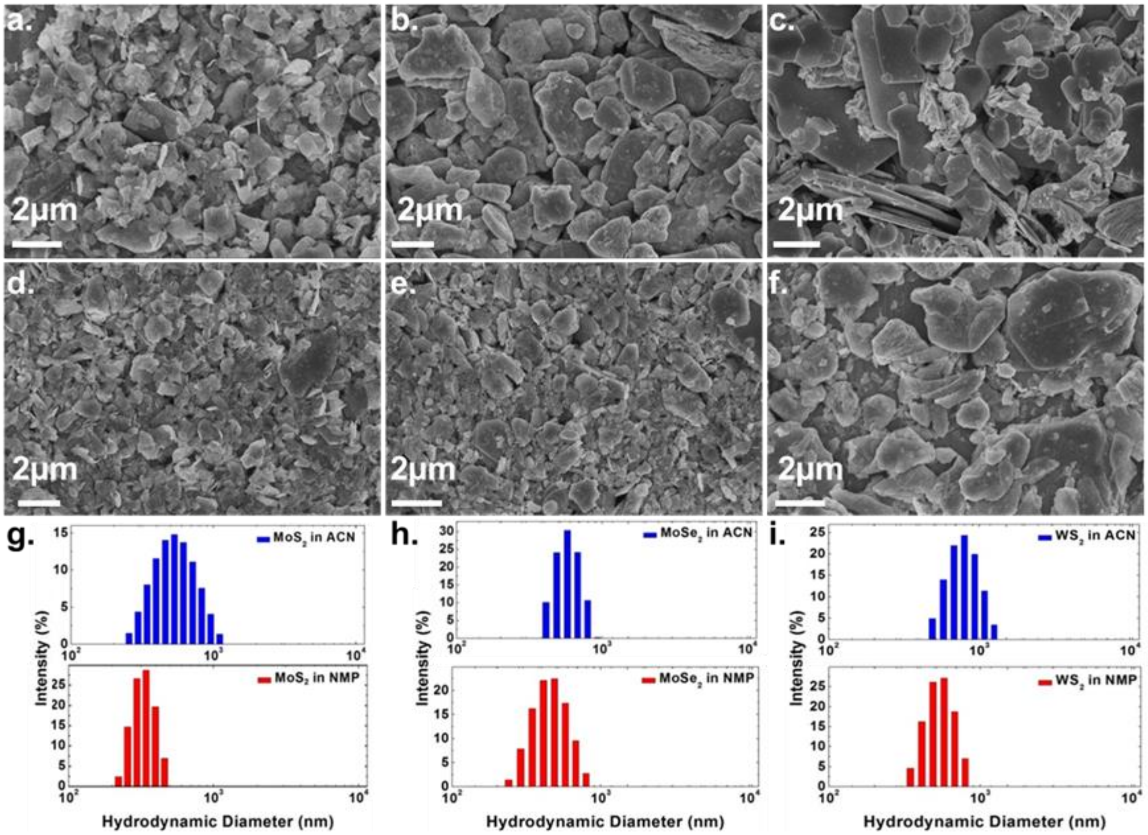

Figure 4.2. SEM characterization of EPD films assembled from a 2 minute application of a constant applied potential of 200V for (a) NMP-MoS2 (b) NMP-MoSe2 (c) NMP-WS2 (d) ACN-MoS2 (e) ACN-MoSe2 and (f) ACN-WS2 films. DLS characterization of the size distribution of exfoliated flakes from supernatant solutions of ACN and NMP suspensions of (g) MoS2 (h) MoSe2 and (i) WS2.

Hydrodynamic diameter measurements using a dynamic light scattering (DLS) technique measure the radius of a sphere in solution with equal volume to the mean NS volume and have recently been shown to be closely related to exfoliated nanosheet size.[64] DLS measurements of the exfoliated dispersions (Figure 4.2g-i) further confirm the presence of ultra-thin TMD materials. Average measured nanosheet sizes are (*i*) MoS_2: 340.1 nm for NMP and 580.1 nm for ACN, (*ii*) $MoSe_2$: 338.3 nm for NMP and 408.8 nm for ACN, and (*iii*) WS_2: 386.9 nm for NMP and 544.0 nm for ACN. Cross-sectional SEMs for TMD films formed at 200 V from NMP solutions are presented in Figure 4.3 and demonstrate these films to be composed primarily of exfoliated nanosheets with parallel stacking to improve packing density.

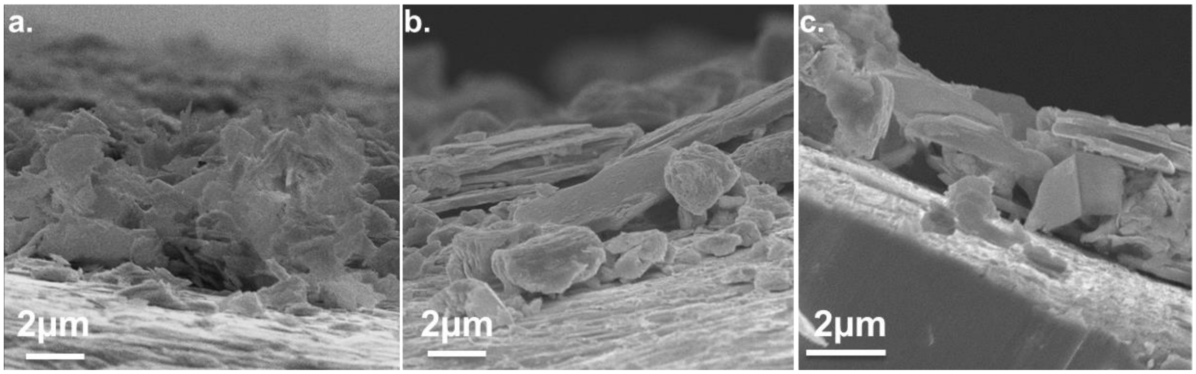

Figure 4.3. Cross-sectional SEM of the assembled films for NMP depositions of (a) MoS_2 (b) $MoSe_2$ and (c) WS_2.

To gauge the effect of exfoliation and assembly on the chemical properties of the assembled films, Raman spectroscopic analysis was performed using a 785 nm laser excitation (Figures 4.4a,b). Analysis of the spectra generally indicates that sonication in NMP tends to chemically alter the MoS_2 and $MoSe_2$ nanosheets, whereas the WS_2 nanosheets tend to exhibit Raman modes that remain invariant between the subsequent exfoliation and assembly treatments. Specifically, MoS_2 nanosheets exfoliated in NMP exhibit a greater intensity of the peak centered at ~237 cm^{-1} (compared to ACN) which is attributed to the formation carbon-sulfur bonds[65] and is indicative of organic NMP carbonaceous residues forming during the sonication process. Similarly, the $MoSe_2$ nanosheets exfoliated in NMP (compared to ACN) demonstrate significant enhancement to the peaks at ~288 cm^{-1}, 451 cm^{-1}, and 591 cm^{-1} which can also be attributed to formation of carbon-selenide bonds.

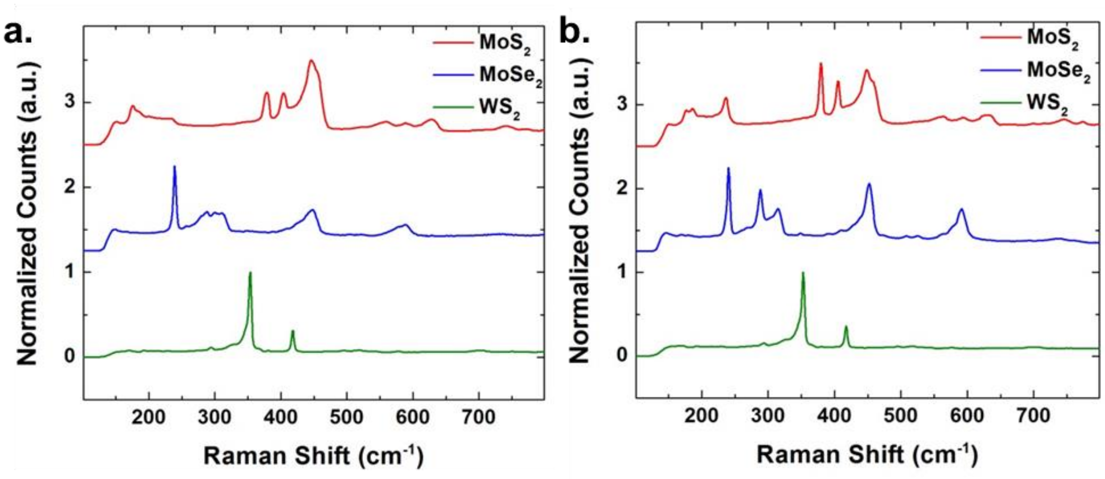

Figure 4.4. Raman analysis of MoS_2, $Mose_2$ and WS_2 after exfoliation in (a) NMP and (b) ACN.

One of the key principles for an EPD process to be effective is the degree of electrostatic stability of the particles in solution. This can be assessed through measurements of the particle zeta potential, representing the magnitude of the electrostatic charge present at the surface of shear for each particle as it moves through solution. Shown in Figure 4.5 is the measured zeta potential for nanosheet suspensions in both NMP and ACN. This indicates that zeta potential values for the individual materials varies only slightly between the two solvents with MoS_2 consistently exhibiting the smallest magnitude (-33.7 mV and-34.6 mV in NMP and ACN, respectively) and $MoSe_2$ (-40.4 mV and -40.0 mV) and WS_2 (-41.1 mVand -42.2 mV) the largest with comparable magnitudes. These measured solute properties together with the inherit properties of the suspending solution can be used to calculate the electrophoretic mobility, μ, using the Smoluchowski equation for electrophoretic mobility:[31] Although this approximation is designed for spherical particles, it is closely related to the mobility expression for rigid particles with high aspect ratios.[66]

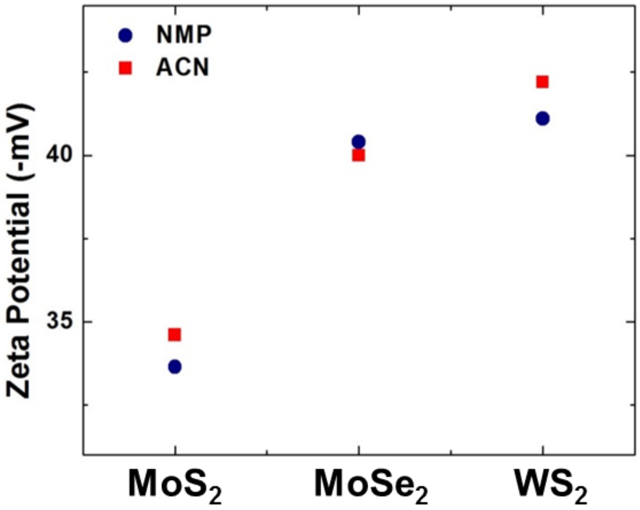

Figure 4.5. Zeta potential measurements of exfoliated TMDs in both ACN and NMP.

4.4 EPD Assembly of Exfoliated Materials

From the Smoluchowski approximation, it is evident that a solution with lower viscosity and a higher dielectric constant will result in a dispersion of particles with higher electrophoretic mobility. Calculated mobility values for the exfoliated TMDs in these two solvents are shown in Table 4.1. Notably, suspensions of exfoliated TMDs in ACN possess ~5x greater mobility than suspensions in NMP.

Solvent	Dielectric Constant	Viscosity (cP)	MoS_2 mobility ($m^2V^{-1}s^{-1}$)	$MoSe_2$ mobility ($m^2V^{-1}s^{-1}$)	WS_2 mobility ($m^2V^{-1}s^{-1}$)
NMP	33	1.7	5.78×10^{-9}	6.94×10^{-9}	7.06×10^{-9}
ACN	38	0.34	2.61×10^{-8}	3.02×10^{-8}	3.18×10^{-8}

Table 4.I. List of solution properties and particle mobilites calculated in both ACN and NMP.

To characterize the EPD kinetics of these materials, experiments were performed in whih deposition rates from these two solvents were measured as a function of applied voltage (Figure 4.6a,b). For MoS_2 materials, the deposition rate is observed to possess the expected near-linear dependence on particle mobility with mass accumulation closely approaching the theoretically predicted value for the two solvents using estimations derived from particle mobility (Figure 4.6c). However, $MoSe_2$ and WS_2 exhibit unpredictably poor deposition behavior in ACN compared to NMP. This non-linear dependence of $MoSe_2$ and WS_2 deposition rates on particle mobility is chiefly attributed to the poor suspension quality in ACN relative to NMP due to the lower buoyancy force in this low density solvent.

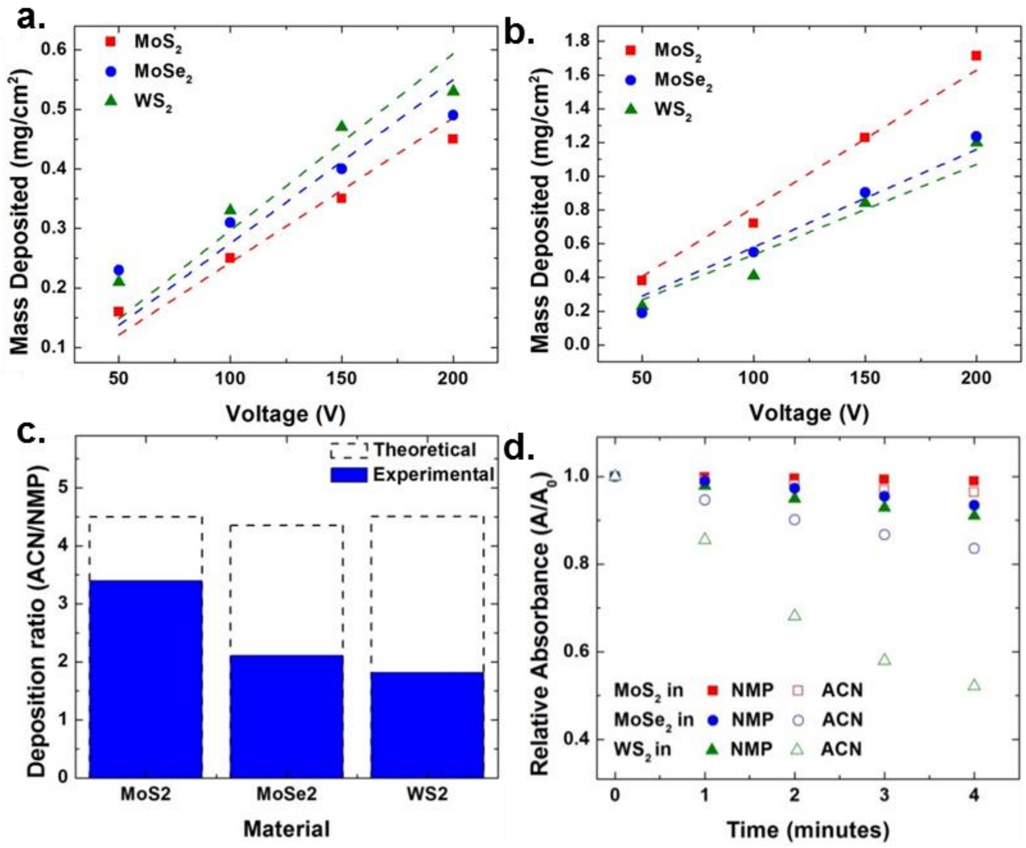

Figure 4.6. Mass deposition as a function of applied voltage for TMD solutions on 2D substrates from (a) NMP and (b) ACN, the dotted lines in the figure represent fits to the data using the Hamaker approximation. (c) Theoretical prediction of the ratio of the deposition rates for ACN to NMP plotted against the observed values obtained from model fits to the Hamaker model.(d) Change in concentration of the TMD solutions over time as the solution is left to settle.

Model fits to the mass deposition data using equation 1 and the parameters listed in table I are presented as dotted lines in Figure 4.6a,b. The sticking factor was slightly adjusted to produce tight fits to the data, with sticking factors for MoS_2, $MoSe_2$, and WS_2 of 0.35, 0.32, and 0.35 respectively in NMP compared with 0.26, 0.16, and 0.14 respectively in ACN. The large disparity in sticking factor values for ACN depositions is attributed to the substantial and material-dependent influence of sedimentation.

Figure 4.6d presents absorbance data for dispersions of TMDs in NMP and ACN over a period of 4 minutes. The correlation between solution absorbance and suspension concentration allow for the estimation of sedimentation rate by the change in absorbance over time[67]. From the data in Figure 4.6d it is evident that suspensions in ACN sediment at a substantially greater rate than in NMP and that WS_2 and $MoSe_2$ demonstrate significant sedimentation over the 2 minute deposition period compared with NMP. The magnitude of change in sticking factor values found to be directly related to the degree of sedimentation, with more heavily sedimenting particles producing smaller sticking factor values. In all cases, however, good agreement is generally observed between the Hamaker model for particle deposition and our experimental data for exfoliated TMD nanosheets indicating that changes in field strength due to the resistivity of the growing semiconducting TMD film are negligible on small timescales. Additionally, the representative current profiles provided in Figure 4.7a,b demonstrate conductivity values that fluctuate about the initial value indicating the absence of parasitic side reactions or the production of heavily insulating films. This behavior indicates constant-voltage EPD is well-suited for the assembly of TMD NSs from solution.

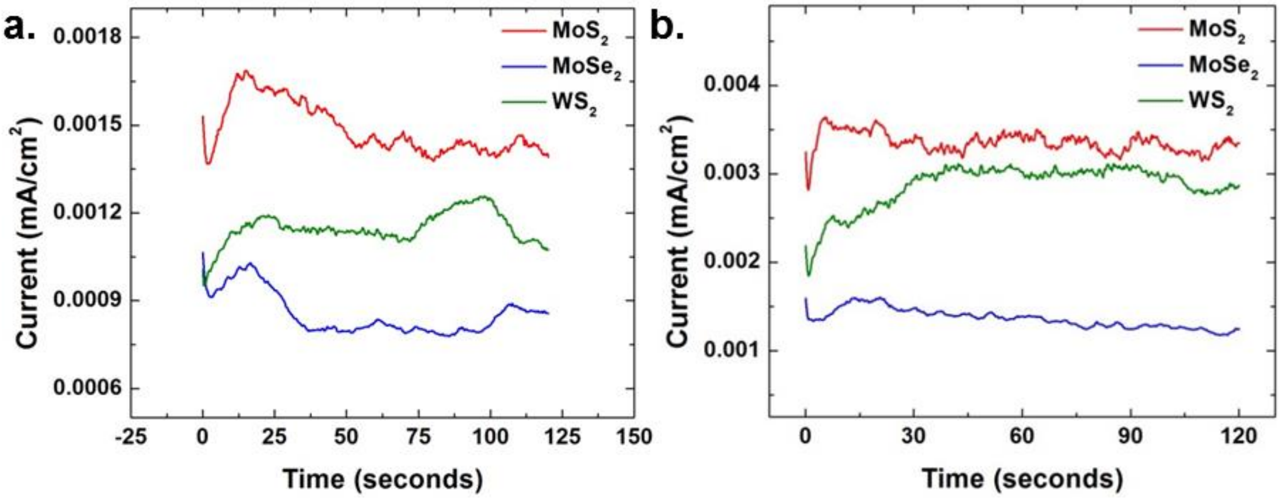

Figure 4.7. Current density measured during the EPD process for 200V deposition in (a) NMP and (b) ACN.

The primary advantage of EPD over other solution processing techniques is the unique ability to form conformal coatings on complex 3-D substrates. To emphasize this ability in the context of exfoliated TMD nanosheets, EPD was performed on a conducting nickel foam substrate for NMP TMD solutions. NMP was chosen as the suspending solvent due to the demonstrated stability of NMP dispersions and the better exfoliation properties that is advantageous for uniform penetration into a 3-D substrate. Similar to deposition on 2-D substrates, the deposition yield followed the trend of WS_2 > $MoSe_2$ > MoS_2 as expected by the calculated particle mobilities (Figure 4.8a). Additionally, over 2x more material is deposited for identical deposition conditions when moving from 2-D to 3-D substrates as expected by the presence of additional surface area in the 3-D substrate. To confirm infiltration of TMDs into the interior of the foam, optical and SEM characterization was performed on nickel foams coated by MoS_2 and is presented in Figure 4.8b. The optical photograph of a cross-section of nickel foam emphasizes the presence of a TMD coating in the interior of the foam while SEM characterization present in the inset confirms this coating to be composed of exfoliated NSs.

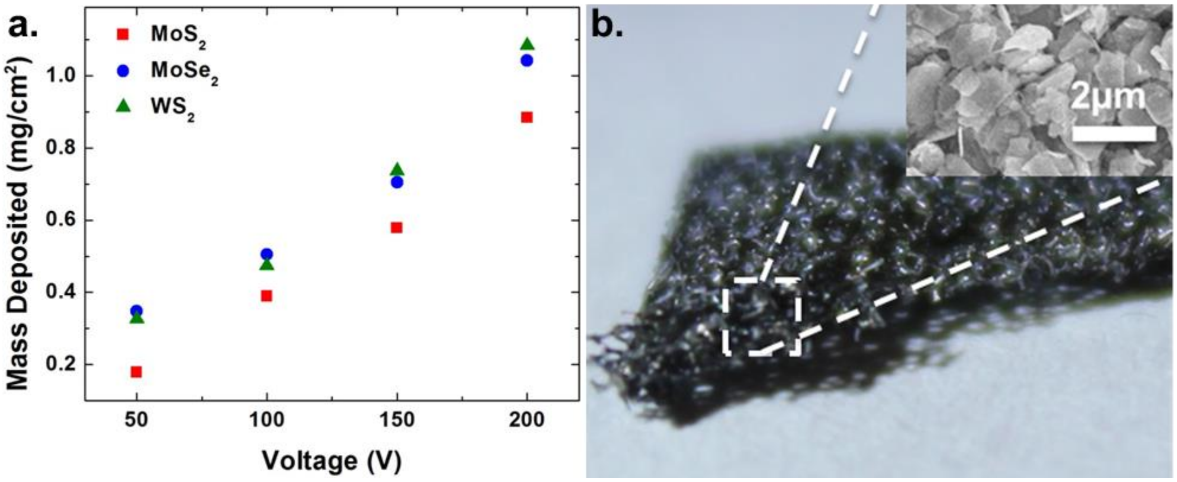

Figure 4.8. (a) Mass deposition as a function of applied voltage for NMP dispersion assembled on 3D nickel foam electrodes. (b) Optical image of a cross section of the MoS2-coated nickel foam emphasizing complete coating of the substrate during EPD. The inset in (b) displays SEM characterization of the material assembled on the nickel foam.

So far in this chapter, the assembly behavior of TMD nanosheets has been analyzed based on dispersions that are formed directly after exfoliation with no additional purification steps. However, many applications of TMD nanosheets rely on the unique properties of single to few-layer architectures that possess unique electronic, optical, and chemical features not achievable in bulk. However, processing of solutions to achieve these highly purified dispersions requires centrifugation cycles that lead to extremely low solution concentrations. These low concentration solutions can be challenging to assemble into macroscopic films using traditional routes of drop drying or spin-casting due to the low-efficiency and lack of controllability of these processes. However, EPD is demonstrated to be a convenient method to assemble thick films from these dilute solutions due to the unique ability to completely assemble all suspended materials in a single processing step. To explicitly demonstrate this, absorption properties of purified solutions in ACN before and after EPD were characterized and the results are presented in Figure 4.9a-f. Characteristic absorption spectra for purified solutions of MoS_2, $MoSe_2$ and WS_2 nanosheets are present in the tested solutions, where the concentration of dispersed nanosheets is directly proportional to the observed absorbance. After the application of 200 V between two electrodes immersed in ACN solution for 30 minutes, the absorption of the remaining solution is reduced by 100% to the accuracy of the UV-Vis-NIR spectrometer, indicating complete removal of the suspended nanosheets into the assembled film. Additionally, a uniform film is observed on the deposition electrode and SEM characterization reveals the presence of ultrathin MoS_2 NSs (Figure 4.9g-h). This indicates that ACN is an efficient solvent for high efficiency conversion of suspensions of high quality nanosheets into assembled electrode materials. Identical experiments performed using purified solutions in NMP did not result in complete removal of material even after extending the deposition to 1.5 hours. Small observed changes to the absorption spectra of these solutions implies that in the regime of low concentration purified nanosheets, the solution properties of NMP cause the low mobility to be a bottleneck for complete transference of suspended nanosheets to an assembled material.

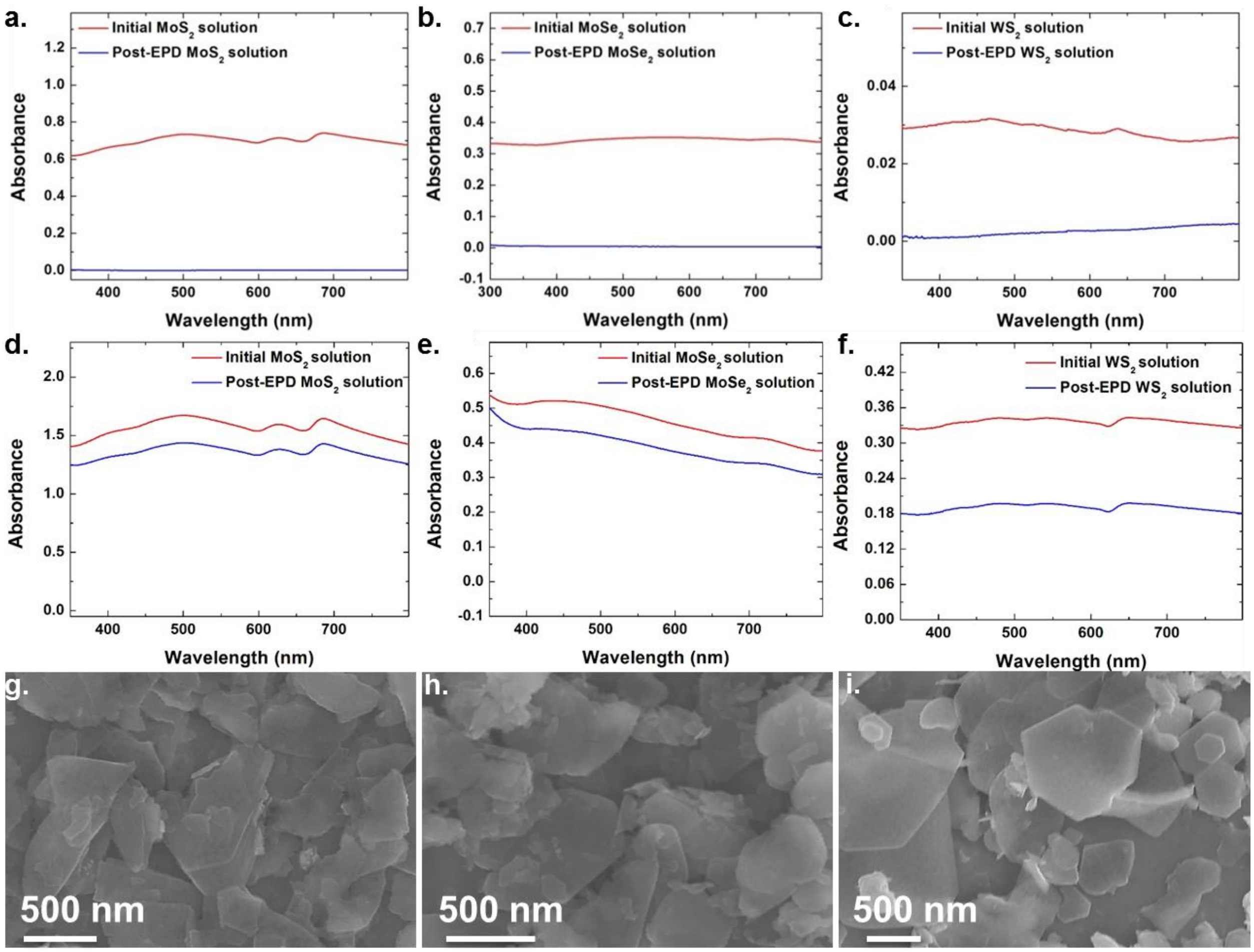

Figure 4.9. Absorbance spectra for purified TMD solutions in ACN before and after EPD at 200V for 30 minutes for (a) MoS_2 (b) $MoSe_2$ and (c) WS_2. Absorbance spectra for NMP solutions under the same conditions at extended times for (d) MoS_2 (e) $MoSe_2$ and (f) WS_2. SEM characterization of the films assembled from ACN for (g) MoS_2 (H) $MoSe_2$ and (I) WS_2.

Whereas this indicates that EPD from low-concentration solutions of TMD nanosheets dispersed in NMP are mobility-limited, the possibility to improve deposition kinetics is demonstrated by engineering the solution properties of the dispersing solution. To demonstrate this idea, the ability to use solution temperature of NMP during deposition as a means to modify the solution viscosity, and hence the electrophoretic mobility is presented. In particular, the heating of a solution increases the average kinetic energy of molecules, decreasing the intermolecular force between neighboring molecules that is manifested macroscopically as a decrease in total solution viscosity. To investigate this effect on the electrophoretic mobility of suspended nanomaterials, EPD was performed at 5 separate temperatures and the results are presented in Figure 4.10a. The general trend observed during this study is a consistent increase in deposition rate with temperature. Whereas this improvement in deposition rate may be chiefly attributed to the viscosity, other factors such as changes in the dielectric permeability, suspension solubility, and solution conductivity could also play a role in the resulting deposition rate. Raman characterization for films formed at 125°C from NMP suspensions demonstrate identical characteristics as those formed at 25°C implying elevated temperatures do not lead to increased residue formation from the solvent or increased amounts of structural damage to the nanosheets during deposition (Figure 4.10b).

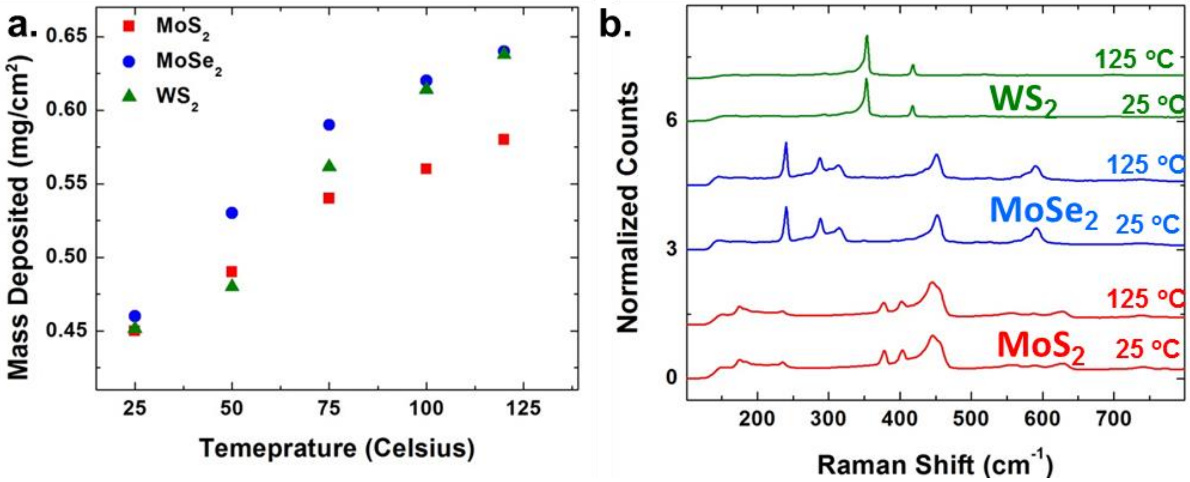

Figure 4.10. (a) Temperature dependence of the deposition rate for 200V constant-voltage EPD experiments at a constant time of 2 minutes. (b) Raman analysis of the films formed at 125 °C (upper) 25 °C (lower).

4.5 Conclusion

In this chapter, the utility of electrophoretic deposition (EPD) as a tool to complement conventional exfoliation routes for one-batch assembly of functional TMD coatings is demonstrated. The success of this approach is crucial in demonstrating that nanoscale TMD materials (such as MoS2) may be assembled into functional coatings of material using a cost-competitive approach. Comparing one-batch exfoliation and assembly processes in both NMP and ACN suspending solvents, it is observed that the use of ACN enables faster EPD assembly kinetics (2-3x), more pristine NS deposits based on Raman spectroscopy analysis, and the capability for complete extraction of all dispersed TMDs to a film using EPD. Whereas NMP exhibits improved exfoliation properties, ACN is identified as an improved solvent for the combined process of exfoliation and EPD assembly due to these points. It is further demonstrated that external stimuli, such as temperature, can be used to modulate the solution properties of NMP dispersions and improve the assembly kinetics without incurring additional damage or residue. This work identifies for the first time that EPD is a versatile tool that can be directly combined with 2-D nanosheet exfoliation processes to yield one-batch solution processing to transform bulk powders into functional coatings of nanosheets. This opens routes toward achieving surfactant- or additive-free macroscopic assembled materials based on a broad family of 2-D TMD nanosheet building blocks for applications across a vast range of areas including energy storage, energy conversion, sensing, catalysis, photodetection, among others.

CHAPTER 5

Strain Engineering MoS_2 for Suitable Cathode Energetics

5.1 Introduction

The previous chapter demonstrated methods for using low-cost material synthesis routes to directly assemble nanostructured, 2-D materials from low-cost bulk materials. As emphasized in Chapter 3, such materials hold exceptional promise as a cathode material for a full-cell Li-ion batteries, however, the performance observed in this chapter fell drastically short of the promise of the layered MoS_2 cathode reported in half-cell configurations. The reason for this poor performance is the poor efficiency of the cathode conversion reaction when paired with conventional anode materials. Electrochemical investigations into the working mechanism of MoS_2 as a cathode material has revealed a conversion reaction in MoS_2 that persists down to potentials as low 0.0 V vs. Li/Li+ as the formed discharge products undergo complete reduction and conversion. Unfortunately however, the pairing of this material with conventional anodes, such as Si or graphite prohibit the realization of such low voltages in a full cell configuration. For this reason, methods to tune the conversion reaction to occur at a significantly higher reduction potential are desirable in order to realize the full potential of this material in a full cell Li-ion battery.

In this chapter, methods for optimizing the performance of MoS_2 materials for full-cell applications will be presented by tuning the Faradaic potential and the efficiency of the MoS_2 conversion reaction during the initial discharge. By utilizing the well-known method of strain-engineering, the reaction energetics of MoS_2 and lithium will be engineered in order to ensure compatibility with present-day anode materials. By applying a thin carbon layer using high-temperature chemical vapor deposition, interfacial strain imparted on the underlying MoS_2 material will facilitate the conversion reaction at potentials as high as 2.0 V vs. Li/Li^+. The results presented in this chapter open up an entirely new field for electrochemical energy storage in which physical properties such as strain may be used to alter and improve the electrochemical properties of Li-ion electrode materials.

5.2 Experimental Methods

To fabricate the MoS_2 nanosheets for this study, 500 mg of bulk MoS_2 powder (Aldrich, particle size < 2μm) were added to 50 ml of 1-methyl-2-pyrrolidinone (Aldrich, 99.5% anhydrous). The solution was sonicated in a bath sonicator for 12 hours using 8 x 90 minute intervals. After sonication, the solution was centrifuged at 2,000 rpms for 40 minutes. The upper 2/3 of the supernatant was removed and subsequently centrifuged for 1 hour at 5,000 rpms before the excess supernatant was removed and the accumulated nanosheets were placed under vacuum overnight to completely evaporate the solvent.

In order to generate vertically stacked carbon - MoS_2 (C- MoS_2**)** nanosheets MoS_2 nanosheets contained within an alumina boat were placed into a 1” tube furnace and the tube was evacuated to 2 mTorr. A gas mixture of 100 sccm Ar and 20 sccm H_2 maintained at atmospheric pressure were introduced during ramping to a temperature 750°C. At 750°C, 2 sccm of acetylene (C_2H_2) was introduced for 10 minutes followed by a temperature ramp to 850°C and an additional 10 minute soak, and a final ramp to 950°C for 10 minutes. After this process, the acetylene was turned off and the furnace cooled back down under a flow of argon and hydrogen where materials were removed.

Electrode materials were fabricating by suspending 20 mg of vertically stacked C-MoS_2 or pristine MoS_2 nanosheets were in 20 ml NMP and sonicating for 30 minutes. Following this, a stainless steel spacer was placed at 0.5 cm from a 1 cm x 1 cm stainless steel counter electrode. A voltage of 30 V was applied for 30 minutes before carefully removing the coated steel electrode from solution and placing this into a vacuum chamber overnight to dry the sample.

Electrochemical half-cell devices were assembled in an argon glovebox using CR 2032 stainless steel coin cells purchased from MTI. The coated steel discs were separated from a lithium metal anode by a 2500 Celgard separator saturated with a 1 M $LiPF_6$ in 1g/1 ml solution of ethylene carbonate (EC) and diethyl carbonate (DEC). Cyclic voltammetry scans and galvanostatic measurements were performed using a Metrohm autolab multichannel testing system. Raman measurements were performed using a Renishaw inVia confocal Raman spectrometer. Micro-Raman maps were collected using a 532 nm laser. Prior to characterizing the electrodes after electrochemical testing, coin cells were disassembled in an Ar filled glove box and the electrodes washed with an EC/DEC solution.

5.3 Electrochemical Behavior of MoS_2 for Li-ion batteries.

As a bulk, sulfur-containing material, MoS_2 represents an easily processed material structure that is able to be directly incorporated as a cathode materials. Due to the sulfur-based lithium storage reaction, this material is capable of achieving energy densities on par with next generation sulfur cathodes with capacities as high as 1,100 mAh/g reported for nanostructured materials. During operation as a Li-ion battery electrode, MoS_2 converts into Mo and Li_2S particles after the first cycle and subsequent reactions of this material store lithium at ~2.1 V vs. Li/Li^+. Due to the high voltage of the lithiation reaction, this material is capable of being paired with traditional anode materials such as graphite or silicon, which store lithium at voltages < 0.3 V vs. Li/Li+, in order to fabricate a full-cell Li-ion battery with a reasonable operating voltage. However, in order to convert MoS_2 into the active Mo and S components a conversion reaction during the initial discharge is required which inhibits the ability of this material to be directly implemented into a cathode material system. For pristine MoS_2 NSs formed using LPE, two concurrent reactions in the initial discharge are observed, with the first one at ~ 1.1 V and the second at ~ 0.55 V vs. Li/Li^+. Figure 5.1a presents a typical discharge curve for the initial discharge of a pristine MoS_2 cathode operated against a Li metal anode. In Figure 5.1b, a differential capacity plot fabricated using the data of Figure 5.1a is presented that highlights the location of these initial electrochemical reactions as MoS_2 is discharged. The reactions obtained here are consistent with the known pathways for insertion of lithium into pristine MoS_2, which occurs first through an intercalation reaction (1.1 V) that follows

$$MoS_2 + xLi^+ + xe^- = Li_xMoS_2 \qquad \text{(equation 5.1)}$$

where MoS_2 undergoes a transition from a semiconducting 2H phase to the strained, metallic 1T phase due to deformation of the crystal from lithium ion insertion. Following this transition, the MoS_2 can undergo a subsequent conversion reaction at lower voltages (0.55 V) that follows

$$Li_xMoS_2 + 4Li^+ + 4e^- = 2Li_2S + Mo/Li_y \qquad \text{(equation 5.2)}$$

These processes are outlined schematically in Figure 5.1c. Unfortunately, the location of this low voltage conversion reaction occurs at a similar potential to that of Li-ion intercalation in traditional anode materials such as graphite or silicon. Therefore, in order to directly implement MoS_2 as a cathode material, pre-treatment of the MoS_2 to convert it into the active material components must take place before pairing this material with an anode, adding significant complexity to the full-cell fabrication.

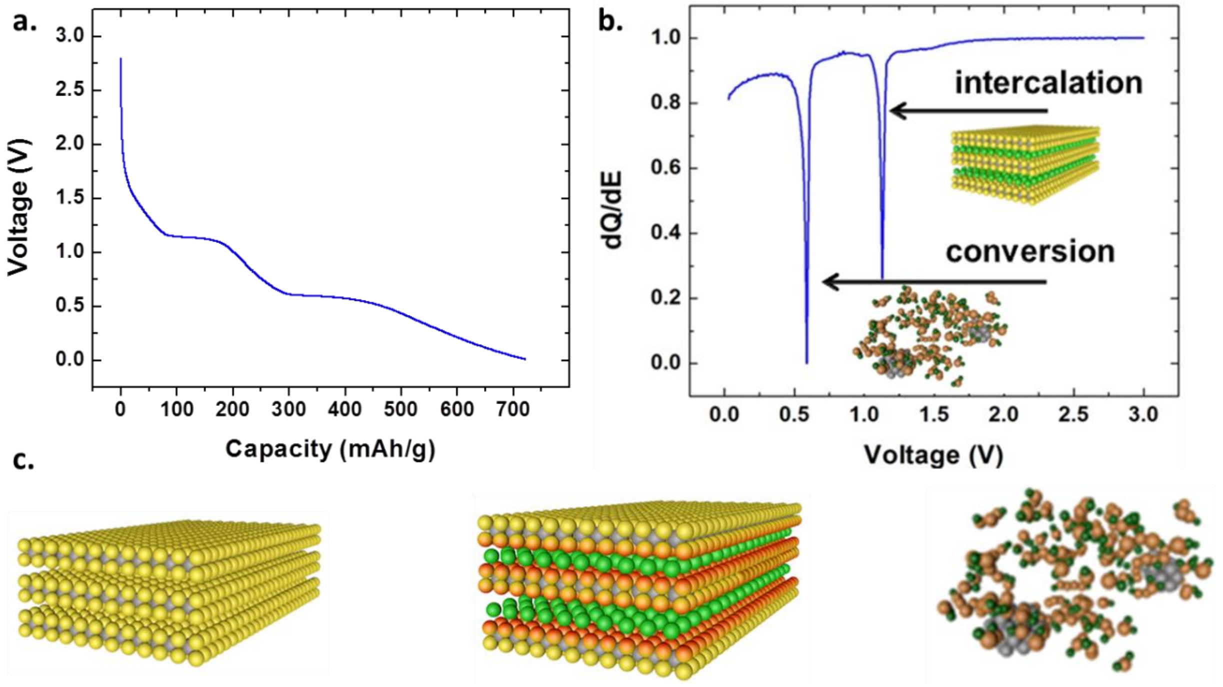

Figure 5.1. (a) Initial discharge curve for a pristine MoS_2 NS and corresponding DQ/DE plot in (b) highlighting the reactions present in the discharge curve. (c) schematic illustration of the pristine MoS_2 conversion reaction process.

5.4 Strain Engineering MoS_2 Materials for Suitable Cathodes in Li-ion Batteries

As emphasized in the reaction scheme of Figure 5.1c, a precursor to the conversion reaction in MoS_2 materials is the presence of a strained MoS_2-lithium interface during intercalation at ~1.1 V. Due to the nature of 2-D materials, however, strain may be imparted to this structure through other means such as interfaced coatings. In semiconductor electronics, engineering 2D materials using strain applied at an interface has been shown to strongly modulate the bandgap and band structure, which results in modified electrical and optical properties for strained materials.[68-73] For monolayer MoS_2, the bandgap is observed to shift by up to 15 meV under tensile strain of up to 4.8%[74] and theoretical efforts have further emphasized strain enabled broadband absorption and photodetection in MoS_2, even though this has not yet been experimentally realized.[75] The intersection of strain engineered properties of 2D materials and the impact on electrochemical storage properties presents an engaging research area for next-generation electronics and has only recently been explored for electrochemical devices.

Unlike electronic devices, however, the application toward energy storage electrodes requires bulk-like quantities of 2D materials – a challenge aided by recent developments in the liquid exfoliation and assembly of layered TMDCs.[76, 77] However, addressing how properties in heterostructured or complex 2D materials can impact chemical processes responsible for electrochemical applications is hampered by uniform material fabrication routes that can be employed on scales required for electrochemical measurements. As a result, the impact of strained interfaces in 2D materials on chemical and electrochemical processes remains virtually unstudied. Only recently has an observation emerged that compressive strain on Pt catalysts can improve the oxygen reduction reaction capability of Pt relevant to fuel cells.[78] In this manner, 2D materials provide an ideal test bed for the understanding of how interfaces and strain can impact electrochemical processes, motivated by pioneering efforts in the field of semiconductor electronics. Using the application of interface strain, attempts are made to tune the electrochemical conversion reaction of MoS_2 to enable a direct pairing of this material with anode materials for Li-ion battery full-cell electrodes. Due to the favorable properties of carbon materials for electrochemical devices, applied strain was controlled through the application of a controlled carbon layer. As mentioned in the previous chapter, extended exfoliation processes using high temperatures and low concentrations of material can initiate a carbon coating through a catalyzed decomposition of the suspending solvent – enabling the potential for one batch processing of these carbon- MoS_2 nanostructures. However, for the present study, this method of applying a carbon coating was found to be difficult to control and requires further research in order to optimize the in-situ formation of a carbon- MoS_2 interface through solution processing methods. In order to demonstrate the applicability of carbon to apply the necessary strain, more controlled methods of carbon layer formation, namely chemical vapor deposition, were employed for this study.

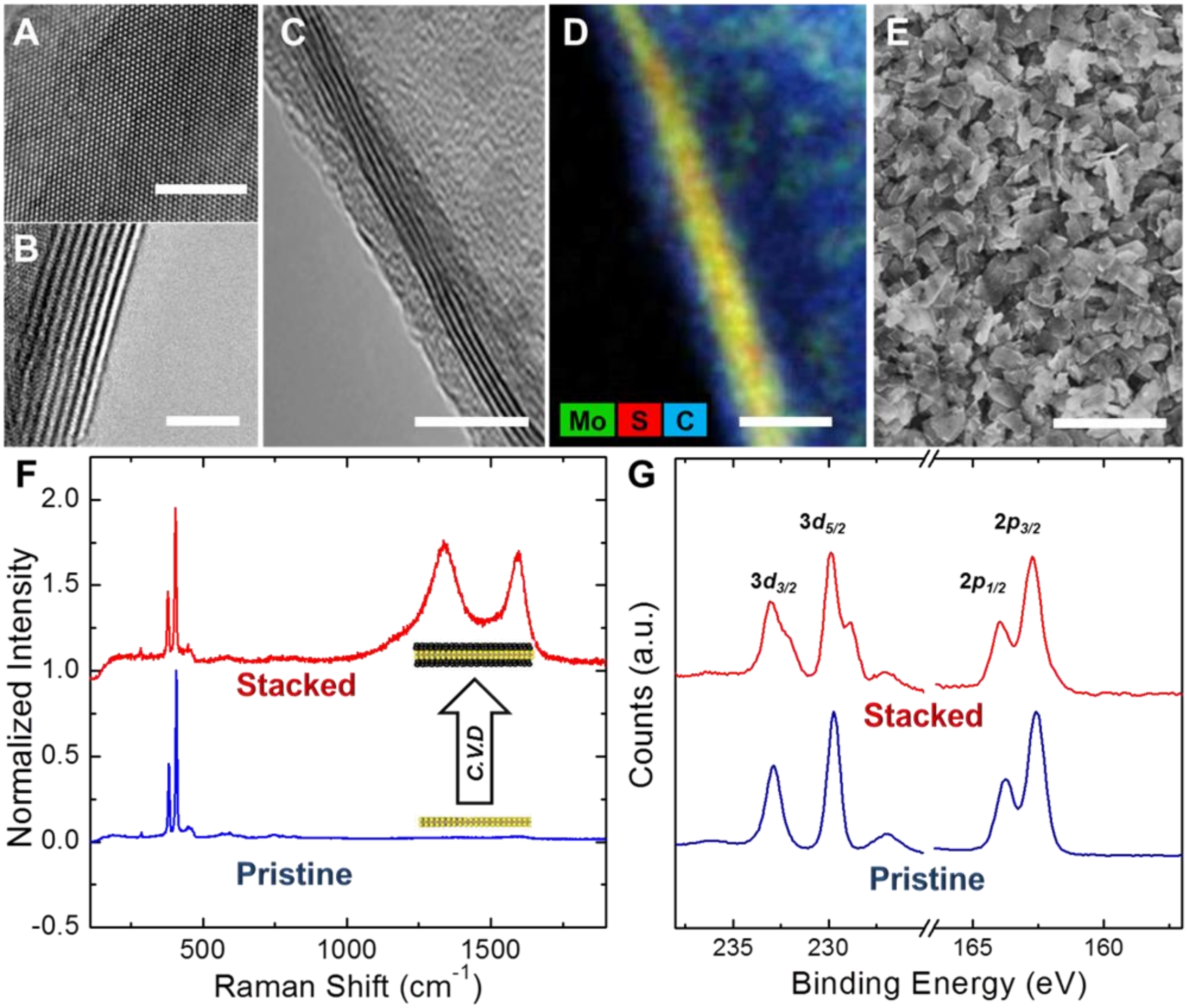

Figure 5.2. (a-b). TEM images of pristine exfoliated MoS_2 nanosheets. (c) Edge-view TEM image of a vertically stacked C-MoS_2 nanosheet. (d) EDS elemental analysis of a stacked C-MoS_2 nanosheet. (e) SEM image of an electrophoretically assembled electrode material formed with stacked C-MoS_2 nanosheets.

MoS_2 nanosheets were produced through liquid exfoliation of bulk MoS_2 powders in n-methyl-2-pyrrolidone (NMP) solvents and subsequent centrifugation. Transmission electron microscopy (TEM) of a representative exfoliated MoS_2 nanosheet is shown in Figure 5.2a,b**.**

Interlayer spacing of ~ 0.61 nm is observed for MoS_2 nanosheets, with thicknesses ranging from 2-10 atomic layers. Ultrathin carbon layers are grown directly on the MoS_2 surface through MoS_2 catalyzed decomposition of C_2H_2 precursors using a temperature ramp chemical vapor deposition (CVD) process. This generates vertically stacked architectures where ultrathin carbon layers are formed on both sides of the MoS_2 nanosheets, with a representative TEM image of this architecture shown in Figure 5.2c, and corresponding elemental analysis map in Figure 5.2d. To produce an appreciable mass of material for electrochemical tests, EPD was used to assemble the vertically stacked C-MoS_2 nanosheets into conformal films on metal substrates from NMP dispersions following CVD. Raman spectroscopy analysis in Figure 5.2f of vertically stacked C-MoS_2 nanosheets indicates that vertical stacks maintain an identical signature of crystalline MoS_2 following the carbon synthesis based on E_{2G} and A_{1G} modes (300 – 500 cm^{-1}). The carbon layers exhibit a significant amount of sp^3 hybridized carbon atoms (~ 1320 cm^{-1}, or D-band) relative to sp^2 carbon species (~ 1580 cm^{-1}, or G-band). Whereas this indicates the presence of carbon, x-ray photoelectron spectroscopy (XPS) indicates the emergence of both a peak in the sulfur $2p_{3/2}$ spectra at low binding energies as well as shoulders in both Mo $3d_{5/2}$ and $3d_{3/2}$ peaks that represent the formation of Mo-C bonds and distortion of surface S atoms. Figure 5.2g. This analysis collectively supports the formation of a distinct carbon-MoS_2 stacked interface, where mismatch of the in-plane lattice spacing between MoS_2 and carbon will induce significant interface strain.

To assess strain in the vertically stacked 2D material, statistical Raman spectroscopy mapping comprising over 200 individual scans in separate areas was performed on the E_{2G} and A_{1G} modes of MoS_2, which are highly sensitive to tensile or compressive strain.[79-81] (Figure 5.3a,b) Based on the peak-to-peak analysis of Raman mode distributions, blue-shifts of ~ 0.66

cm^{-1} and ~0.59cm^{-1} were observed for the E_{2G} and A_{1G} modes, respectively. Asymmetry in these modes is expected and attributed to stronger electronic coupling to the A_{1G} mode[82] and weak covalent bonds that form between the MoS_2 and carbon species. This yields a ~ 0.1-0.2% compressive strain based upon relative A_{1G} mode shifts in accordance with previous studies[68, 80], supporting the presence of interface-induced compressive strain on the MoS_2 material. This is further confirmed using x-ray diffraction (XRD) which demonstrates a similar ~ 0.1% compressive strain due to vertical stacking based on analysis of the (100) and (110) low-index planes of MoS_2. (Figure 5.3c)

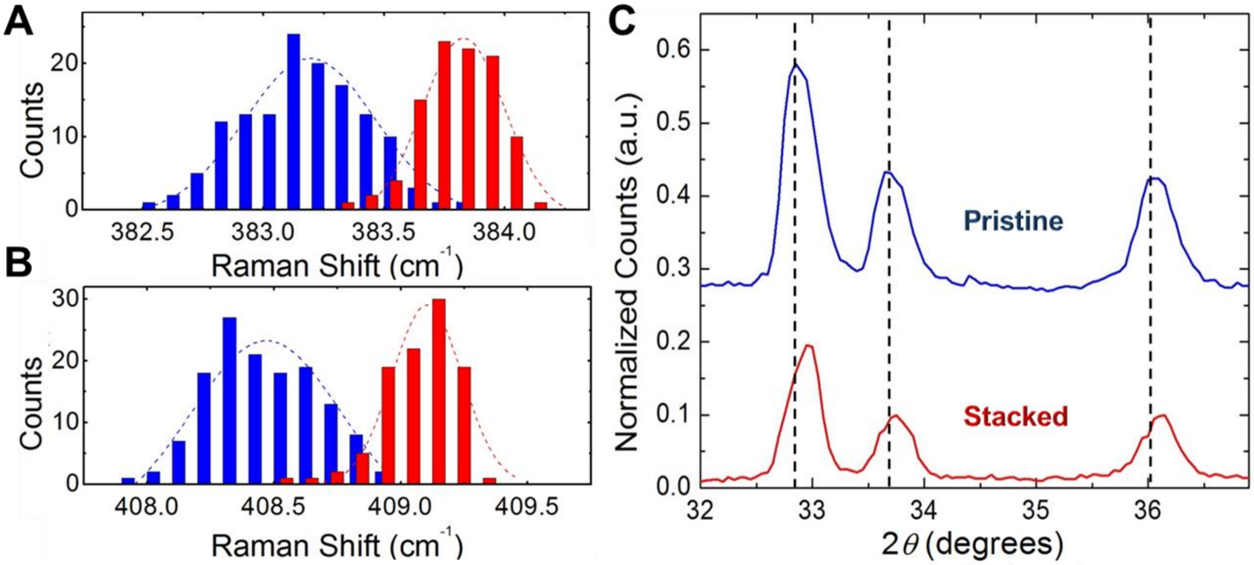

Figure 5.3. (a,b) Distributions from Raman spectroscopy maps comprising > 100 individual scans showing average shifts in the MoS_2 A_{1G} and E_{2G} modes due to strain induced by a lattice mismatched carbon-MoS_2 interface. (c) XRD analysis of vertically stacked C-MoS_2 nanosheets indicating stacking-induced strain in low index planes. The following planes can be assigned to the XRD spectra: 2θ = ~ 32.6° is (100), 2θ = ~ 33.5° is (101), and 2θ = ~ 35.8° is (102).

To assess how the vertically stacked architecture and interface strain influences electrochemical processes, we combined electrophoretically assembled vertically stacked 2D C-MoS_2 nanosheets with Li metal electrodes and an EC/DEC/$LiPF_6$ electrolyte and compared electrochemical properties against similar electrode materials produced with pristine MoS_2

nanosheets. In contrast to the electrochemical reaction pathway outlined in the schematic of Figure 5.1c, insertion of lithium into the vertically stacked C-MoS_2 nanosheets yields a chemical reaction evident at ~ 2.3 V vs. Li/Li^+ based on dQ/dE curves of the initial discharge reaction (Figure 5.4a,b) which is close to the open-circuit voltage (OCV) of the device. Furthermore, there is no significant signature of lithium insertion at lower voltages in a manner consistent with pristine MoS_2 nanosheet electrodes. This highlights the presence of a chemical storage process occurring in vertically stacked C-MoS_2 materials that is not observed in pristine MoS_2 materials. A schematic outline of the proposed reaction pathway is presented in Figure 5.4c. Due to the lack of an electrochemical signature of lithium intercalation into the ultrathin carbon coating, this difference can be associated solely with interface compressive strain in the 2D stacked C-MoS_2 nanosheets versus the pristine nanosheets.

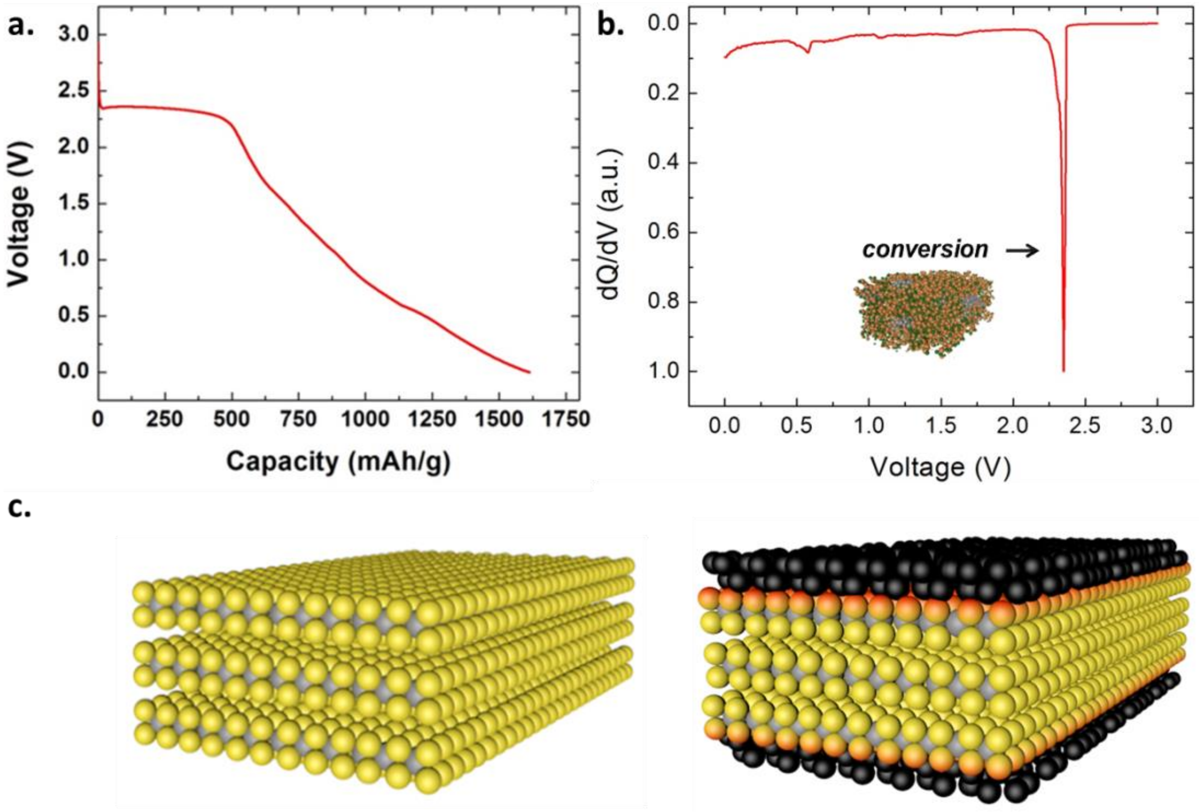

Figure 5.4. (a) Initial discharge curve for a carbon-coated MoS_2 NS and corresponding DQ/DE plot in (b) highlighting the reactions present in the discharge curve. (c) schematic illustration of the carbon coated MoS_2 conversion reaction process.

To address the effect of the C-MoS_2 interface on the electrochemical properties during lithium insertion, Raman spectroscopy of the electrophoretically assembled MoS_2-based electrodes at different cathodic potentials was carried out (Figure 5.5). This analysis is possible due to the preparation of electrodes in a manner that does not require binder materials often used in conventional battery electrodes that can overwhelm the desired Raman spectroscopic features. At OCV conditions, both electrode materials exhibit only the native Raman modes of MoS_2. Cathodic scans from OCV conditions to 1.75 V vs. Li/Li^+ - an energy below the Li^+ insertion reaction observed for vertically stacked C-MoS_2 nanosheets, yields no change for the pristine MoS_2 nanosheets, but the emergence of a distinct Raman peak at 746 cm^{-1} for C-MoS2 nanosheets. This mode is due to the formation of lithium polysulfides (Li_2S_n for $4 \leq n \leq 8$) that can be attributed to chemical conversion of the MoS_2 into reaction products in a manner consistent with eq. (2).[83] This confirms that the high voltage ~ 2.3 V signature in the dQ/dE curves for vertically stacked C-MoS_2 nanosheets is a chemical conversion process similar to that which is known to occur at low voltages (0.55 V) in pristine MoS_2. To further support this, cathodic scans were continued down to 0.01 V vs. Li/Li^+ for the pristine MoS_2 electrode, where the signature of conversion is evident due to the presence of the Raman mode at 746 cm^{-1}.

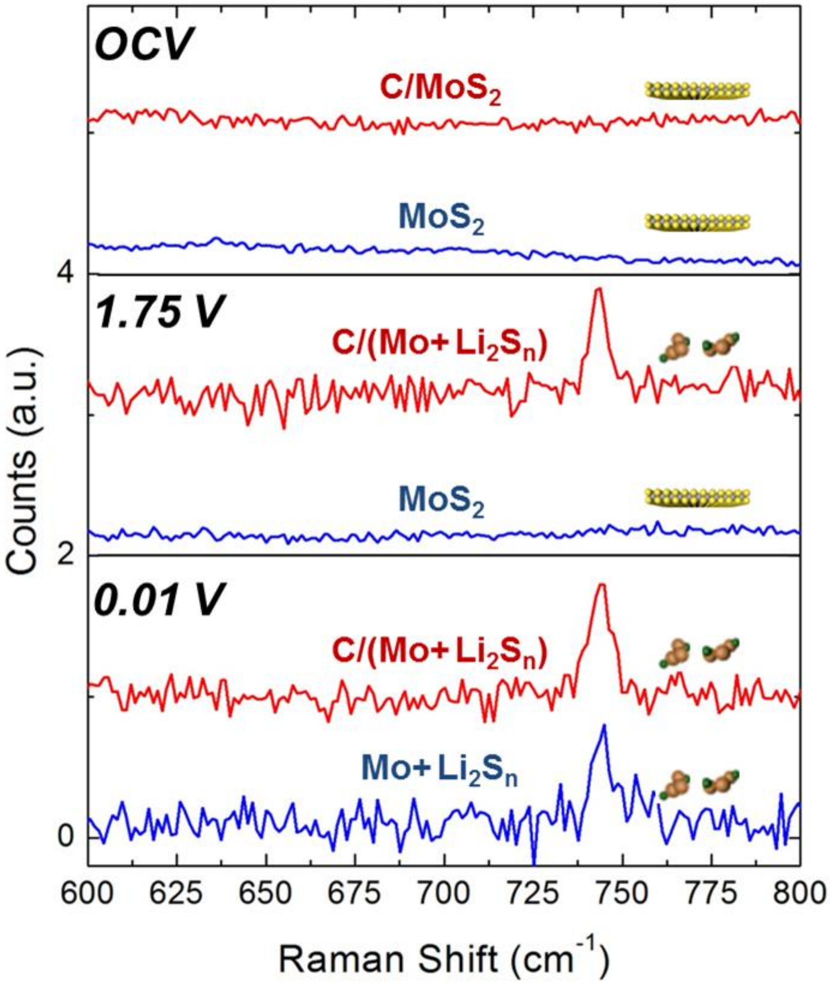

Figure 5.5. Raman spectroscopy confirming the electrochemical signature of chemical conversion based on the Raman mode of polysulfides at ~ 740 cm^{-1}. Notably, at 1.75 V vs. Li/Li+, the vertically stacked C-MoS_2 nanosheets have undergone chemical conversion whereas the pristine MoS_2 nanosheets remain unconverted.

5.5 Conclusion

Based upon combined spectroscopic and electrochemical analysis, a picture emerges emphasizing the role of interface strain on lithium insertion in vertically stacked C-MoS_2 materials. In the pristine semiconducting 2H phase of MoS_2, conversion of MoS_2 nanosheets cannot occur at voltages above where intercalation occurs (1.1 V vs. Li/Li^+) and can only proceed in a two-step chemical process following an intercalation reaction. As many researchers have discussed the promise of MoS_2 nanosheets for battery cathodes, the requirement of a conversion reaction that is near the reduction potential of lithium is highly impractical full-cell architectures. In a vertically stacked C-MoS_2 nanosheet, the interface strain due to lattice mismatch in a carbon-MoS_2 solid-solid interface leads to an average ~0.1% compressive strain that propagates into the MoS_2 nanosheet lattice and enables control of the energetics of chemical conversion. In this regard, interface strain provides the appropriate energetic landscape to sustain direct conversion at voltages that enable pairing with conventional anode material such as silicon or graphite which give promise to practical incorporation of this device in full cell battery.

CHAPTER 6

Precision Assembly of an All-Carbon 3-D Current Collector

6.1 Introduction

While the previous chapters have demonstrated the utility of EPD to fabricate cost-effective full-cell electrodes for lithium-ion batteries, the remainder of this dissertation will focus on the use of this technique to fabricate the battery architectures that are likely to replace Li-ion technologies in the coming decade. For these battery systems, the ability to assemble pristine, high-surface area structures of carbon nanomaterials is crucial in order to fully realize the potential of Li-S and Li-O batteries. In this regard, graphene foam materials have emerged as a promising candidate with which to construct high-surface area, 3-D, conductive templates. Unfortunately, however, to achieve structural stability of macroscale assemblies of these carbon structures, it is common to interface these nanomaterials with polymer stabilizers to retain structural stability during the processing of free-standing carbon structures. In this chapter, the drawbacks associated with this method of stabilization are presented and a means to overcome these limitations is presented through EPD. By stabilizing graphene structures with a layer of SWCNTs, the structural integrity of 3-D graphene films is preserved while simultaneously preserving the native material’s conductivity and chemical inertness.

The two-dimensional, atomically-thin configuration of graphene has enabled the understanding of new physics and chemistry in two-dimensional materials which has been the foundation for the emergence of a broad range of graphene-based applications in areas such as catalysis, sensing, energy systems, and electronics.[84, 85] Ideal material performance intrinsic to suspended graphene, such as high mobility and excellent electrical and thermal properties, are compromised when the graphene is interfaced with a substrate or a polymer surface.[86] Three-dimensional, freestanding structures of graphene,[18] where graphene is grown on the interior surface of a three-dimensional metal template, give exemplary promise to the route of forming flexible and robust macroscopic templates of graphene. However, such an approach is only viable for applications if routes to stabilize freestanding graphene materials can be executed without generating residue or impurities that degrade the electrical, gravimetric, thermal, and electrochemical properties. This is a challenge for graphene materials since studies of flat, 2-D graphene have elucidated the irreversible presence of residue when utilizing the polymethylmethacralate (PMMA) based transfer process universally employed for nearly all graphene-based studies. The presence of such residues and their adverse effect have been demonstrated to persist through chemical and annealing treatments, leading to a modification of the graphene electronic structure that is manifested in optical blue-shifting of the G' double resonance mode in Raman spectroscopy studies.[87, 88] For three-dimensional graphene materials, these results emphasize that the absence of PMMA residue not only impacts the electronic properties, but is also the basis of the structural integrity for the freestanding 3-D material.

One possible route towards polymer-free stabilization is the use of EPD to conformally coat these 3-D graphene structures with structurally stable, chemically inert materials. EPD combines the scalability necessary for roll-to-roll or large-scale industrial processing with control over thickness and deposition rate based on the voltage, charge-to-mass ratio of the particles, and deposition time.[89] In this chapter, a route to stabilize 3-D templates of graphene materials using EPD to generate a thin layer of surfactant-free SWCNTs on the surface of the graphene is presented. It is found that, in comparison to PMMA stabilization, this leads to a graphene material that exhibits nearly 50x lower electrical resistance and optical Raman spectroscopic signatures of pristine graphenic carbon. Whereas this provides a functional route toward stabilizing 3-D graphene materials, it is demonstrated that this approach also leads to near-ideal properties for graphene-based applications.

6.2 Materials and Methods

The CVD graphene films used in this study are grown on Ni foams (MTI, ~110 ppi) in a quartz tube furnace at a growth temperature of 1000^o C under ambient pressure and in an atmosphere of 100 sccm H_2, 500 sccm of Ar, and 10 sccm CH_4. For PMMA assisted graphene foams, 5.5wt% PMMA in Ethyl Lactate is drop casted onto the foam and baked in air on a hot plate at 90^o C for 1 hour before being placed into an iron (III) chloride bath overnight for removal of the Ni foam substrate. The resulting PMMA/graphene foam is placed into a bath of DI water for ~12 hrs and then left to dry. Removal of the PMMA is achieved by placing the PMMA/graphene foam samples into an acetone bath at 25^o C for ~ 1 hr. Fabrication of the annealed samples is achieved using an identical method followed by an additional annealing procedure in which the polymer supported GF is placed into a tube furnace and annealed for 1h under ambient conditions at 400^{o}C followed by an additional hour of annealing in a flow of mixed H_2 (200sccm) and Ar (400sccm).

The EPD solution of SWCNTs is prepared as follows: 10 mg of SWCNTs (HiPCO, purified) are dissolved in 20 ml of NMP and sonicated for ~ 1hr. Graphene coated Ni foams are suspended in the resulting solution at a 0.5 cm electrode separation with a 1cm x 1cm stainless steel counter electrode and subjected to an applied potential of 120 V for 20 min. The resulting nanostructure is placed in an iron(III) chloride bath overnight and then placed into a bath of DI water before being scooped onto the stainless steel current collector.

6.3 Imparting Mechanical Stability

Although 3-D graphene materials have been extensively utilized for applications in the past few years, these approaches have required the use of PMMA-stabilized materials. This study found that 3-D structures of graphene do not exhibit mechanical integrity without the use of PMMA, except when grown with very thick graphite-like layers of graphene materials, upon dissolution of the 3-D foam substrate supporting the graphene. This is illustrated in Figure 6.1a-b, where the 3-D graphene is found to break into small flakes of graphene material when reaching full metal-support dissolution. Structural stabilization of 3-D graphene is achieved with PMMA after dissolving the polymer using acetone, but close SEM analysis reveals the presence of PMMA globules in crevices of the graphene material that cannot be removed using chemical treatments. However, as discussed at a later point, the use of PMMA plays a role to inhibit the development of applications that require pristine graphene properties. Therefore, by using EPD to coat a thin conformal layer of pristine SWCNTs on the graphene surface, a hybrid material is achieved in which SWCNTs act to electrically and mechanically bridge the adjacent grain-like flakes of graphene formed during growth on an underlying Ni foam template using standard chemical vapor deposition processing. This enables the formation of freestanding 3-D foams of graphene materials with superior properties to those materials stabilized using PMMA (Figure 6.1c-d). The benefit of this SWCNT stabilization route is further illustrated in Figure 6.1e-h, where the web-like morphology of the SWCNTs forms an electrically conductive and mechanically robust stabilization layer to support the 3-D graphene in contrast to the insulating residual polymer stabilizing graphene sheets when using PMMA stabilization.

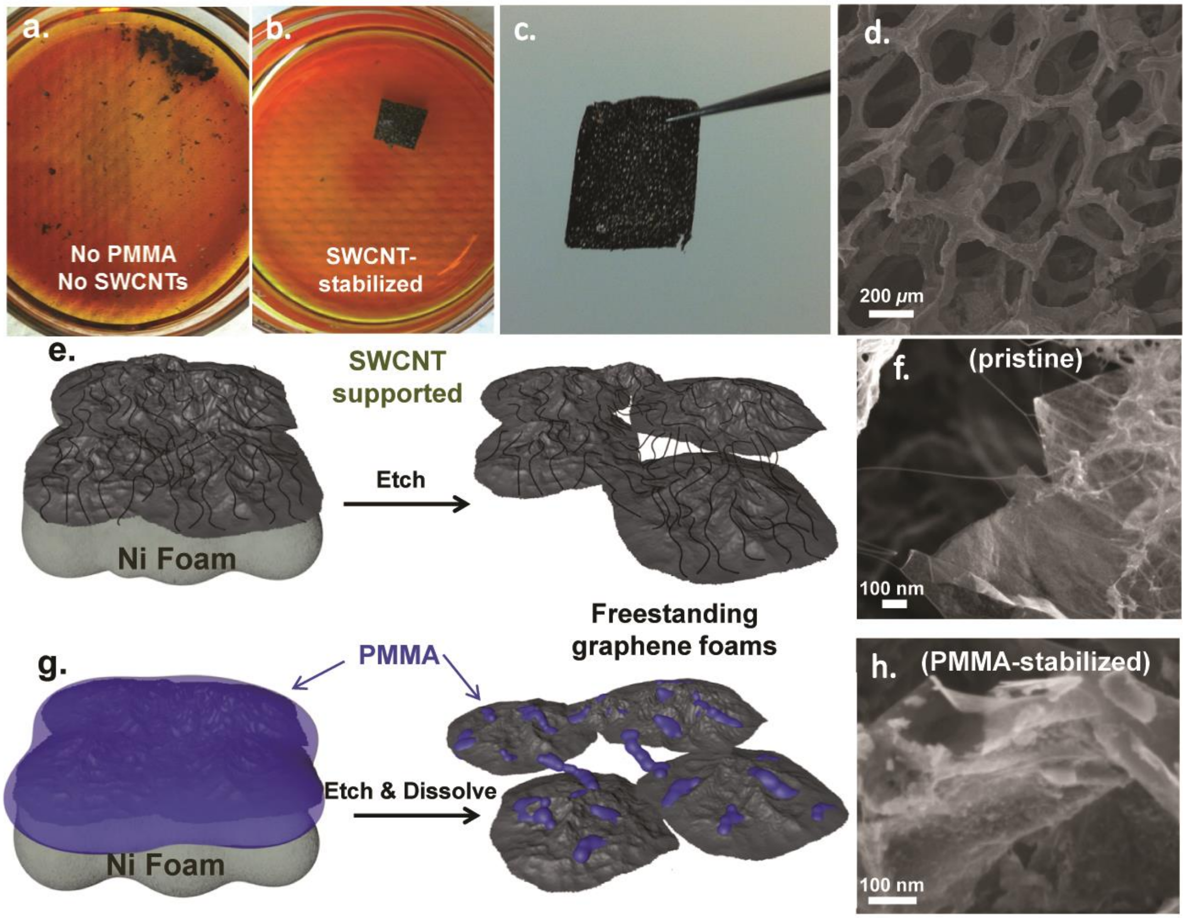

Figure 6.1. (a-b) Photographs of graphene foams that remain following the dissolution of Ni foam in $FeCl_3$. The left panel is a graphene foam with no polymer or SWCNT stabilization, whereas the right side panel shows a foam material stabilized with surfactant-free SWCNTs. (c) Photograph of a freestanding graphene-SWCNT foam. (d) Low-magnification of a SWCNT-stabilized graphene foam material. (e-h) Scheme depicting the mechanism of stabilization of 3-D graphene foams with SWCNTs (e) and PMMA polymer (g) that leaves residue behind following etching of the Ni foam, with supporting SEM images (f,h).

6.4 Device Performance

In order to characterize the benefit of the SWCNT coating, in comparison to PMMA stabilization, the electrical, optical, and electrochemical properties of the foam materials was investigated (Figure 6.2). To characterize the electrical properties, two-electrode current-voltage scans were performed on both SWCNT stabilized and PMMA stabilized graphene. Since the thickness of the foam materials in both cases are identical and both samples exhibited a linear, Ohmic response, the resistivity of PMMA stabilized foam was calculated to be 1.8 x 10^{-4} Ω*m, and the resistivity of the CNT stabilized sample to be 3.5 x 10^{-6} Ω*m (Figure 6.2a). This indicates a ~ 50x improvement in sample resistivity and a value approaching bulk metals when using CNT stabilization. Furthermore, optical analysis of the G’ mode using Raman spectroscopy revealed further benefits of the SWCNT stabilized materials. The G’ mode corresponds to a double-resonance process that is highly dependent upon the Fermi velocity in the vicinity of the excited carbon-carbon bond.[90] In the case of PMMA stabilized graphene, a blueshift of the peak center of the graphene G’ mode of ~ 19 cm^{-1} compared to the SWCNT stabilized foams is observed, emphasizing the pristine nature of the graphene when stabilizing it with SWCNTs relative to PMMA (Figure 6.2b).[87] It has been shown that polymer residue, even after annealing, can influence the electronic structure of the graphene and cause this peak to blue-shift relative to pristine graphene materials.

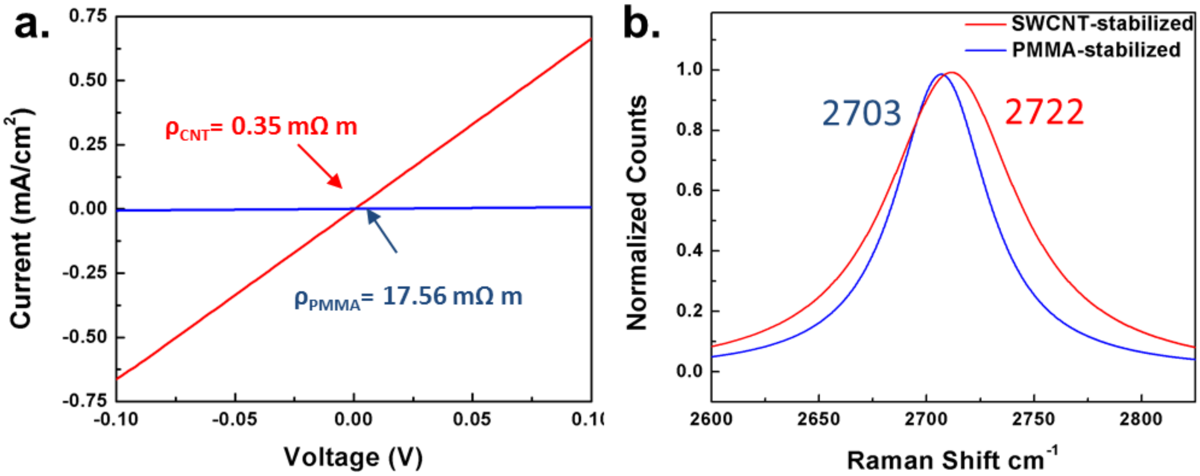

Figure 6.2 (a) Electrical I-V measurements made on PMMA-stabilized and SWCNT-stabilized foams, (b) Analysis of the Raman spectroscopic G’ mode for PMMA and SWCNT stabilized foams.

To gauge the benefits of these hybrid materials in an electrochemical setting, such as those occurring in Li-S or Li-O batteries, an electrochemical analysis of the PMMA-stabilized and SWCNT-stabilized materials using 1-ethyl-3-methylimidizolium tetraflouroborate (EMIBF4) electrolytes was carried out. Electrochemical impedance spectroscopy (EIS) measurements (Figure 6.2b) indicate ideal diffusion behavior for the SWCNT-stabilized graphene foams evidenced by a mid-frequency spike of ~ 45^o compared to non-ideal diffusion properties for the PMMA-graphene foam. Additionally, cyclic voltammetry studies performed at 100 mV/second scan rates (Figure 6.3c) indicate an improved electrochemical stability window for the SWCNT stabilized foam material (~ 0.5 – 0.7 V).

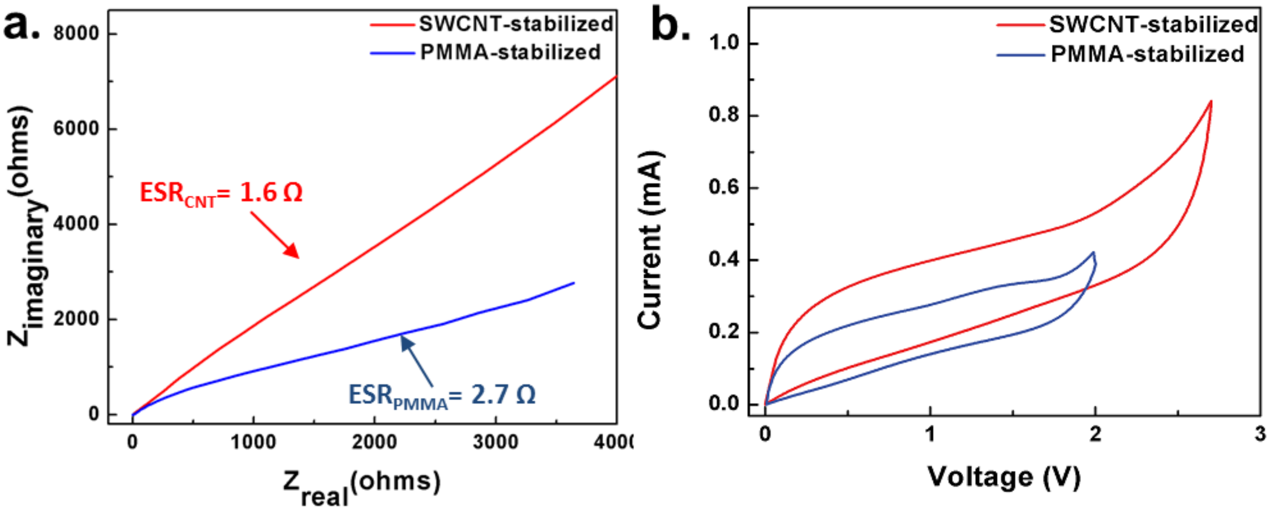

Figure 6.3. (a) EIS analysis of PMMA and SWCNT stabilized foams in EMIBF4 electrolytes, and (b) CV scans performed at a rate of 0.1 mV-s for each foam material.

6.5 Conclusion

Therefore, as the potential for future applications employing 3-D graphene materials is correlated to the ability to generate pristine, freestanding graphene materials, an approach is demonstrated here to achieve this by stabilizing the surface of graphene foam structures with a thin, clean SWCNT coatings using a scalable EPD technique. This hybrid material yields a pristine, electrically conductive and mechanically robust template that can be the basis for a broad range of efficient device applications across fields such as energy storage and conversion, catalysis, sensing, and other fields where pristine properties of carbon nanostructures are desired. This approach more broadly illustrates a route to engineer pristine carbon nanomaterials to generate macroscopic assemblies exhibiting significantly enhanced performance in comparison to materials with residual parasitic mass from polymers or surfactants.

CHAPTER 7

EPD of Electrocatalysts for Li-Air Batteries

7.1 Introduction

For many emerging energy storage applications, the practical realization of long-range electric vehicles and low-cost grid-scale storage systems rests in the ability to cost-effectively design secondary high energy density storage media that can be competitive on a cost-performance basis with fossil fuel-powered systems. In this regard, non-aqueous lithium-oxygen batteries (LOB) have promise as a solution owing to the extremely high theoretical energy density on par with conventional fossil fuels.[42, 91-93] Unlike traditional metal-ion batteries, metal-air batteries rely on the ability to store ions on the surface of a material through a reaction with ambient air and the performance of these materials is directly related to the reactivity of a material's surface for oxygen evolution (OER) and reduction (ORR) reactions.[94] The high surface area and improved reactivity of nanostructured materials gives rise to substantially improved performance in metal-air architectures comprised of pristine nanomaterials.[95] Traditional manufacturing techniques are unable to produce such structures for metal-air batteries due to the complex 3-D surfaces required for acceptable volumetric and gravimetric capacities. Conventional coating technologies rely on 2-D methods to maintain low-cost and high-throughput and the additives required by these techniques have been shown to passivate a material's surface and severely inhibit, or in some cases completely prevent, the ability to nucleate oxide compounds. Thus, processing of pristine solutions of nanomaterials on 3-D architectures is essential to obtaining the level of performance predicted for air battery electrodes.

Macroscale assemblies of catalyst nanomaterials are essential for the commercial realization of next generation energy storage and conversion systems.[96-98] This is especially true for Li-O batteries in which the mechanism of charge storage relies on a complex reaction between lithium and oxygen that yields the largest theoretical energy density of any energy storage system to date. This high theoretical capacity is based on the cathode-side reaction which generates lithium peroxide on the electrode surface as the battery discharges: $2Li^+ + O_2 \rightarrow Li_2O_2$, $E^0 = 2.96$ V vs Li/Li^+. Although the chemical mechanism of the Li-O seems straightforward, the practical operation of these devices has been impeded by seemingly endless technical challenges such as low round-trip efficiency, poor cyclability, and limited stability of the battery components.[99-102] These challenges primarily arise from the energetics of growth and decomposition of the insulating and insoluble discharge product during operation which yields a variety of parasitic side reaction products and degrades the battery components. Two routes to overcome many of these challenges have emerged recently, including the use of either redox mediators or catalysts that can direct the efficient formation of discharge products. Recent rapid progress has demonstrated the use of a LiI redox mediator to instigate the formation of LiOH rather than Li_2O_2, even though charge and energy efficiencies of these devices still lag behind those of conventional Li-ion batteries (>99.5%).[103-105] In this manner, catalysts can play a key role either independently used in Li-O batteries or also combined with redox mediators to lower the overpotential at the site of discharge product formation.[94, 106, 107]

To this end, a number of catalyst architectures have shown great promise for improving the efficiency of LOBs including precious metal catalysts,[108] doped nanocarbon architectures,[109] and metal oxide nanostructures.[110] Among these, metal oxide-based architectures have received a great deal of attention due to the low material cost and bi-functional capability in promoting both the oxygen evolution (OER) and oxygen reduction (ORR) reactions present in the Li-O battery chemistry.[111-113] Within this regime, catalysts minimize the overpotential associated with both the OER and ORR by tuning parameters such as electronic conductivity, binding strength of the adsorbate on the particle surface, and the nature of the discharge product morphology.[106, 114-116] Whereas traditional routes to achieve this enhanced performance have focused on optimization of the particle-scale chemical and electronic properties of the individual catalyst particles, efforts to understand how morphological effects and assembly on the scale of a macroscopic electrode can influence performance have not been carried out. Despite the recognized importance of assembly for catalytic systems in platforms ranging from fuel cells to gas sensors,[117-119] the effect of catalyst morphology in a Li-O battery and its impact on the performance of the catalyst layer currently remains largely unexplored.

A key challenge to study morphology effects on catalytic systems is the use of techniques that can enable simultaneous control over particle orientation, packing density, film thickness, and substrate adhesion, among other parameters. Unlike conventional processes such as dip-coating, self-assembly, or spin coating, electrophoretic deposition (EPD) has the potential to achieve this control by precise selection of the deposition parameters (*e.g.* applied voltage, duration, electrode geometry, *etc.*) that can be finely tuned.[120, 121] The assembly mechanism inherit to EPD maximizes interfacial contact between the substrate and depositing materials while also promoting high packing efficiencies within the assembled film itself yielding particle coatings that exhibit exceptional mechanical properties and resist delamination or aggregation.

Such interfacial limitations have been correlated to degradation in fuel cell applications[122] and hence we anticipate such effects to play a role in Li-O batteries.

In this study, we compare two methods of producing coatings of catalytic Mn_2O_3 nanoparticles on mesh substrates with different morphologies. For coatings prepared with EPD, which exhibit smooth, compact, and conformal morphologies, we demonstrate significant improvements to the operational parameters of Li-O batteries, including the overpotential and durability. Using *in-situ* electrochemical studies combined with *ex-situ* electrode imaging we demonstrate a synergistic effect between the single-particle catalytic properties and the morphological properties of the assembled catalyst layer to achieve the best performance in lithium-oxygen batteries.

7.2 Materials and Methods

Multi-walled carbon nanotube (MWCNT) coatings were fabricated on stainless steel mesh electrodes using a solution of MWCNT (cheaptubes.com, 8-15 nm diameter) in 1-methyl-2-pyrrolidone (NMP) (99.8%, Anhydrous). 20 mg of MWCNT material was added to 40 ml of NMP solution and sonicated for 30 minutes using a 3 second ‘on’ and 3 second ‘off’ pulse to minimize heating. A pristine stainless steel mesh electrode was then placed 0.5 cm from a stainless steel counter electrode on both the front and backside. A bias of 200 V was applied to the system using a Labview-operated Keithley 2400 Sourcemeter for 5 minutes and the mesh electrode as the anode before carefully removing the mesh from the solution and drying in a vacuum oven overnight. Only mesh materials with a MWCNT loading of 0.04 mg/cm^2 were selected for further use.

Coatings of catalyst particles (Mn_2O_3) were fabricating using a solution of Mn_2O_3 (skyspring nanomaterials, 40-60 nm) in ethanol (200 proof, Decon Laboratories). 20 mg of Mn_2O_3 was added to 40 ml of ethanol and the pH of the solution was tuned through dropwise addition of a 1 M NaOH solution until the suspension achieved a pH of 8. For EPD coatings, the MWCNT coated stainless steel mesh was placed back into the EPD system described in the previous section and a voltage of 100 V was applied for 1 minute before carefully removing the electrode from solution and leaving it to hang dry overnight. Only mesh cathodes with a Mn_2O_3 loading of 0.06 mg/cm^2 were selected for further testing. To form DC coatings, the MWCNT coated stainless steel mesh was briefly dipped in solution, removed, and left to dry before repeating the process to achieve s coverage density of 0.06 mg/cm^2.

Components for the Li-O battery were assembled into a custom built battery testing system using an argon-sealed glovebox with O_2 levels < 0.5 ppm (MBraun). The coated mesh cathode was placed opposite a lithium metal anode and a Celgard battery separator soaked in 0.1 M $LiClO_4$ tetraglyme (Sigma Aldrich) electrolyte was placed between them. The chamber was sealed and removed from the glovebox before evacuating the argon and refilling the chamber with a mixture of 20% O_2 / 80% Argon. Charge discharge, cyclic voltammetry and EIS measurements were performed using a Metrohm Autolab multichannel testing system over a frequency range of 1 MHz to 0.1Hz.

To obtain profileometry measurements, MWCNT coatings were applied to 2-D stainless steel surfaces using identical deposition parameters as those used to fabricate mesh structures. Mn_2O_3 films were then assembled on these 2-D stainless steel surfaces with the same procedure used to coat the stainless steel mesh. Profileometry was performed on the assembled composite films using a Veeco Dektak 150. Raman analysis was performed using a Renishaw inVia Raman microscope with a 532nm excitation. Zetasizer measurements were carried out using a Malvern Zetasizer Nano ZS instrument.

7.3 Solution Processing of Catalyst Materials

The integration of solution phase catalyst synthesis into scalable fabrication processes relies on the ability to control the final morphology of the assembled film. Whereas conventional coating methods such as dip-coating and doctor-blading are straight-forward, such methodologies that depend on the quality of the catalyst dispersion in the solution and the disruptive capillary forces present during drying present bottlenecks to achieve control necessary for many applications. Alternatively, electric-field assisted assembly, or electrophoretic deposition (EPD), can be used to control the morphology of coatings without sacrificing the ease and scalability of the coating technique. In this spirit, we focus this study on a comparison of films of catalyst nanoparticles (Mn_2O_3) produced using these two different coating techniques, and coated onto a multi-walled carbon nanotube (MWCNT) coated mesh electrode (Figure 7.1).

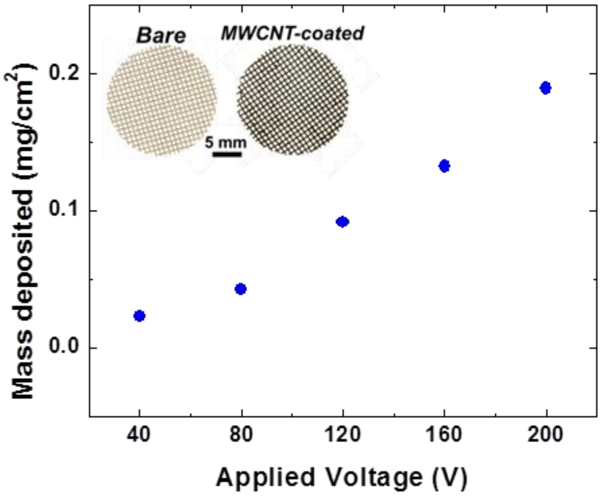

Figure 7.1. Mass deposition as a function of applied voltage for a 0.5 mg/ml solution of MWCNT in NMP demonstrating the linear relationship expected from the EPD process. The inset depicts an optical imaging of the stainless steel mesh electrode before and after deposition of the MWCNT coating emphasizing no change to the geometric area of the electrode as a result of deposition.

The general process for catalyst assembly in both cases is presented in Figure 7.2a and 7.2b for the dip-coat (DC) and EPD process, respectively. Commercially available Mn_2O_3 nanoparticles (NP) dispersed in ethanol (0.5 mg/ml) provide the depositing suspension for both processes. During DC assembly, the substrate is dipped in the Mn_2O_3 solution and carefully removed to produce the catalyst layer, which forms a disordered aggregate of particles during drying. Scanning electron microscopy (SEM) analysis of the DC sample in Figure 7.2c highlights this non-uniformity through the presence of uncoated regions and large aggregates that are formed as result of the assembly process.

In contrast to this, EPD produces particulate films through a guided self-assembly process in which particles are directed to the deposition substrate under the application of an applied electric field. Upon arrival at the substrate surface, electrohydrodynamic flows generated by ionic currents provide lateral migration of the particles that can result in controlled monolayer-by-monolayer assembly that results in exceptionally uniform films with high packing density.[123, 124] Using this method, we are able to produce a film of tightly-packed nanoparticles which possess superior interparticle adhesion that overcome the effects of drying and preserve the uniform and conformal nature of the catalyst film that exists in solution[125] leaving a smooth, compact catalyst film. (Figure 7.2d) To further quantify the differences in the initial macroscopic morphology of the electrodes assembled using these different methods, profilometry was carried out on both substrates. (Figure 7.2e and 7.2f) A root mean square roughness of ~7.7 µm was measured for DC samples versus ~1.1 µm for EPD films. The use of EPD and DC assembly in forming the catalyst layer enables a comparison between smooth/compact and rough/disordered catalyst films and the effect these separate morphologies have on the continuous operation of a Li-O battery.

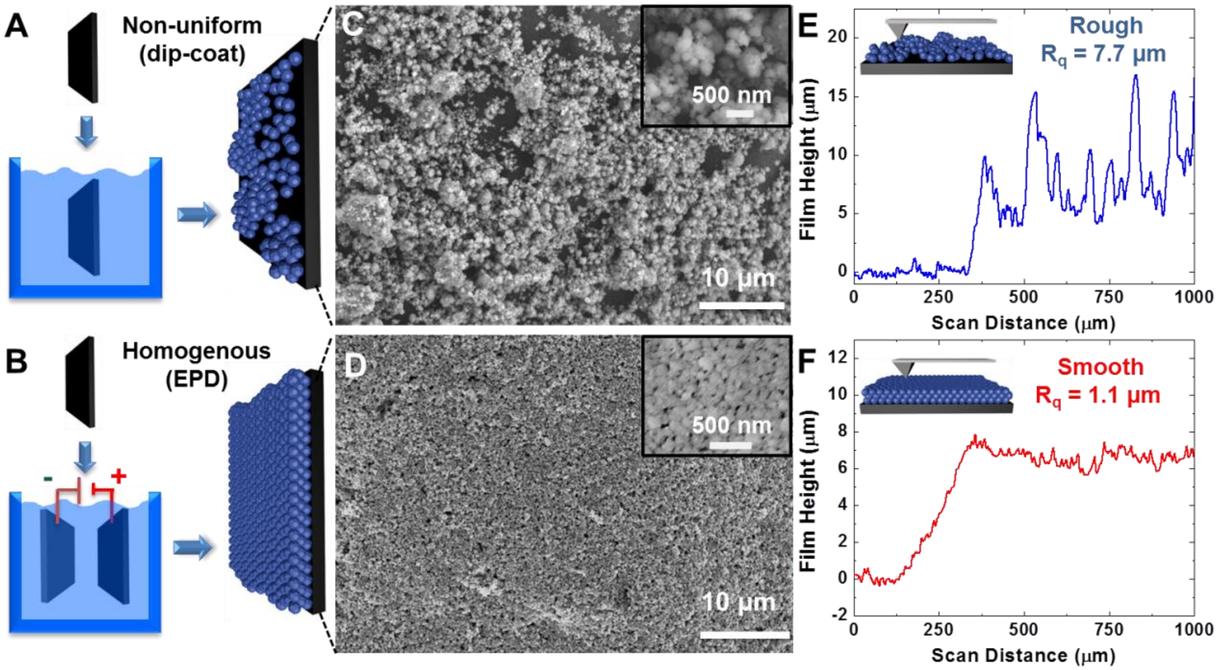

Figure 7.2. Schematic representation of (a) DC and (b) EPD assembly processes. During DC assembly, film formation via evaporation results in the presence of nanoparticle aggregates and large regions of exposed substrate in contrast to EPD which assembles particles through a guided self-assembly process using applied electric fields. (c-d) SEM imaging for both (c) DC and (d) EPD films with higher magnification insets showing the high packing density of the nanoparticles at the film interface. (e-f) Profilometry performed on (e) DC and (f) EPD films emphasizing the drastic difference in surface roughness as a result of the different assembly processes. An inset is included to illustrate the experimental configuration of profilometry measurements.

Smooth, well-interconnected Mn_2O_3 NP films from EPD were achieved by engineering the surface charge via the pH of the dispersing medium[126] which controls the zeta potential or the particle mobility under an applied electric field. Measurements of the Mn_2O_3 NP surface charge were performed over a range of acidity values (Figure 7.3a) and a suspension with a basic pH of 8.5 and a corresponding zeta potential value of -15.2 mV was selected as the depositing solution due to the high stability and electrophoretic mobility. High mobility enables the formation of films with exceptional packing efficiency and interparticle connectivity under applied electric fields.[127] Measurements of the total deposited Mn_2O_3 catalyst NP mass obtained using EPD was observed to increase in a nearly linear manner as a function of time (Figure 7.3b), which is in good agreement to a fit applied based on the widely-accepted Hamaker approximation (see supporting information). Therefore, the use of EPD provides the capability to rapidly assemble uniform films of catalyst NPs with highly controllable mass loading characteristics. Using this technique, catalytic Mn_2O_3 NPs were coated onto a 3D mesh electrode and a comparison of the coating quality with evaporative techniques with comparable mass loading is depicted in Figure 7.3c and 7.3d.

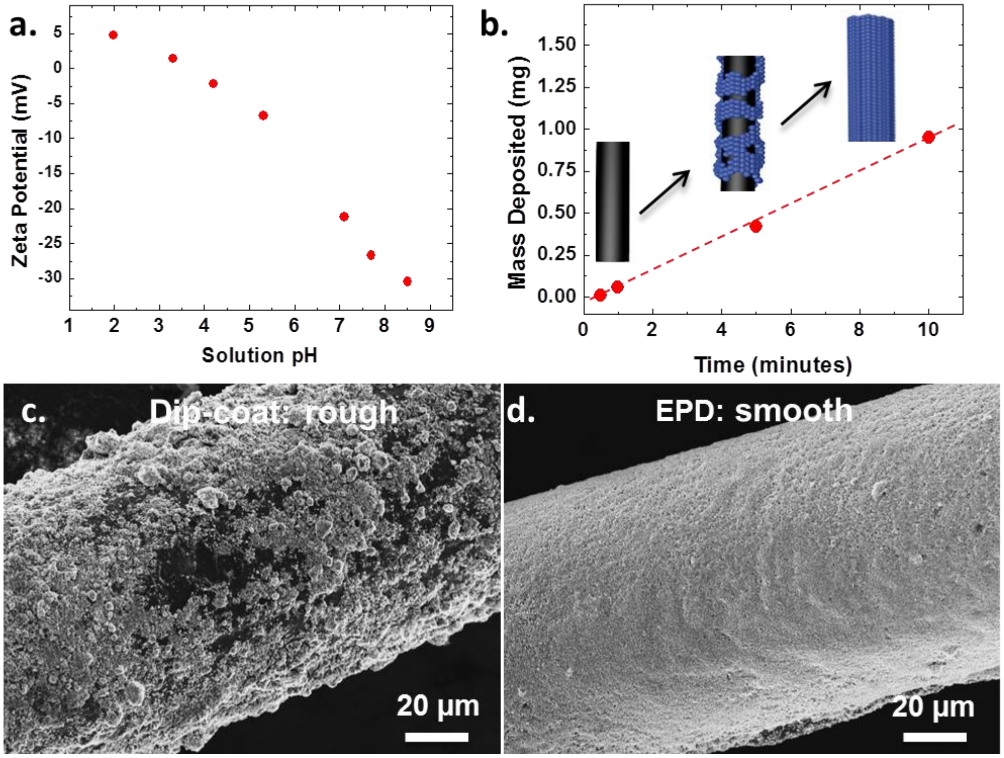

Figure 7.3. (a) Zeta potential measurements for a 0.5 mg/ml solution of Mn_2O_3 nanoparticles in ethanol. Magnitude of the zeta potential increase significantly for high pH values providing the necessary mobility and dispersion stability for the EPD process. (b) Mass deposited as a function of time during EPD assembly with schematic insets emphasizing the evolution of the coated layer. Dotted-line fit is based on modeling the system using the Hamaker approximation. (c-d) SEM characterization of the film coating on the mesh electrodes for (c) DC and (d) EPD assembly processes demonstrate the homogenous nature of EPD films over entire cylindrical regions of the mesh electrode.

7.4 Effects of Assembly on Li-air battery operation

We further employ these catalyst layers toward the reduction and evolution of oxygen species for lithium-oxygen batteries (LOBs), or also commonly denoted lithium-air batteries. During operation of a LOB, the growth and decomposition of an insulating discharge product occurs at the interface between the electrolyte and both the electrode surface and the catalyst layer, modifying interfacial electronic and physical properties between the catalyst particles and the current collector. To study this effect in the context of catalyst coatings, equivalent masses of MWCNTs were first coated onto a stainless steel (SS) mesh substrate using EPD[128] to produce a lightweight current collector before a subsequent coating of catalytic Mn_2O_3 nanoparticles was applied using either the DC or EPD technique.

To assess the performance of these catalyst-coated MWCNT mesh electrodes, galvanostatic charge-discharge measurements were performed to a constant capacity of 1,000 mAh/g_{carbon} at a rate of 100 mA/g_{carbon}, with the results of the first complete cycle shown in Figure 7.4a. Comparing the difference between ORR and OER curves in Figure 7.4a, smooth films exhibit a 1.37 V difference between the OER and ORR potentials while rough films exhibit a much larger separation of 1.59 V. This elucidates the overpotential improvement associated with an interconnected and smooth catalyst film as opposed to a film with a rough and disordered morphology. To further study the role of the morphology of the catalyst layer on the LOB performance, OER and ORR voltage profiles were compared over 5 consecutive cycles, and the end-of-cyclevoltage was compared to extract the voltage decay rate. (Figure 7.4b) A decay rate of 9.8 mV/cycle and 5.78 mV/cycle was observed during oxygen evolution for rough and smooth films, respectively, while a decay rate of 4.3 mV/cycle and 2.8 mV/cycle was observed during reduction.

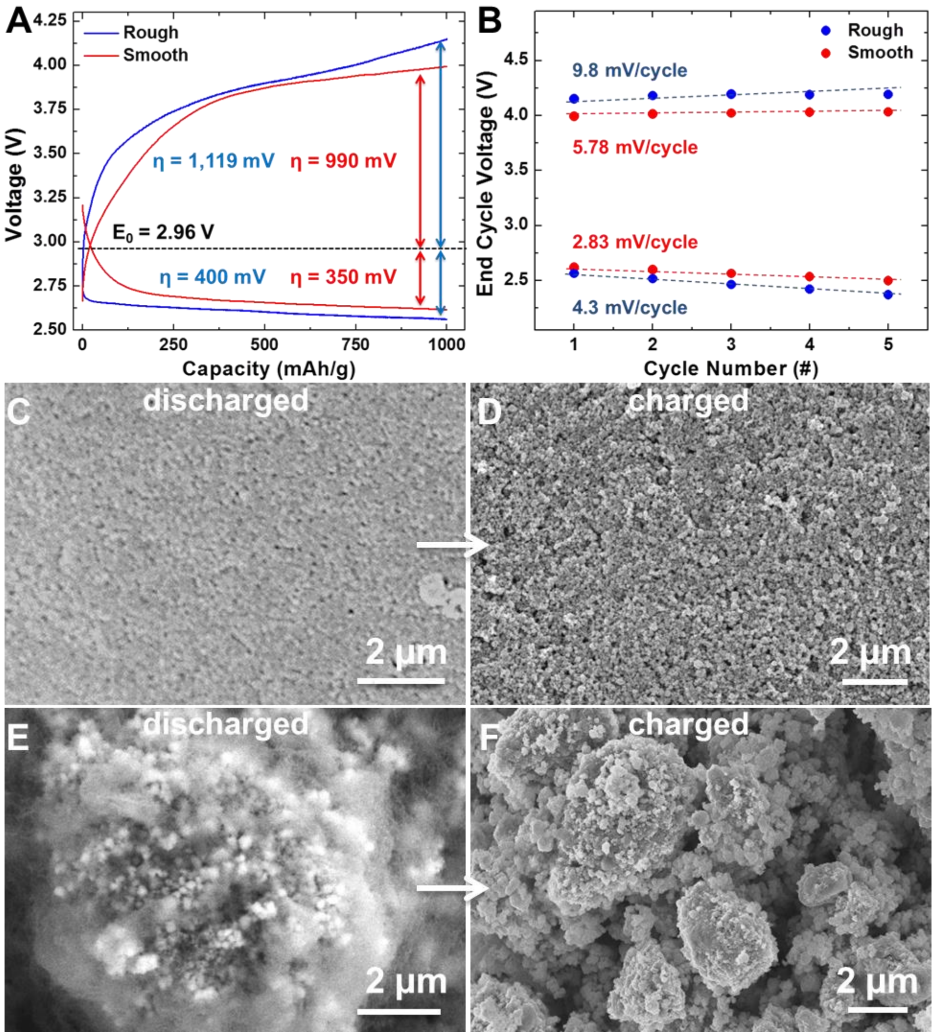

Figure 7.4. (a) Initial galvanostatic discharge and charge curves for smooth and rough catalyst films. (b) End-of-cycle voltage measurements from galvanostatic cycling over the course of 5 cycles. (c-f) SEM images of both smooth (c-d) and rough (e-f) catalyst layers both in the discharged state and charged state. Additional images for these films under further cycling are available in the supporting information.

To better understand the differences between the LOB performance of the DC and EPD catalyst coated electrodes, SEM was performed over the course of the initial discharge-charge cycles for both electrodes. (Figure 7.4c-f) After the initial discharge, SEM images reveal that rough films possess patchwork growth of discharge product on Mn_2O_3 aggregates (Figure 7.4e) while uniform films possess a conformal coverage distributed homogenously across the surface of the catalyst layer. (Figure 7.4c) Upon charging of the device, the smooth, compact Mn_2O_3

catalyst layer formed by EPD promotes uniform decomposition kinetics that restores the original morphology of the assembled electrode, whereas the patchy, heterogeneous interface from the DC coating results in preferential decomposition at more conductive regions of the electrode promoting disruptions to the interfacial region of the catalyst layer. This observation is further amplified after five consecutive cycles where the smooth compact EPD film maintains integrity, whereas the rough and disordered DC-assembled film exhibits an unstable interface that promotes the deactivation of large portions of catalyst material through detachment or electronic isolation *via* growth of a thick and insulating interface (Figure 7.5a and 7.5b). These results imply that catalyst layers with smooth morphology exhibit more uniform volumetric mechanical stresses during ORR product formation and removal, whereas coatings with greater roughness and more disorder lead to non-uniform stresses that more rapidly deactivate the function of the catalytic layer.

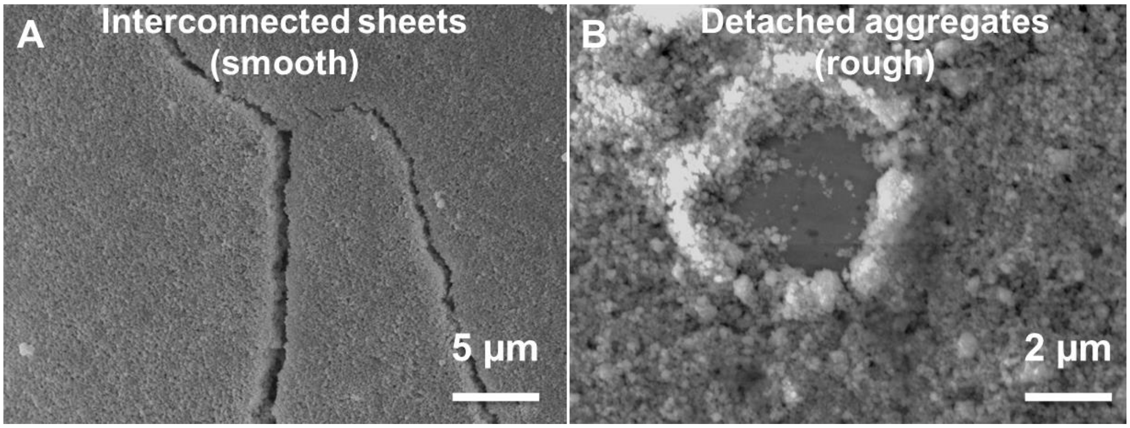

Figure 7.5. Oxygen electrodes after 5 cycles, (a) SEM of an EPD-assembled oxygen electrode demonstrating failure through the formation of cracks between large interconnected regions of the catalyst film and (b) SEM of a DC-assembled electrode showing failure through aggregation and detachment.

7.5 Mechanistic Understanding of The Enhancement to Li-air battery performance

To monitor the individual evolution of select electrode components during operation, electrochemical impedance spectroscopy (EIS) was performed at the end of each discharge during cyclic voltammetry testing over the course of 5 cycles. By probing the impedance of the electrode in the discharge state, we are able to accurately assess the impact of as-formed discharge products on the electronic processes within the active layer. *In-situ* EIS presents a powerful tool for measuring the evolution of metal oxide-based electrodes during LOB operation due to its non-invasive nature and its sensitivity in isolating contributions from individual cell components. EIS spectra for both rough and smooth catalyst films in lithium-oxygen batteries at OCV conditions are shown in Figure 7.6a, with an inset diagram showing the equivalent circuit representation used to analyze this data. The high frequency intercept of this plot with the real axis, indicated by circuit element R_{ESR}, represents the equivalent series resistance (ESR) which includes the ionic resistance from the electrolyte and the electrical resistance of the catalyst film and current collector.[129, 130] The small semicircle at high frequencies, indicated by circuit elements Q_{int} and R_{int}, represent the contribution to impedance from the active interface. The active interface in this case refers to the region of the electrode that consists of the portion of catalyst particles in direct contact with the electrolyte encompassing both the electrolyte resistance within the electrode and the resistance of the oxide particles comprising this interface.[131, 132] Lastly, the large semicircle at medium frequencies is represented by elements R_{ct} and Q_{ct} and includes within them the charge-transfer resistance stemming from kinetic inhibition to lithium ion transfer coupled with the double layer capacitance of the 3D electrode.[133, 134] These separate elements and their contribution to the overall cell impedance are represented schematically in Figure 7.6b.

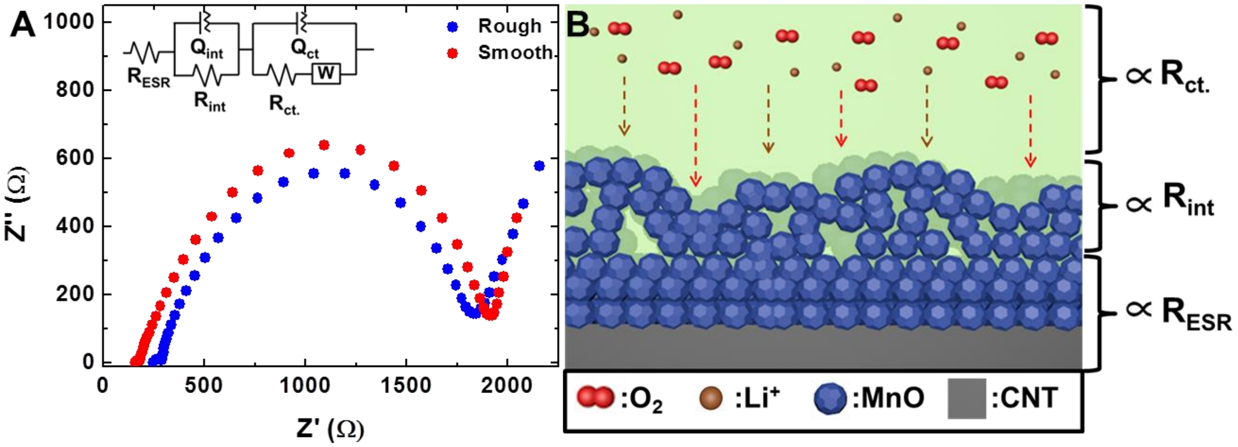

Figure 7.6. (a) EIS characterization of smooth and rough catalyst films in a LOB system at the open circuit voltage. Schematic illustration inset of the equivalent circuit used to describe cell components and fit EIS data (details on fits in the supporting information) (b) schematic illustration of the meaning of modeled circuit elements in the lithium-oxygen battery electrode, highlighting R_{ESR}, R_{int} and R_{ct}.

ESR values of 68.4 Ω/cm^2 for smooth electrodes and 100 Ω/cm^2 for rough electrodes indicate a nearly 1.5X improvement in EPD films that is attributed to the compact and interconnected nature of the Mn_2O_3 NPs in the EPD coated layer. Further, EIS data reveals a reduction in the interfacial resistance (R_{int}) of compact coatings with a value of 7.6 Ω/cm^2 for smooth films compared with 14.4 Ω/cm^2 in rough films that is related to better interconnectivity of the particles across the electrolyte-electrode interface in the EPD prepared film. Finally, a comparable charge-transfer resistance (R_{ct}) is observed for both smooth and rough electrodes with a resistance of ~680 Ω/cm^2 in smooth films compared with ~600 Ω/cm^2 in rough assemblies. The slightly increased resistance to charge transfer with the electrolyte solution in smooth films is attributed to a more complete and compact coating of the carbon surface by the conformal metal oxide layer. By monitoring the evolution of these individual cell components, substantial insight is provided regarding the underlying mechanisms of catalyst film degradation during battery operation.

A summary of the evolution of component resistance values (R_{int}, R_{ct}, R_{ESR}) over 5 consecutive charge-discharge cycles is presented in Figure 7.7. Most notably, the interfacial resistance in the LOB cathode exhibits the greatest susceptibility to the initial catalyst layer morphology with a 91.9% *increase* in interfacial resistance observed for rough films compared with a 15.9% *decrease* in smooth films. (Figure 7.7a) As this resistance is associated directly with the electrode-electrolyte interface, this implies that irreversible changes during volumetric expansion and contraction during ORR and OER processes leads to modifications to the catalyst-electrode interface that produces a large resistive barrier to charge transfer across this interface for the rough (DC) coating. However, the opposite is true for the EPD coatings, where this interface resistance slightly decreases. This observation is in excellent agreement with SEM images, including cross-sectional SEM images, that clearly highlight morphology-driven deactivation in rough catalyst coatings that would be correlated to such a large increase in R_{int}, and minimal structural modification to the smooth EPD coated catalyst layers. This morphology-directed modification to the internal resistance can be understood mechanistically based on results discussed thus far. Discharge into smooth catalyst films produces coverage of reaction product distributed uniformly across the entirety of the metal oxide surface and remains confined solely within the metal oxide layer. The incorporation of discharge product directly within the catalyst layer enables a portion of the catalyst particles at the electrolyte interface to become interconnected with conducting Li_2O_2 surfaces[135] resulting in a drop in film resistance. Upon charging, this configuration facilitates direct decomposition through catalytic pathways *via* metal oxide nanoparticles and produces little-to-no disruption of the catalyst-substrate interface after charging. However, in contrast to this, aggregates of catalyst particles in the non-uniform and rough coating results in an amorphous, heterogeneous interface with the electrolyte solution.

This architecture involves a number of different sites for the formation of reaction product including (1) exposed sites with no catalyst, where products form directly on the exposed collector material, (2) exposed catalyst sites with good electrical and mechanical connectivity with the collector interface, and (3) catalyst sites poorly mechanically and electrically connected to the collector. This architecture therefore leads to two distinct modes of degradation – parasitic side reaction products *via* decomposition of the carbon material, and morphological evolution and deactivation of the catalyst due to irregular volumetric changes that occur during the preferential formation of products at the most electrically accessible sites, typically at the interface with the collector. A schematic highlighting these degradation routes is presented in Figure 7.7d.

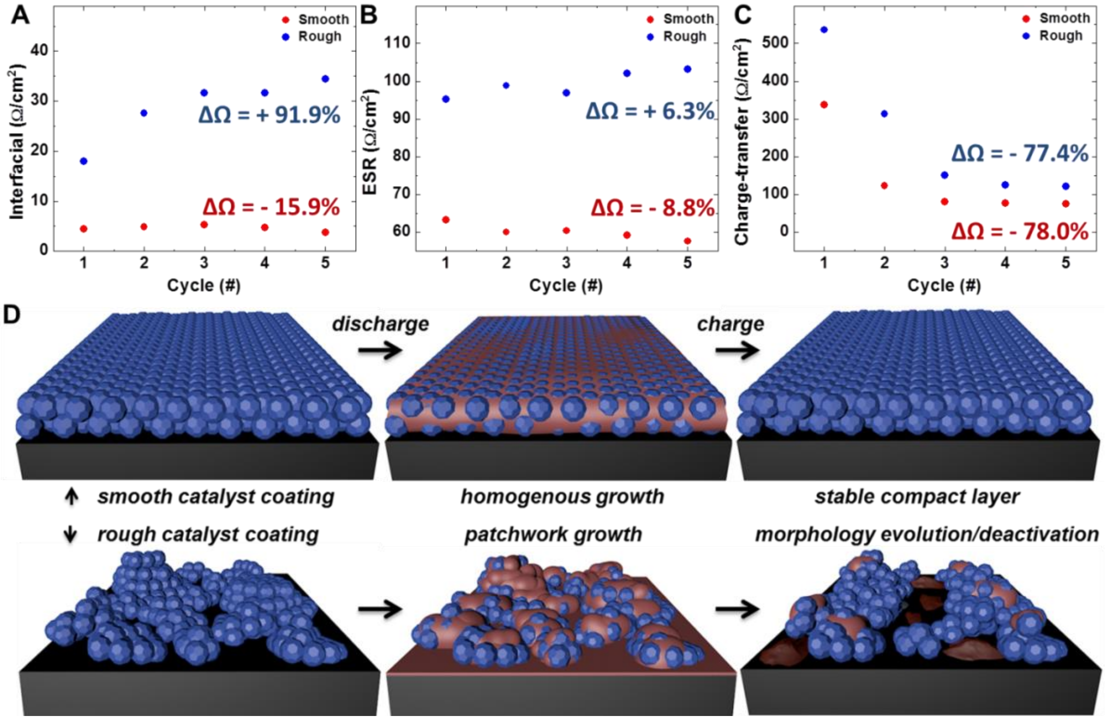

Figure 7.7. *In-situ* EIS analysis during charging and discharging of lithium-oxygen batteries. (a) interfacial (R_{int}) (b) ESR (R_{ESR}) and (c) charge-transfer (R_{ct}) impedance contributions as a function of cycling for films with rough/disordered and smooth/compact morphologies. Highlighted in the panels are the total change in impedance over 5 consecutive cycles. (d) A schematic illustration of the mechanism that enables improved performance in smooth, compact catalyst films based on results of imaging and *in-situ* EIS analysis.

Additional benefits of a smooth catalyst film are elucidated by the evolution of the remaining circuit elements describing the battery electrode. Over the course of operation, the ESR of rough films increases by 6.3% compared with a decrease of 8.8% for smooth films. The degradation in conductivity of the underlying metal-oxide layer for rough films is attributed to the loose packing of catalyst particles which enables the nucleated discharge product to grow at the interface between the catalyst layer and the current collector, disrupting electronic contact to the active catalyst particles. This effect is characterized by SEM imaging in which images depict a thick insulating film at the interface between the current collector and a loosely-packed, dislodged Mn_2O_3 aggregate. The presence of this additional insulating layer below the catalyst film serves to increase the effective thickness of the insulating layer between the current collector and the redox-active surface, hampering electronic conduction. Finally, an analysis of the charge-transfer resistance during cycling of the battery reveals a steadily decreasing resistance for both smooth and rough catalyst films. This effect is similar to that discussed in previous studies and implies a decreasing kinetic resistance over time due to the rearrangement of the electrode morphology that promotes ion conduction directly to the surface.[136] The sum of these individual resistance values comprise the overall cell impedance and provide a fundamental insight into the nature of the overpotential and the relationship this value has with the morphology of a catalyst layer.

7.6 Conclusion

Overall, this study demonstrates the importance of a uniform, homogenous, and compact morphology on the mechanistic performance of a lithium-oxygen battery. To accomplish a compact film with a smooth morphology, we developed a technique to coat three-dimensional mesh substrates with catalytic Mn_2O_3 nanoparticles using electric-field assisted (or electrophoretic) deposition processes, which were compared to catalytic films produced by evaporative methods that are commonly employed. We demonstrate a reduction in the overpotential by over 50 mV for ORR and 130 mV for OER using smooth catalyst films combined with a cycle-over-cycle degradation of the overpotential that is nearly 2X lower. *In-situ* EIS measurements combined with imaging after subsequent charging and discharging of the battery reveal these differences to be directly correlated with the morphology-directed growth of insulating discharge product and the impact this has on morphology evolution of the catalyst film. Specifically, EIS and imaging results indicate increased overpotential and cycle-over-cycle overpotential increase that is due to irregular growth of discharge product that both deactivates catalytic material and leads to the formation of irreversible and insulating side products. Compact and smooth-morphology films overcome this due to a uniform volumetric accommodation of stresses generated during discharge product formation that maintains the integrity of the compact and mechanically/electrically connected nature of the catalyst film. This work implies the generation of highly uniform coatings of nanostructures on 3-D materials presents as large of a challenge for lithium-oxygen batteries as the quest to identify and exploit catalyst materials for these systems. Further, whereas this work has direct implications for lithium-oxygen batteries, such ideas can be straightforwardly transferred to other systems where catalyst coatings are relevant to device operation, including fuel cells and photocatalytic systems.

CHAPTER 8

Nanomanufacturing Li-S Batteries

8.1 Introduction

While the previous two chapters have emphasized the essential role of a carbon current collector for the realization of next-generation Li-O batteries, the realization of Li-O batteries in commercial applications is assumed to be decades away due to the poor energy efficiency and reversibility attainable with today's electrocatalysts. However, Li-S batteries, which boast similar energy densities to that of Li-O batteries are currently being commercialized and as recently as 2013 have been introduced for applications such as flying drones or portable electric vehicles. On this front, the optimization of the carbon current is similarly essential for this technology as the insulating Li_2S discharge product presents similar challenges to that of insulating Li_2O_2 or electrocatalysts.

Lithium-sulfur (Li-S) batteries are poised to replace current generation Li-ion batteries due to a myriad of attractive features including high energy density (2600 Wh kg^{-1}), low-cost, natural abundance and environmental safety.[137-140] However, many challenges still exist regarding the efficient utilization of elemental sulfur as a cathode material due to the poor electronic conductivity and the dissolution of intermediate reaction products that severely impede the reversible capacity and lifetime of Li-S batteries.[141] To overcome these challenges, research has focused largely on the pairing of sulfur with carbon-based composites to enhance the electrical conductivity of the electrode while minimizing polysulfide dissolution and maintaining mechanical integrity during the large volumetric expansions and contractions that accompany cycling.[142-144] On this front, substantial progress has been made in implementing porous carbon or functionalized carbon electrodes to mitigate capacity loss and obtain exceptional energy densities.

However, approaches demonstrating high performance have commonly made use of a single melt-infiltration technique to form sulfur-carbon composite materials, commonly requiring a large mass of material in powder form, additional binders, additives, or extra materials outside of the native electrode materials and sulfur as well as additional processing steps following infiltration in order to produce a suitable film for electrode fabrication.[145] Commonly, specific cathodic performance is characterized independently from the mass introduced due to extra cathodic components (e.g. binders, membranes, etc.), even though unlike carbon-based lithium-ion battery anodes, all added materials outside of sulfur in a Li-S battery cathode are equally passive to the conversion chemistry of the sulfur active material.[146-148] Therefore, for lithium-sulfur battery performance to practically exceed conventional lithium-ion batteries, industry-scalable techniques to achieve high sulfur loading (> 70%) relative to all additives and components of the cathode template must be achieved[149-151] while simultaneously preserving the native specific capacity of the (insulating) sulfur active material. Until now, the few reports of high specific sulfur loading that matches these criteria indicate downfalls in storage capacity and cycling performance.[152, 153]

On this front, research efforts focused on carbon-based cathodes have been centered on improved performance based on either pore confinement[154-157] and/or surface functionalization[158-160] where sulfur infiltration yields low loadings < 50 wt% or multiple long-duration steps until a usable battery material can be realized.[161] Whereas alternative approaches to melt infiltration have been proposed,[162-164] the incorporation of sulfur into porous structures is best achieved through melt-infiltration leaving this as a benchmark technique in the research community.[142] High performance in lithium-sulfur cathodes involves a quartet between high loading of sulfur relative to the entire composite (> 70 wt.%), high capacity (> 1000 mAh/g_{sulfur}), excellent cycling performance (near 80% retention after 100 cycles), and high Coulombic efficiency (> 98%). Despite intense widespread research on lithium-sulfur batteries, only a few reports have emerged that indicate such combined levels of performance. A recent examination of 274 Li-S papers revealed that most sulfur cathodes utilize material fractions of 30-70% which prohibit competitive performance with commercialized Li-ion cells. Additionally, less than half of these papers reported any information at all regarding the sulfur loading, prohibiting a direct comparison with other electrode architectures.[149]

In this report we demonstrate a simple isothermal technique where the high surface free energy of nanoscale pores or surfaces drives the spontaneous nucleation of sulfur liquids until thermodynamic equilibrium between source and cathode is reached. Unlike melt infiltration where such small pores are thermodynamically inaccessible, our approach achieves more complete and uniform coating in addition to highly repeatable sulfur loadings exceeding 80 wt.%. The total amount of sulfur infiltrated into the material is directly determined by the structure of the composite leading to a process that introduces an optimized mass of sulfur in idealized geometric locations. In turn, this leads to devices based on carbon black containing electrodes that outperform the combined cycling, capacity, sulfur loading, and charge efficiency of other reports. The thermodynamic origin of this process presents a unique coating mechanism whereby the most active regions of the electrode are coated first and this process is confirmed experimentally by establishing the thermal activation barrier for coating. We also demonstrate the capability to scale-up this process to a benchtop roll-to-roll coating platform by leveraging the rapid nature of this approach compared to other conventional routes.

8.2 Materials and Methods

To fabricate carbon films, 50/50 mixtures of single-walled carbon nanotubes (NanoIntegris) and carbon black particles (Super C45, MTI) (SWCNT/CB) were bath sonicated in N-Methyl-2-pyrrolidone (Aldrich, 99.8% anyhdrous)) for 1 hour at a concentration of 2mg/mL. The solution was then cast onto stainless steel mesh discs and dried for 12 hours under vacuum. To achieve sulfur deposition, the carbon-loaded mesh discs were placed on a slightly raised surface inside a small sealed stainless steel vessel with a reservoir of 10 mg of sulfur powder (Sigma Aldrich, 99.98%).) beneath the electrode. The entire vessel was heated to 155°C for 45 minutes and the electrodes obtained an average sulfur loading of 74 wt %. The electrode was directly employed as cathode in a CR 2032 stainless steel coin cell (MTI) with a lithium foil anode, 2500 Celgard separator wetted with 1M LiTFSi (Aldrich, 99.95 %), 0.25M $LiNO_3$ (Aldrich, 99.99 %) in a 1:1 mixture of DME (Aldrich, anhydrous 99.5 %) and DOL (Aldrich, anhydrous 99.8 %). The coin cell and electrolyte were prepared in an argon glove box with <0.5 ppm O_2.

In order to directly compare vapor-infiltrated lithium sulfur battery cathode with the typical melt infiltration method, a 50/50 SWCNT/CB powder was combined with powder sulfur in a 1:9 ratio by mass. Melt infiltration was performed by heating the carbon/sulfur composite to 155ºC for 12 hours. The resulting melt infiltration loading was 86 wt% sulfur. This composite was then mixed with CB and PVDF in 85:7:7 by weight and a few drops of NMP and bath sonicated for 1 hour. This solution was then cast onto stainless steel mesh electrodes for a resulting sulfur loading of 74 wt% which is equivalent to the loading obtained through vapor-phase condensation. The cathode was fabricated into coin cells in the same manner as the previous samples. Electrical testing was carried out using an MTI 8 channel battery analyzer and Electrochemical Impedance Spectroscopy was performed using a NOVA Autolab system. Scanning Electron Microscopy (SEM) (Zeiss, Merlin) and Scanning Electron Microscopy Energy Dispersive X- ray Spectroscopy (STEM EDS) (Osiris) were preformed.

8.3 Optimizing Sulfur Coating Processes for Carbon Current Collectors

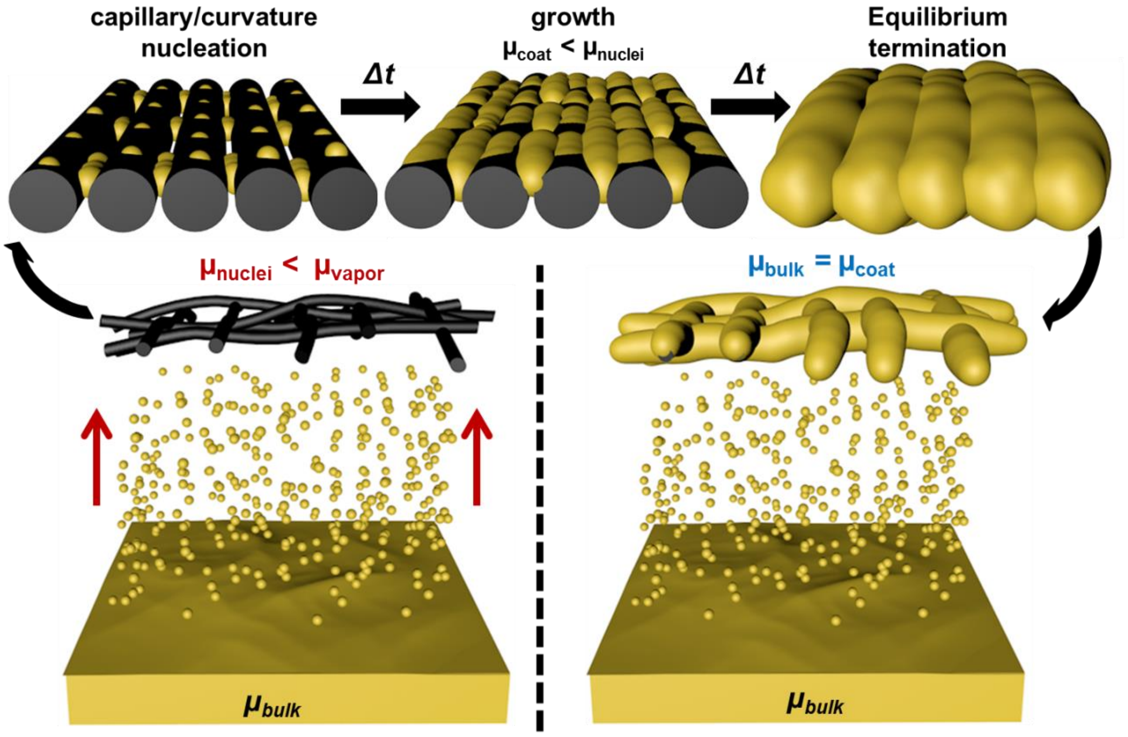

Figure 8.1. A Schematic representation of the vapor- condensation infiltration process used to load pre-formed carbon anchoring materials with elemental sulfur. By maintaining a uniform temperature of the entire system to produce a sufficient vapor pressure of sulfur, capillary condensation in the porous regions of the electrode and on curved surfaces within the electrode facilitate liquid sulfur nucleation from the vapor phase. The driving force to coating the entire electrode relies on a minimization of the electrochemical potential of the liquid nuclei until the electrochemical potentials of both the bath and the coating are equivalent.

The general thermodynamic concept of rapid isothermal vapor infiltration of sulfur into carbon scaffolds is presented in Figure 8.1. In this process, liquid sulfur maintained in a sealed chamber at low temperature reaches thermodynamic equilibrium through the generation of a fixed vapor pressure of sulfur in the chamber. A carbon-based template supporting the sulfur cathode, which is composed in our case of pre-formed combined single-walled carbon nanotubes and carbon black material, is placed at a height of ~ 1 mm above a reservoir of molten sulfur at the base of the sealed container. Based on conventional thermodynamics involving bulk materials, one would expect a fully isothermal system to exhibit balanced mass transport of sulfur vapor to and from the carbon composite and therefore negligible sulfur coating. However, condensation onto the composite can be achieved by introducing a thermal gradient, such as in the sulfur frost (low-pressure vapor deposition) method,[165] but the limitation in such a process is that as sulfur vapor loses energy approaching the cooled carbon cathode it begins to agglomerate, causing thick surface coatings of sulfur as opposed to conformally coated carbon cathodes. Using this technique, we observe poor penetration of the sulfur into the interior of the cathode (Figure 8.2) which explains previously observed poor cyclability,[166] as sulfur does not possess high surface area in contact with conductive carbon or protection from polysulfide shuttling.

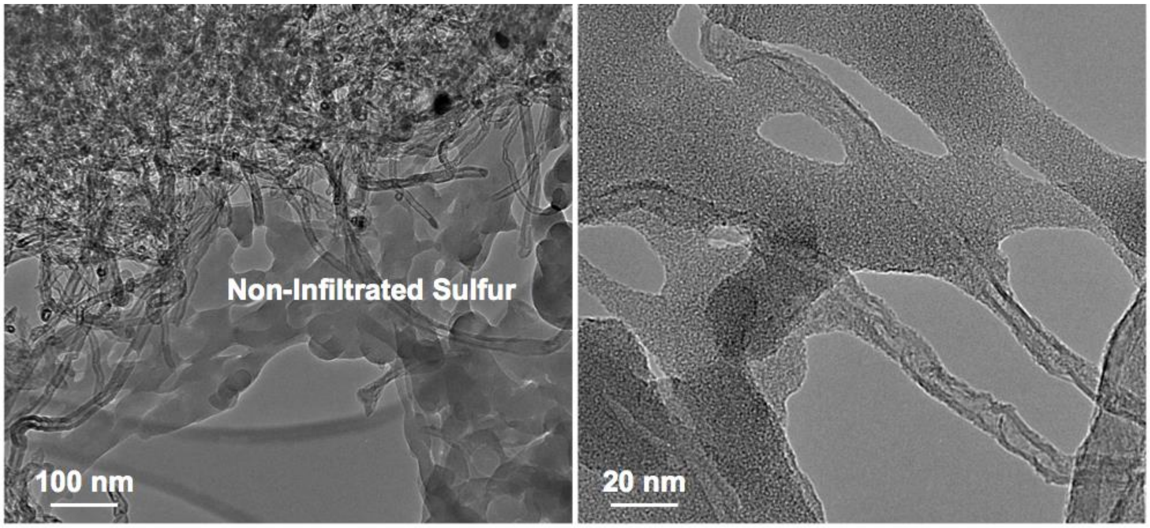

Figure 8.2. TEM images of cooled-substrate vapor infiltrated into CNTs revealing non-uniform deposition and exterior excess.

In our experiments we observe high sulfur loading in an *isothermal* system where no thermal gradient is introduced. Whereas this appears contradictory to convention, this is enabled by capillary condensation of the sulfur vapor, driven by the high surface free energy of the nanoscale pores and curved surfaces in the carbon. At the point of nucleation, the high radius of curvature at these sites leads to the preferential, spontaneous nucleation of sulfur liquid on the cathode material in the smallest pore features due to the free-energy driven difference in chemical potential (μ) between the sulfur nuclei and the sulfur vapor (Figure 8.1). After nucleation occurs, $\mu_{coating}$ remains greater than than μ_{bulk} leading to a process where further mass accumulation occurs until reaching an equilibrium state where $\mu_{coating} = \mu_{bulk}$, and the process is complete. This method of sulfur infiltration provides a self-limiting process whereby the amount of sulfur loaded into the material is determined by the material system and a repeatable, optimized loading of sulfur in the carbon matrix is consistently achieved. The final equilibrium state involves a carbon material where all surfaces are conformally coated with a layer of sulfur such that the surface free energy of the coated cathode and the surface free energy of the bulk liquid are similar.

To investigate the origin of this process, we carried out kinetic studies where the SWCNT-CB cathode material was exposed to different durations of isothermal treatment at three different temperatures (135 ^{o}C, 155 ^{o}C, and 175 ^{o}C) and the total specific sulfur loading was measured (Figure 8.3a). In all cases the loading curves represent a decaying exponential function indicating temperature-activated kinetics in accordance with the thermodynamic picture emphasized in Figure 8.1. By fitting these kinetic profiles to a self-limiting, decaying exponential function, we extracted values for the sulfur growth rate (v), the characteristic time for equilibrium sulfur coating (τ), and the activation energy (E_A) for the continuous isothermal growth of sulfur onto the cathode template. In all cases, after less than 60 minutes of total isothermal processing, sulfur loading > 70 wt.% relative to all components of the carbon cathode is achieved. At the highest temperature of 175^{o}C, we consistently observed both the fastest (~ 10 minutes), and the highest loading (~ 82 wt.% sulfur). By slightly decreasing the isothermal temperature to the same temperature used for melt infiltration (155 °C due to the low viscosity of liquid sulfur at this temperature),[167] an equilibrium loading of ~ 75% was achieved after 40 minutes. Similarly, areal loadings closely matching commercial Li-ion and state-of-the-art Li-S batteries were achieved using a coating of 1 mg/cm^2 of carbon materials. After exposure to the isothermal infiltration process at 175 ^{o}C, a loading of 75 wt.% was achieved corresponding to an areal density of 3 mg/cm^2 and uniform penetration throughout the entirety of the sample was observed through cross-sectional and top-down SEM imaging (Fig. S3).

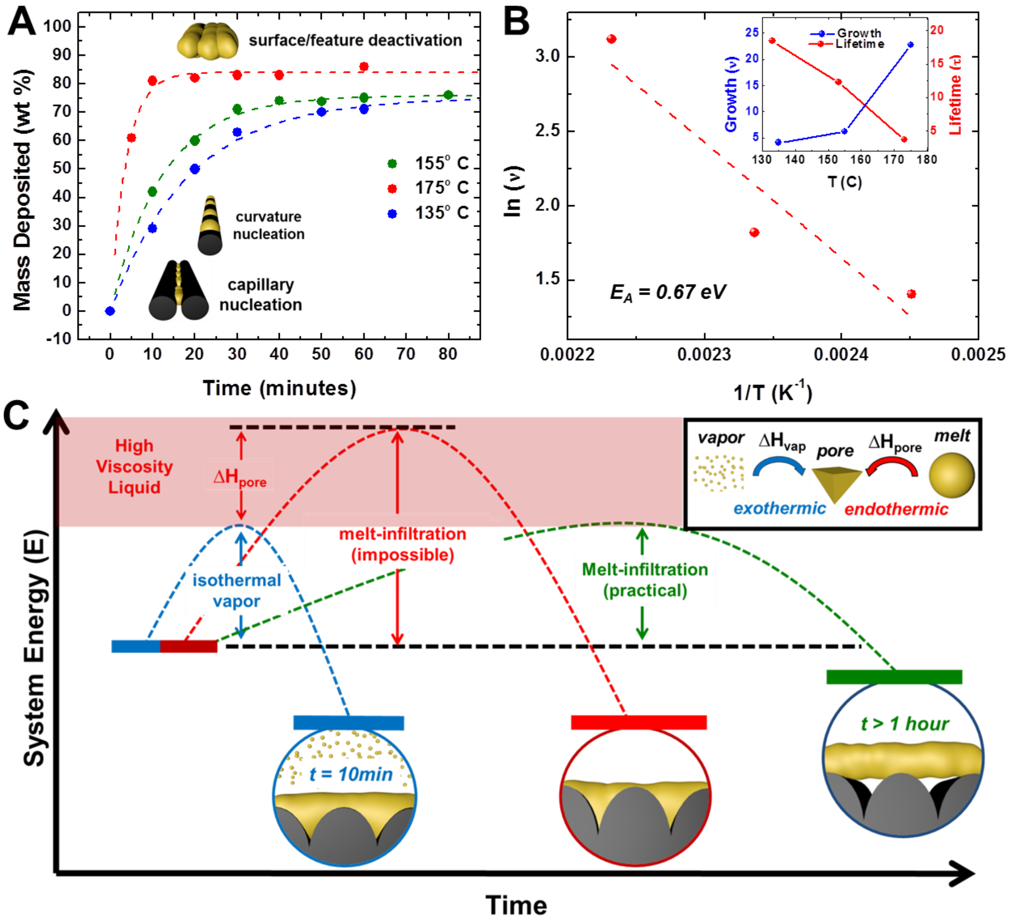

Figure 8.3. (a) Sulfur loading with respect to time for three different temperatures using the vapor-condensation process with inset schematics depicting condensation nucleation and saturation points. (b) Arrhenius plot for the growth rate of the sulfur film vs. 1/T. A linear fit to the data is shown by a dotted line with an inset depicting the specific values for growth rate and lifetime obtained at each temperature. (c) Energy diagram depicting the evolution of the system energy during the coating process.

Compared to melt infiltration processes, where durations > 10 hours are commonly required to achieve moderate sulfur loading in nanoscale carbon materials, our isothermal vapor process significantly decreases the time (up to 12X) associated with sulfur loading and yields higher (conformal) loading than that reported for effective melt-infiltrated lithium-sulfur battery cathodes. Compared with the cost of NMP-based electrode fabrication processes, the requirement of an additional melt-infiltration step yields over a 4X increase in the fabrication cost unlike vapor-infiltration in which the additional cost incurred is nearly a third of traditional fabrication costs. Additionally, vapor infiltration leads to over 20X improved carbon footprint compared to melt infiltration – yielding industry-level feasibility while enabling improved device-scale loading (Figure 8.4).

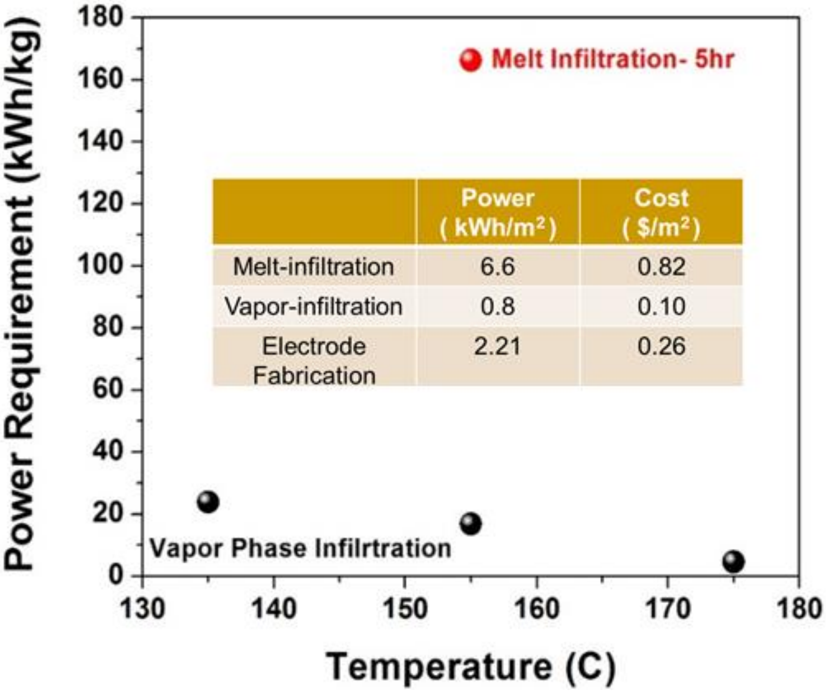

	Power (kWh/m^2)	Cost (\$/m^2)
Melt-infiltration	6.6	0.82
Vapor-infiltration	0.8	0.10
Electrode Fabrication	2.21	0.26

Figure 8.4. Power requirement for vapor phase infiltration at various temperatures to obtain 70 wt% S loading compared to melt infiltration for 5 hours. The inset table describes the cost associated with melt-infiltration or vapor-infiltration of sulfur materials compared with the cost of fabricating electrodes from NMP solution. In the calculations, an areal sulfur loading of 4 mg/cm^2 and an electricity cost of \$0.12/kWh is assumed.

In this spirit, Figure 8.3c presents process pathways that illustrate the mechanistic difference in melt and vapor infiltration to explain the improved loading characteristics. During melt infiltration, sulfur liquid is mixed with carbon materials and exposed to long thermal processing to drive the liquid into the porous regions of the carbon matrix. The use of temperature (and time) enables the sulfur to overcome the activation barrier to separate from bulk and fill the nanoscale voids in the porous material. However, filling the smallest nanoscale pores with liquid – which implies increasing the free energy of the sulfur relative to that of bulk sulfur, only occurs when the temperature used in melt infiltration can overcome an energy barrier that increases as pore size decreases. In turn, prior studies using melt infiltration to produce highly nanoconfined Li-S cathode architectures yielded a trade-off of low specific loading less than ~ 50% and demonstrated the inability of sulfur to completely utilize the entire pore volume.[154-157] As emphasized in Figure 8.3c, the ceiling of thermal energy that can be supplied to melt infiltration is limited by sulfur polymerization that occurs at higher temperature. On the other hand, our vapor process is *initiated* by nuclei that form in the highest energy (smallest size) pores and crevices of the cathode material that are not accessible by melt infiltration. This leads to an ideally uniform and conformal coating where sulfur is able to access the smallest pores, yielding improved loading (up to 82 wt.%) in the smallest and most active pores in the cathode that are not accessed in melt infiltration. Conformality of the coating is demonstrated by scanning electron microscope (SEM), Transmission electron microscope (TEM) images, and energy dispersive x-ray maps (Figure 8.5) that show uniform penetration of the sulfur into the SWCNT/CB composite material. However, it is important to note that the improvement achieved through our vapor infiltration method *could be* achieved through melt infiltration if the temperature of the melt was increased, although the polymerization regime prevents this. Based on principles of energy conservation, the improved loading from isothermal vapor infiltration is equivalent to increasing the temperature of melt infiltration by T, where $C_pT = H_{vap}$ where C_P is the heat capacity of molten sulfur (49.9 J mol^{-1} K^{-1}), and H_{vap} is the enthalpy of vaporization of sulfur (9.8 kJ mol^{-1}). This implies that nucleating a sulfur coating from the vapor phase at a given temperature enables the process a total amount of energy of $C_PT + H_{vap}$ to overcome the barrier to pore filling (opposed to simply C_PT for melt infiltration), leading to more uniform higher loading and a lower final free energy state for the sulfur-carbon composite after infiltration at a fixed temperature. Using values for heat capacity and enthalpy reported elsewhere,[168] we calculate the total energy of sulfur vapor to be equivalent to sulfur liquid heated an additional 196°C. This thermodynamic argument, which is fully consistent with the first and second laws, is generally illustrated in Figure 8.2c. Further building from kinetics data presented in Figure 8.2a, the formation of a sulfur coating from a vapor phase also occurs appreciably faster than the infiltration of a liquid into a nanoporous composite. This means that in addition to boosting the sulfur loading, this process occurs at up to a 30X faster rate. Since our calculations emphasize that the greatest energy input to cathode fabrication for both methods is maintaining the temperature over the duration of infiltration, this gives a simultaneous route to lower the manufacturing cost and carbon footprint, improving throughput, and also improving loading. Such energy savings could drastically improve the commercialization of sulfur batteries as nearly half of the total cost from traditional battery manufacture originate from the fabrication process and cathode materials cost.[169, 170]

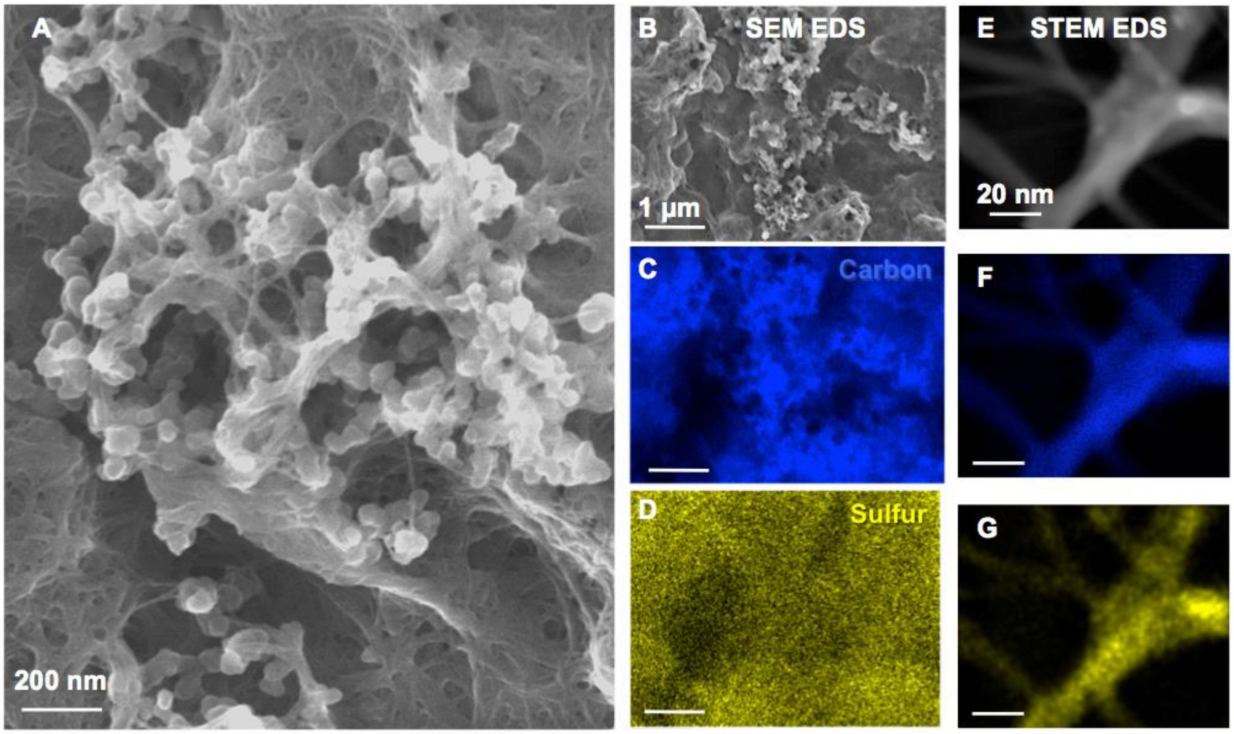

Figure 8.5. (a) scanning electron micrograph (SEM) showing surface morphology of 50/50 SWCNT/CB pre-formed carbon film a 74 wt.% sulfur loading. (b) SEM image of the area over which energy dispersive x-ray spectroscopy (EDS) analysis was performed, (c) SEM EDS map of elemental carbon and (d) sulfur. (e) scanning transmission spectroscopy image of a SWCNT

bundle condensed with sulfur and corresponding (f) STEM EDS elemental carbon map and (g) STEM EDS sulfur map

8.4 Superior Performance Over Melt-Infiltration

Whereas the results so far give promise to improving lithium-sulfur battery cathodes, we further carried out experiments to test the effectiveness of sulfur cathodes produced using this technique and compared the performance to equivalent materials infiltrated using melt-infiltration. Full details on the experimental preparation methods are available in the supporting information. To compare the two techniques, we used SWCNT/CB networks containing sulfur at 74 wt.% infiltrated using melt and vapor-condensation methods at 155 °C. This loading was chosen due to the low viscosity of sulfur at this temperature and the challenge of preparing higher sulfur loading with melt infiltration as the conductivity of the composite cathode is drastically diminished for high sulfur contents (Figure 8.6).

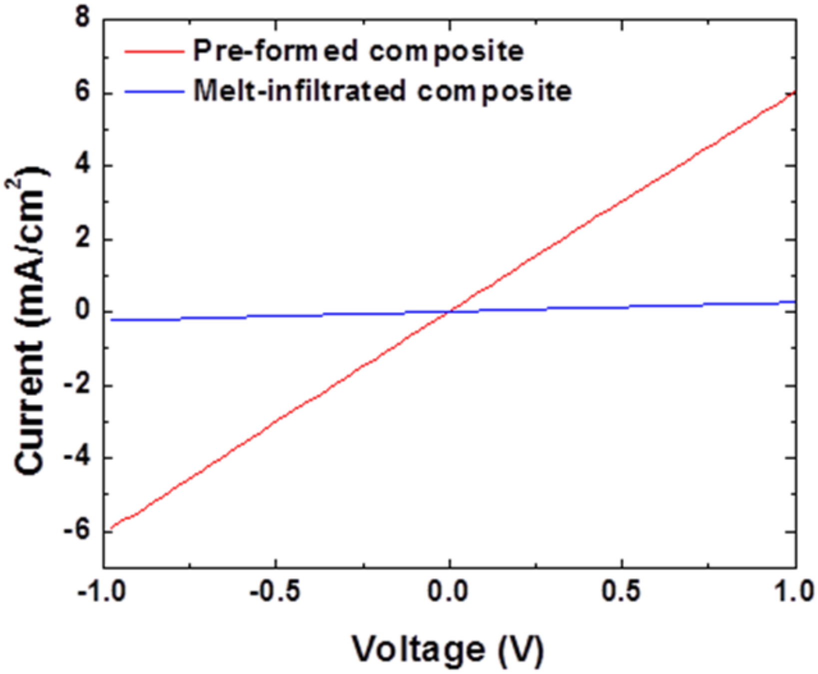

Figure 8.6. I-V curves of pre-formed and melt-infiltrated SW/CB films at 74 wt% S.

Galvanostatic testing of both cathodes at rate of 0.1 C (C = 1,675mA/g_{Sulfur}) are shown for the first cycle of both cathode materials in Figure 8.7a. The vapor infiltrated cathode delivers an initial discharge capacity of 1015 mAh/g_S (~759 mAh/$g_{electrode}$) while the melt-infiltrated sample delivers 768mAh/g_S (~568 mAh/$g_{electrode}$). The increase in initial discharge capacity for the vapor-infiltrated cathode is attributed to both (i) an improved uniformity of the vapor coated sulfur film that extends into the narrowest pores in the material, and (ii) enhanced charge-transfer to the site of lithiation facilitated by the absence of additives and binders in the cathode material.

These cathode materials were further examined using Electrochemical Impedance Spectroscopy (EIS) measurements (Figure 8.7b). EIS indicates that the charge transfer resistance (R_{CT}) for the vapor infiltrated sulfur cathode is approximately 2X lower in comparison to the melt infiltrated cathode. Here, R_{CT} represents the effective barrier for electron flow between the active site where lithiation occurs and the current collector. The results in Figure 8.4b imply that (i) the vapor infiltrated cathode exhibits a less torturous pathway across SWCNT junctions that are required for electrical addressability, whereas melt infiltration processes clog the critical electrical transport pathways by insulating coatings of sulfur material (Figure 8.7b, inset), and (ii) the sulfur coating with vapor infiltration is more uniform than with melt infiltration. Additionally, when examining the cathode charge profile (Figure 8.7a, inset), the potential barrier prior to the first charge plateau that is characteristic to sulfur batteries is diminished for the vapor infiltrated sulfur cathode. This potential barrier is attributed to a barrier of charge transfer between electrolyte and lithium sulfide during charging,[171] and this observation of a decreased barrier in the vapor infiltrated charge curve is consistent with the measurements obtained through EIS.

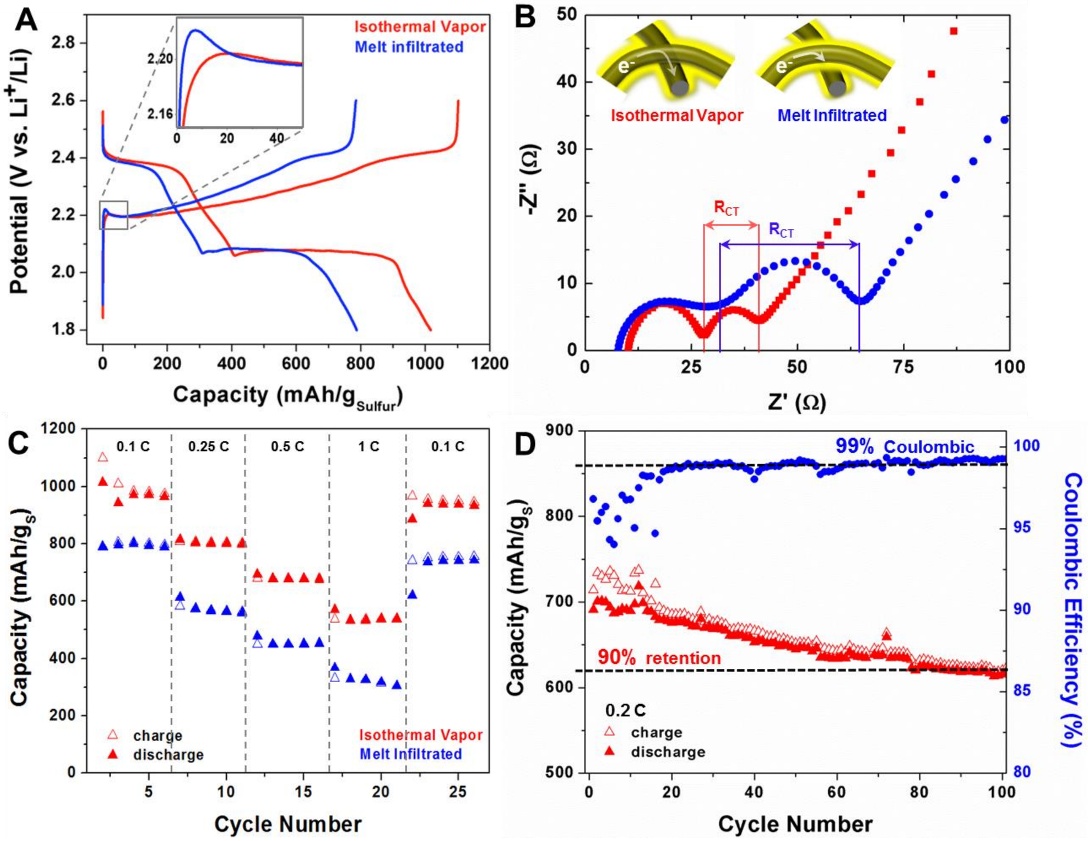

Figure 8.7. (a) galvanostatic charge-discharge of a melt infiltrated and condensed cathode at 0.1 C with an inset depicting the potential barrier on charge. (b) Corresponding Nyquist plots obtained using electrochemical impedance spectroscopy with a graphical inset of SWCNT junctions for each sulfur infiltration method explaining the variations in $R_{CT.}$ (c) Galvanostatic rate study at 0.1, 0.25, 0.5, 1, and 0.1 C rates for each cathode and (d) galavnostatic cycling behavior of condensed cathode at 0.2C

Over the course of 100 cycles at a rate of 0.2 C, the vapor infiltrated cathode exhibits 89% capacity retention (Figure 8.7d). This level of capacity retention is, to the best of our knowledge, the highest reported value in conjunction with high sulfur loading from any current state-of-the-art reports[150, 172] and is enabled by the ideal cathode morphology produced in this vapor infiltration technique. Additionally, the Coulombic efficiency at the 100th cycle is > 99%, which is an indicator of a stable and highly reversible conversion process. Whereas many reports indicate excellent cathode performance metrics in one area with trade-offs in other metrics, cathodes developed using this technique combine a quartet of key performance metrics that are both independently and collectively surpassing current state-of-the-art reports. This includes (1) a total cathode composite capacity of > 1,000 mAh/$g_{electrode}$ normalized to *all* cathode components, (2) ~ 90% cycling retention at 0.2 C after 100 cycles, (3) specific sulfur loading above 70% with all cathodic components included, and (4) high Coulombic efficiency including a 99.3% efficiency after 100 cycles at 0.2 C. Combined with the lower energy footprint of vapor infiltration processing, this provides a straightforward process that can be widely adapted to improve lithium-sulfur battery performance to practical levels required for commercial impact.[149]

8.5 Manufacturability of the Sulfur Infiltration Approach

Beyond the lab-scale device performance and thermodynamic description of this process, the simplicity and reproducibility of this process can overcome key limitations that have hindered moving beyond current lithium-ion battery technology. For industrial-scale processing, the total number of steps, the duration of those steps, and the reliability of the process dictate the overall manufacturing cost in conjunction with the total energy input to the process, where vapor phase infiltration is superior. The simplicity of this vapor infiltration technique motivates its utility toward scale up processing. In this case, a pre-formed material is infiltrated with sulfur vapor in as little as 10 minutes to achieve high specific loading, and the output is a full sulfur cathode that requires no further processing (Figure 8.8a). Whereas this simplifies large-scale processing routes for such batteries, this approach also brings a marked benefit at the laboratory scale as researchers have devoted a significant amount of effort to the production of controlled and preformed carbon nanomaterials that has largely been disconnected from efforts to develop better lithium-sulfur batteries. This vapor phase technique can be seamlessly “scaled down” where very small, engineered lab-scale samples can be reliably vapor infiltrated with sulfur on a "sample-by-sample" basis – a feature not achievable with melt infiltration. Overall, the decreased number of steps in this process, the lower sulfur infiltration times, and the ability to engage a new and diverse set of carbon templates for sulfur cathodes brings a key step forward in the development of practical cathodes at both large and small scales. To further leverage these ideas, we developed a simple benchtop roll-to-roll platform (Figure 8.8b) where a coated film of SWCNT-CB on a 11 cm x 1.3 cm roll) was infiltrated with 82.5 wt.% by rolling the material through a system designed to operate on a simple bench-top hotplate. Since the sulfur does not condense on bulk surfaces using this technique, full utilization of the sulfur can be achieved in this approach, and no additives or other components are necessary in the cathode manufacturing process. In contrast Figure 8.8c presents a representation of the total number of steps required in the processing of lithium-sulfur cathode material using conventional melt-infiltration, which is currently the primary route utilized to simultaneously achieve high loading and good device performance. In this approach, the melt-infiltration process which can conservatively be limited to only 6 hours of duration for uniform infiltration of nanomaterials only produces a material (not an electrode) which must be further processed into a cathode. This typically involves sonication of the material after infiltration and combining a PVDF binder and carbon black to an active material, which can then be cast and dried as a slurry into a cathode. The drying step is also slow (approx. 6 hours) leading to an overall sluggish process from composite elements to complete electrode. Overall, we believe that the improvement on all fronts enabled by this vapor phase infiltration technique will liberate many of the current barriers that are limiting current advances in lithium-sulfur battery materials from penetrating the energy storage marketplace.

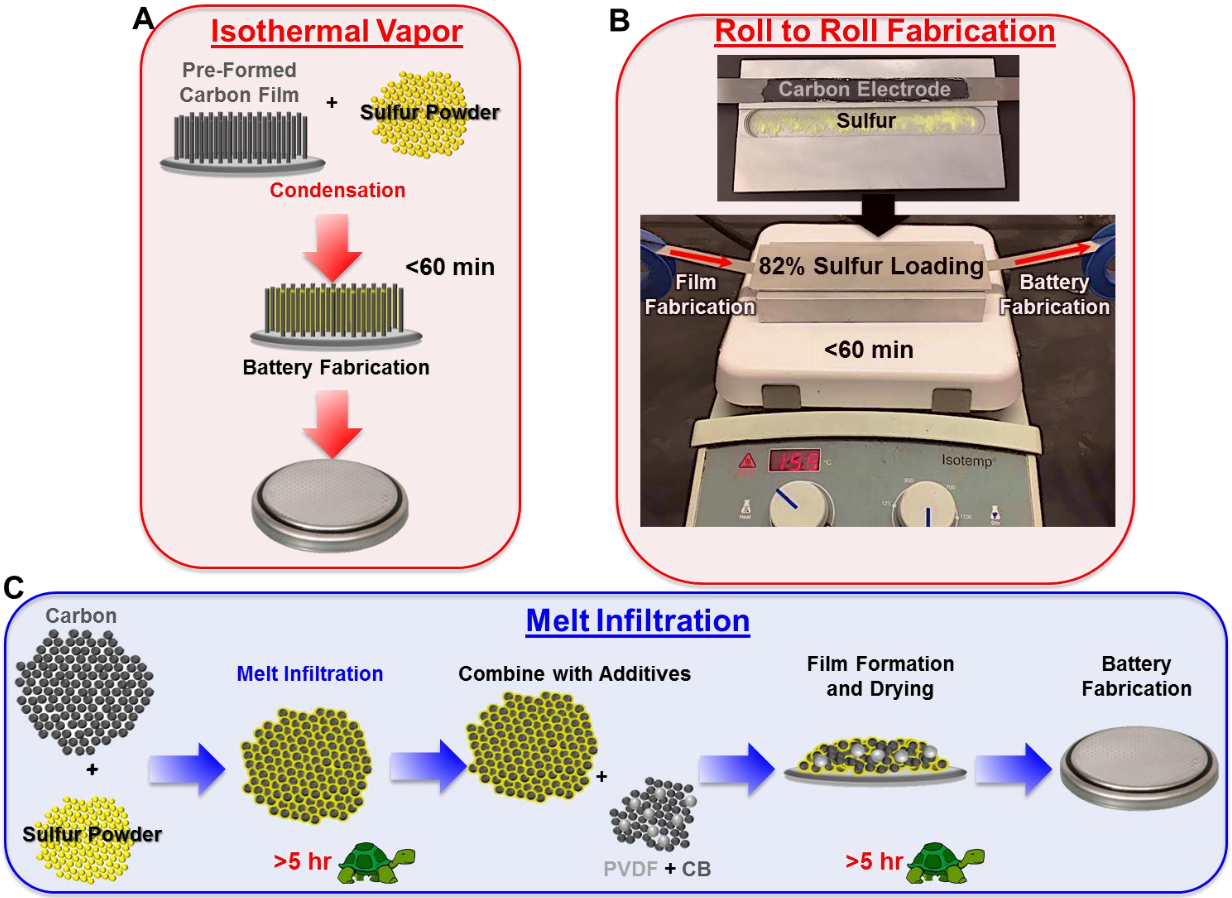

Figure 8.8. (a) Schematic representation of the process for creating usable cathode materials from the vapor-infiltration process and corresponding (b) optical photographs of a large-scale, roll-to-roll system using the vapor condensation sulfur loading process. (c) Schematic illustration of the processing steps required for creating usable cathode materials from conventional melt infiltration processes.

8.6 Conclusion

We have presented a simple vapor-phase infiltration process to load pre-formed films of carbon nanomaterials with high loadings of sulfur. The self-limiting nature of this approach permits repeatable loading of sulfur material over large substrate areas at low temperatures. At a loading of 74 wt %, the assembled composite cathodes exhibits an initial discharge capacities of over 750 mAh/$g_{electrode}$ with an exceptional capacity retention of ~90% after 100 cycles and significantly outperforms similar device architectures fabricated with the traditional melt-infiltration technique. With careful design of an ideal pre-formed anchoring material, the initial discharge capacity can be greatly enhanced while maintaining exceptional cyclability and high sulfur loadings. The low power consumption of this process combined with roll-to-roll process ability provides exceptional promise to this technique as a method for commercial fabrication.

CHAPTER 9

Optimizing Carbon Structure for Sulfur Condensation

9.1 Introduction

Typical methods for optimizing the performance of an all-carbon sulfur composite involve optimization of the porosity of the carbon electrode or the introduction of functional groups to the surface that overcome the performance limitations of *sp*^{2} carbons.[164, 173, 174] To achieve exceptional durability and sulfur utilization through pore size alone requires the implementation of ultra-small nanometer and sub-nanometer pores to retain low-order polysulfides and maintain the necessary contact area during battery operation. Unfortunately, however, such small pores are capable of only modest sulfur loadings and, despite exceptional efficiency and durability, the energy density of the composite electrode lags far behind approaches that opt for larger pore sizes in lieu of higher sulfur loading.[145, 175, 176] To overcome these limitations, the surface chemistry of the carbon electrode may be separately optimized through the addition of oxygen-containing functional groups to the surface that improve the binding between the conductive carbon matrix and active sulfur compounds.[177-180] The strong binding of sulfur to oxygen improves the anchoring of lithium polysulfides and, consequently, the cyclability of the composite electrode.[181-183]

In this study, we optimize the fabrication process for carbon-sulfur electrodes by pre-defining the conductivity and defect density of the carbon electrode through solution processing. By combining conductive SWCNTs with defective CNHs using electrophoretic deposition (EPD), we optimize both the defect density and conductivity of the entire electrode before coating these interconnected networks with a low-temperature vapor-phase infiltrate route that minimally influences the electrode conductivity. By using a high concentration of CNHs, sulfur loadings in excess of 75 wt. % are consistently achieved in less than one hour with a reversible sulfur capacity of over 1200 mAh/g. These results pave the way for designing low-cost, simple electrode fabrication process for exceptional Li-S performance.

9.2 Materials and Methods

To fabricate single-component carbon films, mixtures of SWCNTs (NanoIntegris) and CNHs (Carbonium, Dahlia type) were solubilized in N-Methyl-2-pyrrolidone (Aldrich, 99.8 5anyhdrous) at a concentration of 100 µg/ml. For hybrid films, SWCNTs and CNHs were combined at a ratio of 7:3 and 3:7 to achieve a total carbon concentration in solution of 100 µg/ml. The suspensions were sonicated using a probe sonicator (Sonics, VCX750, 30% amplitude) for 30 minutes with a 3 second ‘on’ pulse and 3 second ‘off’ pulse to avoid excessive heating. All solutions were left overnight before use.

EPD on stainless steel (SS) mesh was performed using a Keithley 2400 Sourcemeter integrated with LabView data acquisition software to apply a constant voltage and record the flow of current. A pristine stainless steel mesh electrode (MTI) was placed 0.5 cm from a stainless steel counter electrode before adding 10 ml of the desired solution. A bias of 100 V was applied to the system for 10 minutes before the solution was slowly drained from the Teflon container with the voltage left on. To infiltrate sulfur vapor into the fabricated carbon films, the coated mesh electrodes were placed on a raised surface inside a sealed stainless container with a reservoir of 20 mg sulfur powder (Sigma Aldrich, 99.98%). The entire vessel was heated to 155^{o}C for 45 minutes before being removed from the oven to cool at room temperature. The sulfonated carbon electrodes were directly employed as a cathode in a CR 2032 stainless steel coin cell (MTI) with a lithium foil anode and a Celgard 2500 separator wetted with a 1M LiTFSi (Aldrich, 99.95 %), 0.25 M LiNO3 (Aldrich, 99.99 %) in a 1:1 mixture of DME (Aldrich, anhydrous 99.5 %) and DOL (Aldrich, anhydrous 99.8 %). The coin cell and electrolyte were prepared in an argon glove box with < 0.5 ppm O_2. Galvanostatic testing of the assembled coin cells was performed using an MTI 8 channel battery analyzer and Cyclic Voltammetry was carried out on a NOVA Autolab system. Raman analysis was performed using a Renishaw inVia Raman microscope with a 532 nm excitation. Zetasizer measurements were performed using a Malvern Zetasizer Nano ZS instrument. I-V measurements were performed by doctor blading a solution of the specified carbon material on a glass slide before infiltrating the film with sulfur using the method described above. I-V testing was performed using a Keithley 2400 sourcemeter.

9.3 Current Collector Design

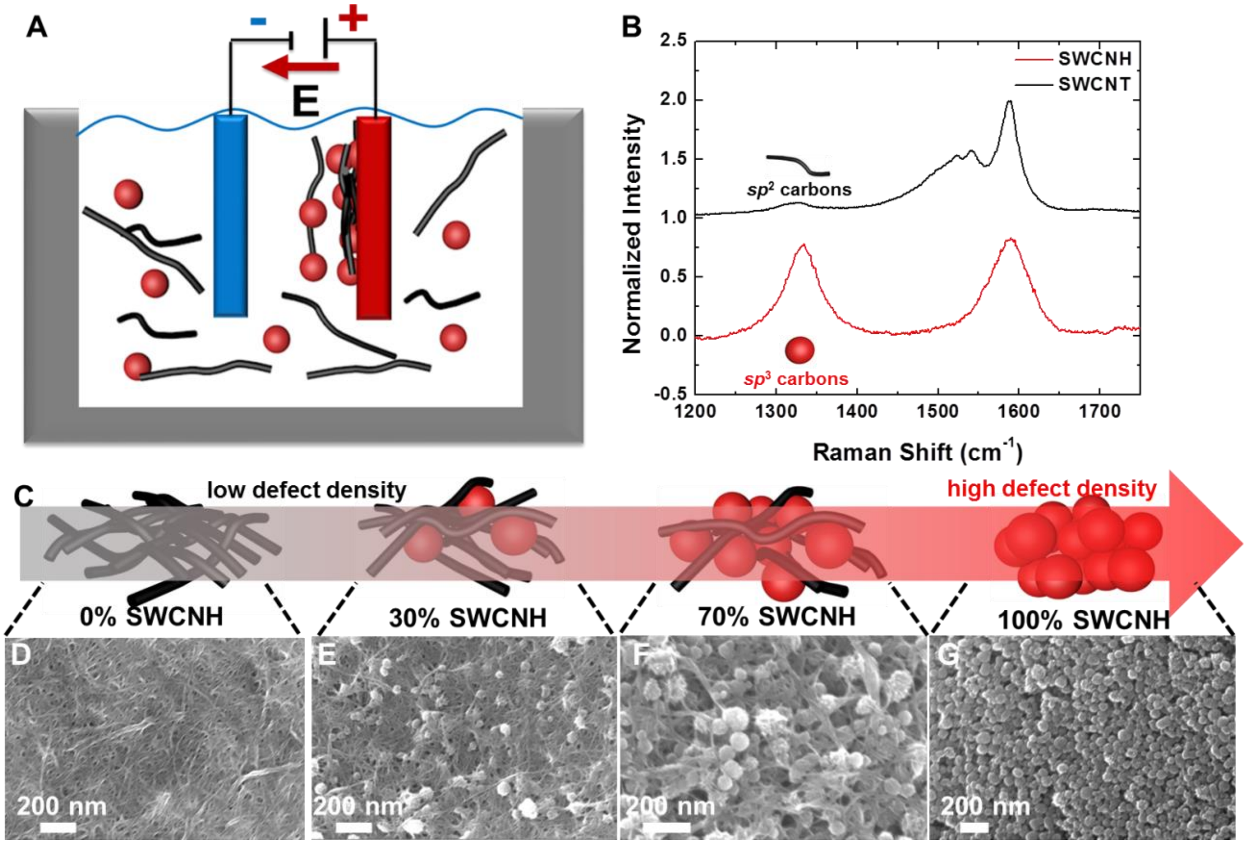

Figure 9.1. (a) Schematic of the EPD process in which ultra-dillute, highly solubilized solutions of SWCNTs and CNHs are assembled onto current collectors. (b) Raman spectra of the component materials highlighting the high *sp*^{3} content in CNH materials. (c) Schematic illustration of the effect of varying the CNH content in hybrid films along with corresponding SEM images in D-G for every ratio tested.

The fabrication process for the composite materials used in this study is outlined in Figure 9.1a. Single-walled carbon nanotubes (SWCNTs) are combined with single-walled carbon nanohorns (CNHs) in 1-methyl-2-pyrrolidone (NMP) solution at varying ratios to produce a composite film with a density of *sp*^{3} hybridized carbon atoms proportional to the content of CNHs. Raman analysis of the individual structures reveals the large intensity of the carbon D-peak for CNHs indicative of a high defect content compared to the SWCNTs (Figure 9.1b) that increases for an increasing concentration of CNHs. CNHs were chosen as the source for defective carbons due to their large size and promising performance at high loadings compared to conventional carbon blacks or activated carbons. [148, 184]

To ensure a uniform dispersion of the defective carbon materials with the more conductive SWCNTs, ultra-dilute solutions of SWCNTs, in which the SWCNTs exist as small bundles and individually solubilized structures,[185] were combined with CNHs and assembled using electrophoretic deposition (EPD). EPD is a proven technique for assembling conformal films of ultra-dillute carbon nanomaterials on 3-D structures and guarantees a high-quality, homogenous coating over the entirety of the substrate material.[58, 128, 186] In this study, EPD was implemented to form a conformal coating of carbon material over a 3-D steel mesh electrode. As emphasized by previous studies employing a mixture of SWCNTs and CNHs in NMP solutions, the similar mobilities of these two solutions (Figure 9. 2), ensures the composition of the assembled film closely matches that of the solution.[186] To study the impact of film morphology and composition on electrode performance, films comprised of individual structures of SWCNTs, denoted '10T' and CNHs, denoted '10H' were fabricated and the assembly and device performance compared with two hybrids synthesized at varying ratios. To isolate the role of CNH concentration in the material, composites with a majority CNHs, namely 70% CNHs and 30% SWCNTs denoted '7T3H', were compared against composites with a majority of SWCNTs, namely 70% SWCNTs and 30% CNHs denoted '3T7H'. A schematic of the role of defective CNHs is presented in Fig. 1C along with SEM images of the assembled composite materials in Fig. 1C-F. In these images, it is clear that both the CNH content and openness of the electrode structure increases with increasing CNH concentration in solution.

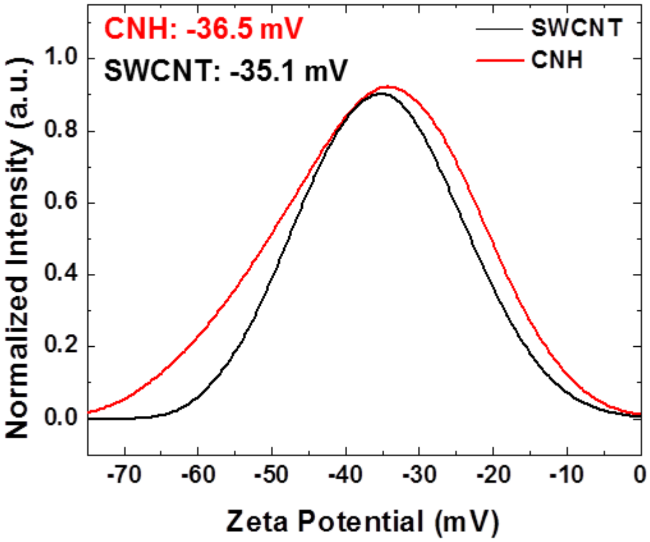

Figure 9.2. Zeta potential measurements of NMP solutions of the nanostructures used in this study. Measurements were performed on solutions with a concentration of 50 µg/ml.

9.4 Coating Sulfur into Designed Current Collector

After formation of the composite film, sulfur was infiltrated up to a loading of between 73 and 80 wt% in each composite using a novel isothermal vapor phase infiltration process. In this process, illustrated schematically in Figure 9.3a, sulfur vapor is provided by a bath of liquid sulfur beneath the composite electrode and condensation of the vapor is used to initiate a liquid coating of sulfur in the carbon electrode. The lower energy provided by the nanoscale capillaries within the composite materials ensures the most porous regions of the electrode are coated first and further growth of the liquid phase is supported by a lowering of the chemical potential of the sulfur liquid nuclei and an overall decrease in the free energy of the sulfur-carbon composite.[179, 186, 187] By maintaining an identical temperature between the substrate and bath, an equilibrium is reached at a coating thickness in which the chemical potential of the coating is equivalent to that of the bath providing a self-limiting mechanism to ensure repeatable coatings amongst the different materials tested. A study of the mass deposition over time in Figure 9.3b for the composite electrodes illustrates the mechanism whereby the open porous nature of CNH films facilitates the vapor infiltration nucleation process leading to more rapid growth rates and higher limiting sulfur contents. To calculate these growth rates, fits to the deposition data were acquired using a decaying exponential indicative of a self-limiting reaction of the form $y = b + \nu\tau + exp\left(\frac{-t}{\tau}\right)$ where ν represents the initial growth rate and τ the lifetime. [188] From this data, it is evident that the presence of CNHs facilitates a more rapid, low-energy infiltration of sulfur at high loadings thereby improving the manufacturability of the composite electrode.

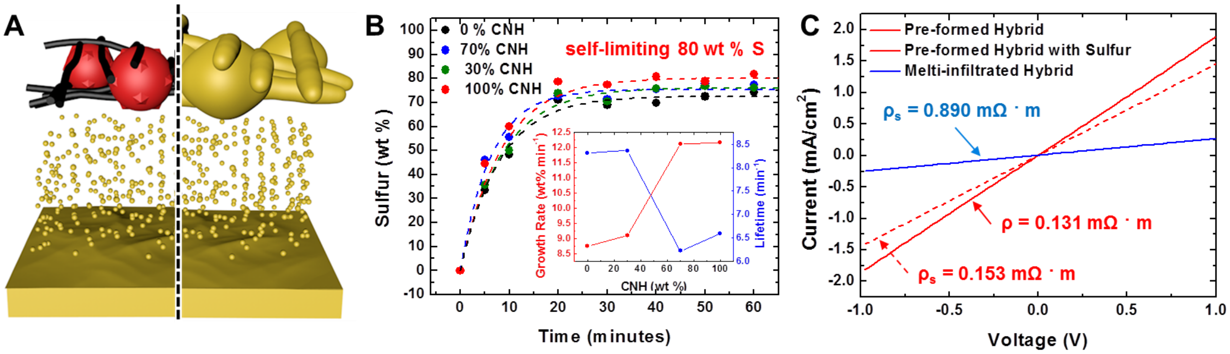

Figure 9.3. (a) Schematic illustration of the sulfur loading process emphasizing the self-limiting nature of the sulfur coating. (b) Mass deposition of sulfur condensed on the various hybrid electrodes over time with insets depicting the growth rate and lifetime of the sulfur coating process. (c) I-V measurements for hybrid samples of 30% CNHs and 70% SWCNTs highlighting the minimal reduction to conductivity that results from vapor-phase sulfonation processes compared with conventional melt-infiltration.

The pre-assembly of films prior to the sulfur infiltration process enables a high degree of film conductivity of the composite at high sulfur loadings. Unlike traditional melt-infiltration processes, which coat powdered materials in an insulating coating prior to assembly, the ability to pre-define the nanoscale contacts in a system before sulfonation ensures a conductive carbon backbone that is not disrupted by the presence of sulfur. In Fig. 3c, I-V measurements performed on 3T7H films before and after sulfur infiltration illustrate the negligible change to conductivity that results from the coating of a pre-formed carbon structure. Nearly an order of magnitude improvement to conductivity is observed for the developed vapor-phase infiltration process compared with conventional melt-infiltration - enabling high conductivity at high defect concentrations and sulfur loadings. Identical conductivity measurements performed over all the hybrid systems investigated in this study is presented in Figure 9.4.

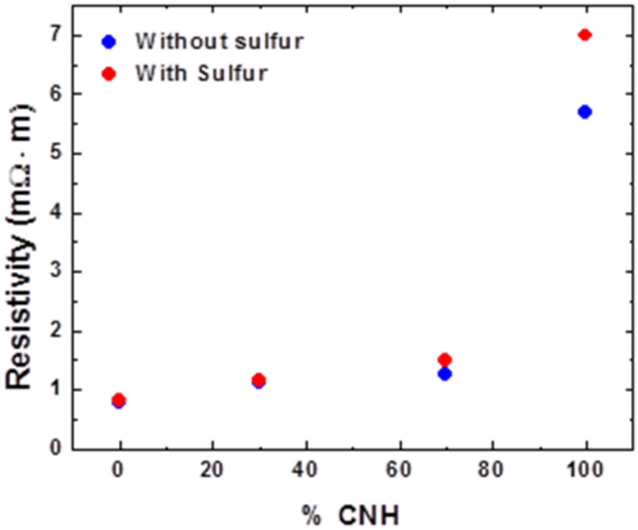

Figure 9.4. Resistivity measurements of the different hybrid materials before and after sulfur coating.

SEM imaging in Figure 9.5a-c illustrates the morphology of the materials after sulfur loading. As evidenced by the outline of the nanostructures still visible in these images, the sulfur is evenly distributed across the entirety of the electrode surface and does not form large aggregates that may severely impede electron transfer. To confirm the conformal nature of the sulfur coating, SEM EDS analysis in Figure 9.5h-k highlights the uniformity in the sulfur coating across all device compositions.

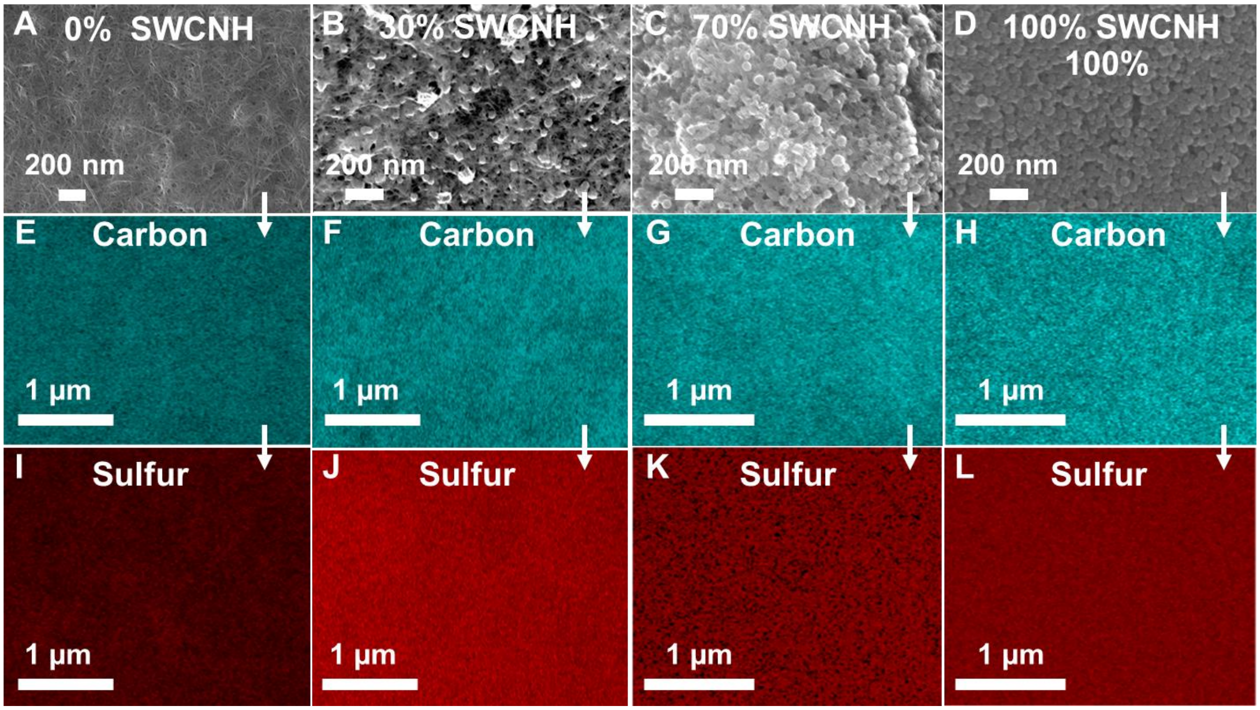

Figure 9.5. (a-d) SEM characterization of sulfonated films for hybrid materials with a CNH content specified by the inset. Corresponding SEM EDS analysis in figures e-l emphasize the uniformity of the sulfur coating over the entirety of the film.

9.5 Device Performance

Device testing of the different composite samples highlights the role of defect carbon materials within the CNHs during operation of the Li-S cell. In Figure 9.6a, galvanostatic charge-discharge performed on both single-particle and hybrid structures at a rate of 0.1 C (C= 1675 mA/g) reveals a large disparity in the energetics and efficiency of sulfur reduction that is dependent on the concentration of CNHs within the material. For all samples tested, during discharge, two distinct regions are observed. The first at ~2.4 V represents the reduction of S_8 to soluble, high-order polysulfides (HOPSs), S_n^{2-} where n = 8, 6, or 4. In this region, without sufficient anchoring, the HOPS are dissolved back into the electrolyte through the "shuttle phenomenon" limiting the total capacity and cyclability of the electrode. After reduction of elemental sulfur to S_4^{2-}, the retained soluble polysulfides are further reduced to low-order polysfulides (LOPSs) comprised of insoluble S_2^{2-} and S^{2-} in a precipitation reaction that is defined by the region that extends from ~2.1 V – 1.8 V. In this region, the capacity is directly correlated to the ability of the electrode to retain the HOPS formed during the initial discharge and nucleate LOPS on the surface. With this in mind, a comparison of the relative capacity of each region determines the ability of the carbon surface to retain the HOPSs and subsequently convert them to the insoluble LOPSs.[179] Previous studies suggest that oxygen-containing functional groups on the surface of carbon help retain the high-order polysulfides during operation through the formation of C-S bonds.[174] An analysis of the ratio of the capacity of LOPS formation to that of HOPS reveals a 2.5X increase in the ability of hybrid materials to retain HOPS during discharge at 0.1 C.

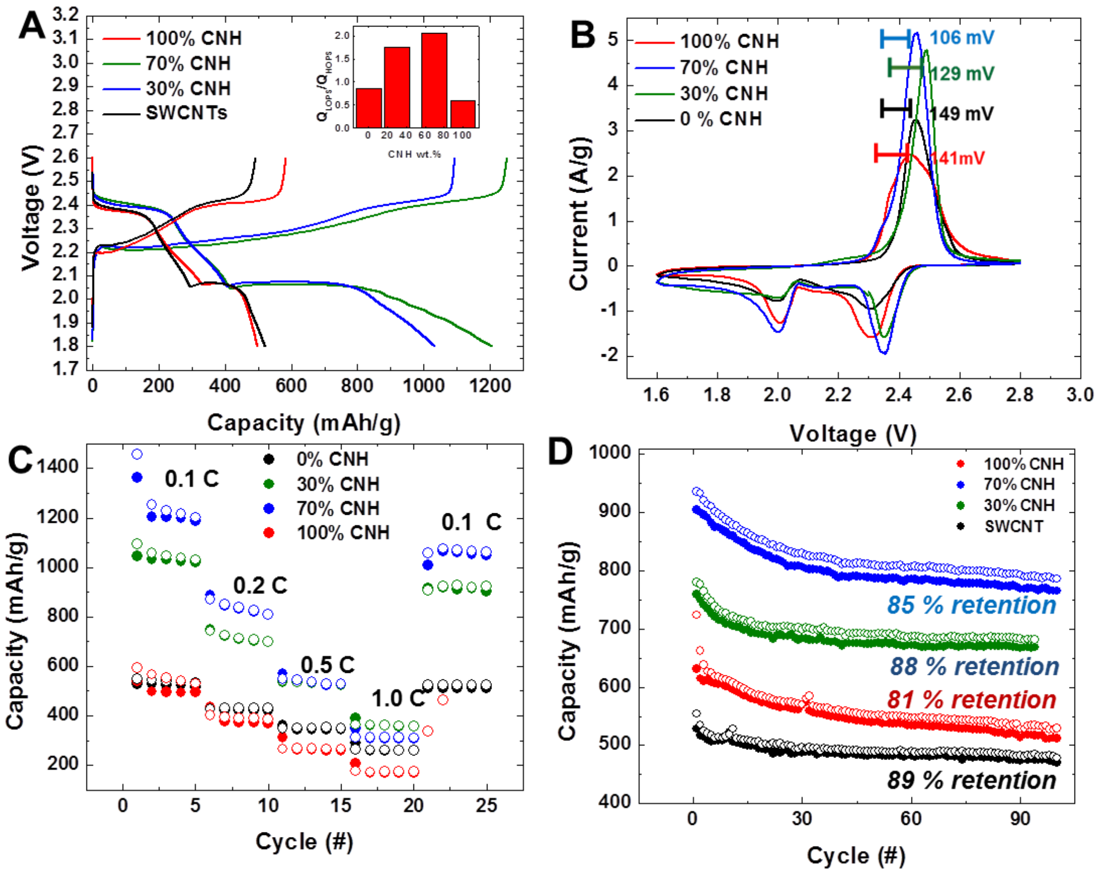

Figure 9.6. (a) Representative charge-discharge curves for each ratio of hybrid material acquired at a rate of 0.1 C. The high voltage plateau at ~2.4 V represents conversion to high order polysulfides and the low voltage plateau at ~2.0 V represents the conversion of HOPS to low order polysulfides (LOPS). (b) Cyclic voltammetry performed on each ratio at a scan rate of 0.1 mV-s emphasizing the difference in peak separations for each material tested. (c) Rate performance of each system studied at the specified rates. The open circles represent capacities obtained during the ‘charge’ cycle and the closed circles represent the capacities obtain during ‘discharge’. (d) Cycling performance at 0.2 C for each of the systems studied.

In addition to improved capacities, the energetics of Li-S reduction are similarly improved through hybridization of the defective and conductive structures. The lower separation between the discharge and charge plateau is evident from the plot in Figure 9.6a and is further quantified using cyclic voltammetry (CV) presented in Figure 9.6b. The voltage splitting between peak currents for 7T3H and 3T7H hybrids during a scan at 0.1 mV-s were 129 mV and 106 mV, respectively, compared to 10H samples with a separation of 141 mV and 10T samples with a separation of 149 mV. The reduced separations in the hybrid films represent improved kinetics of sulfur reduction and a lower barrier to charge-transfer stemming from the presence of oxygen functional groups that bind strongly to the lithium polysulfide species and the presence of conductive SWCNTs that ensure sufficient electrical contact with the current collector. Films comprised solely of SWCNTs lack sufficient oxygen-containing groups in their structure to facilitate effective binding and significant retention of HOPSs formed during charge-discharge while films comprised solely of CNHs lack sufficient structural and electrical integrity to efficiently utilize the high loading of sulfur. SEM analysis in S.I. Fig 4 highlights macroscale interconnectivity of all the films studied at high sulfur loadings. Hybrid films are able to take advantage of both structures with sufficient structural and electrical integrity from the presence of SWCNTs and sufficient anchoring sites from the CNHs.

To further understand the implications of the improved reaction energetics and kinetics on the battery performance, a rate study performed across 4 separate rates was performed for each of the systems studied and is presented in Fig. 4C. At a slow rate of 0.1 C, 3T7H exhibits a reversible capacity of over 1200 mAh/g_{sulfur} compared to 7T3H materials with only ~1000 mAh/g_{sulfur} attributed to the improved retention of HOPSs in the more defective materials. As expected, the single-component materials dramatically underperform their hybrid counterparts with a reversible capacity of 580 and 500 mAh/g_{sulfur} for 10T and 10H films, respectively. At a higher rate of 1.0 C, similar trends in capacity were observed with a reversible capacity of 390 mAh/g for 3T7H samples (33% retention compared to 0.1 C), 310 mAh/g for 7T3H samples (31% retention), 180 mAh/g for 10H (36 % retention) and 280 mAh/g for 10T (56% retention). The poor retention of CNH samples at high rates stems from the poor kinetic behavior of the LOPS reduction from HOPS in which the capacity at the low plateau region degrades more rapidly at higher rates.[179]

Finally, the effect of CNH additives on the cycling stability of composite materials was investigated. The more effective anchoring of HOPSs during discharge results in improved cyclability stemming from the mitigation of active material dissolution during discharge and reduced poisoning of the lithium anode. These beneficial factors manifest in improved cyclability at a rate of 0.2 C, as presented in Fig. 5B. 3T7H samples exhibit a reversible capacity of nearly 800 mAh/g after 100 cycles compared with 7T3H samples that retain only 600 mAh/g and single-component materials with ~500 mAh/g for both 10T and 10H samples. The coulombic efficiencies of all samples maintained over 97 % for the duration of cycling (S.I. Fig. 5). The retention of over 85% of the initial capacity after 100 cycles is the best reported to date for binder-free electrodes with high sulfur loadings. A comparison with the device performance of many sulfur cathodes reported over the last two years is presented in S.I. Fig. 6. From this plot, which charts the total cathode capacity (normalized to the capacity of all cathode components include binders and additives) against the wt.% loading of sulfur illustrates that the devices fabricated herein represent one of most promising electrode architectures reported to date and may be fabricated using a low-cost, scaleable manufacturing approach.

9.6 Conclusion

Hybrid structures of SWCNTs and CNHs were controllably combined using scalable liquid processing techniques to form conductive films of carbon nanomaterials that possessed varying degrees of carbon defects with similar conductivities. By pre-forming the carbon films and using an isothermal sulfur vapor infiltration process, high loadings of over 75 wt. % S were fabricated that preserved the conductivity of the underlying carbon structure. By independently modulating the defect density, the effect of different loadings of CNHs was investigated. Due to the high concentration of oxygen-containing surface groups of the CNH structure, exceptional retention of HOPSs was achieved that resulted in efficient conversion to the solid LOPS reaction products and higher capacities and retention. At a rate of 0.1 C a reversible capacity of over 1,200 mAh/g was achieved for optimized hybrid structures compared to ~600 mAh/g for single-component structures of SWCNTs and CNHs. The retention of over 85% the initial capacity represents one of the best reported sulfur cathodes to date and a comparison with other electrodes reported in literature over the past two years demonstrates the exceptional promise of this novel assembly approach.

CHAPTER 10

Conclusion and Future Outlook

10.1 Conclusion

The chapters contained in this dissertation have emphasized the ability for controlled nanomaterial assembly to engineer the performance of energy storage electrodes. Through the application of EPD, hybrid films of nanomaterials were assembled into electrode-scale films for Li-ion, Li-O, and Li-S batteries that outperformed identical electrode compositions assembled using conventional methods. In this chapter, the major findings of each previous chapter will be summarized in addition to promising research directions inspired by these results.

In chapter 2, the system that enabled controlled EPD assembly was introduced. By achieving individually solubilized structures of carbon nanostructures in NMP, films with homogenously dispersed nanoscale components were fabricated with a composition directly tunable through suspension parameters. Using this system, a mathematical model was developed that describes the accumulation of nanomaterials on a conducting electrode from solution under an applied electric field. By accounting for the unique viscosity effects that stem from concentrated suspensions of high aspect ratio nanomaterials, the unique assembly behavior of SWCNTs that deviated from the traditional EPD model was appropriately described. Applying this model to multi-component solutions of carbon nanomaterials enabled the fabrication of films with a tunable morphology directly related to the suspension and deposition conditions.

In chapter 3, this approach was extended to material systems optimized for the fabrication of lithium-ion battery cathode and anode materials. By fabricating hybrid electrodes comprised of carbon and silicon or MoS_2 nanomaterials, full-cell lithium-ion batteries with superior energy and power capabilities over traditional lithium-ion battery materials were developed. Chapter 3 emphasized the manufacturability of this EPD processing method through the design of a high-throughput, roll-to-roll EPD system capable of fabricating electrodes for a full cell Li-ion battery in less than 30 seconds.

Chapter 4 built upon the notion of EPD for nanomanufacturing by demonstrating a one batch synthesis and assembly process for the layered MoS_2 nanomaterials that comprised the cathode of the full cell battery. Through a combination of liquid-phase exfoliation and EPD, a meaningful mass of purified nanosheets with a controlled size distribution were assembled onto electrodes when starting from inexpensive bulk materials. In chapter 5, the cathode performance of these exfoliated MoS_2 nanosheets was enhanced through the application of a carbon layer that imparted an interfacial strain to the material and enabled improved conversion reaction energetics when operated in a full-cell lithium ion battery with conventional anode materials.

In chapter 6, the utility of the EPD solution processing approach was extended from traditional Li-ion battery materials to next-generation battery systems (i.e. Li-S and Li-O) through a careful design of an all-carbon current collector. By utilizing a controlled hybridization of SWCNTs and graphene materials on metal foam substrates, freestanding all-carbon 3-D structures were fabricated that exhibited robust mechanical properties and exceptional electrical properties characteristic of pristine nanocarbon structures. By comparing this method of EPD hybridization with traditional polymer stabilizing methods, improved conductivity and electrochemical reactivity were observed.

Chapter 7 extended the application of 3-D carbon current collectors to Li-O systems by implementing EPD to controllably interface electrocatalyst nanomaterials with the 3-D carbon network. The films assembled using EPD were demonstrated to have reduced overpotentials during the oxygen reduction and evolution reactions when compared to identical films assembled using the traditional dip-coating approach. The mechanism of enhancement in these films was elucidated through in-situ EIS measurements that emphasized the improved mechanical stability and interconnectivity of EPD films that remained after repeated formation and decomposition of the Li-O discharge product. The comparison with traditional dip-coating coating processes highlighted the important role EPD will play in fully utilizing the properties of future nanoscale catalyst designs.

Finally, the advantage of EPD assembly for Li-S systems was demonstrated in chapter 8 through the invention of a sulfur coating process based on the nanocarbon films of previous chapters. A novel sulfur vapor condensation approach was developed that used the phenomena of capillary condensation to controllably coat the interior of porous carbon electrodes rapidly and at a substantially reduced energy cost compared to the traditional melt-infiltration approach. An analysis of the electrochemical properties of the assembled composite revealed improved charge-transfer between the carbon current collector and sulfur film that improved the energy efficiency upon repeated charging and discharging of the device. Chapter 9 extended these results by using EPD to design all-carbon hybrid electrodes optimized for this novel coating process. By utilizing the assembly developed in chapter 2, a controlled carbon defect density was implemented on a 3-D electrode to engineer the performance of the manufactured carbon-sulfur composite. An optimized ratio of 70% CNH to 30% SWCNT was discovered that resulted in one of the highest cathode utilizations ever reported for Li-S batteries. By combining this sulfur infiltration approach with the R2R battery fabrication process from chapter 3, the promise of large-scale manufacture of these optimized Li-S composites was demonstrated.

Future work using EPD to assemble energy storage electrodes holds exceptional promise. EPD uniquely enables the assembly of nanomaterials with a controllable morphology using scaleable solution processing methods. In order to reduce the cost of film processing using this approach, an adaptation of these techniques from organic solvents to more cost-effective aqueous solutions should be investigated. In order to accomplish this, it is likely that surfactants or polymer functional groups will be required in order to make nanoscale electrode materials miscible in aqueous solvents. Because the presence of these electrochemically inactive polymer additives will hinder the gravimetric energy densities of these composites, research must be done to use the smallest possible quantity of additives to form the aqueous suspensions for EPD.

In regards to next-generation energy storage systems, the fabrication of electrode materials for Li-O cathodes is critical. Extending the results presented in chapter 7 to nanoscale catalysts designed and optimized on the lab scale will be necessary to realize the full commercial impact of newly invented catalyst materials. As work in the realm of nanocatalyst materials has already emphasized, crystalline catalysts exhibit a facet-dependent overpotential for oxygen reduction and evolution that must be optimized by controlling the orientation of the catalyst with respect to the substrate. In this light, electromagnetic properties unique to nanocrystalline materials, such as a tunable dipole moment, should be investigated as mechanisms to enable orientation control when using electric field driven assembly.

In the realm of Li-S batteries, the limitations of the condensation coating process in the context of EPD assembled films should be thoroughly investigated. The critical drawback to current approaches of Li-S cathode design is the focus on optimizing the individual nanostructure with little-to-no regard on how these materials are assembled into a macroscopic films. EPD, however, presents a new parameter to control the morphology of the sulfur coating by engineering the porosity provided by the morphology of the assembled film. This approach enables confinement of the sulfur via both the optimized nanostructure and the junctions between these materials. Due to the mechanism of capillary condensation, junctions between individual nanostructures serve as nucleation points for the sulfur coating enabling confinement from both the nanostructure and the macrostructure of the assembled film. Such a combination permits sulfur loadings beyond what is provided by the nanoscale porosity of individual structures and is crucial in scaling these systems to commercial applications.

I am excited to see the results of any work that builds upon the ideas presented in this thesis. EPD for nanomaterials, and in particular energy storage electrodes, is a very promising field that will increase in relevance as new nanomaterials are introduced and the battery market expands exponentially in the decades to come.

APPENDIX

Performance Parameters of Batteries

A.1 Specific Capacity

In order to assess the quality of battery materials fabricated using EPD, it is important to understand frequently used terms that describe the performance of batteries. In particular, this work will focus on an evaluation of the specific capacity, coulombic efficiency, cycle life, and energy density.

Specific capacity is defined as the amount of charge that may be stored per unit mass of the electrode material. It is a function of the total capacity of both electrodes and is defined mathematically as follows:

$$C_{cell} = \frac{C_{anode}\ x\ C_{cathode}}{C_{anode} + C_{cathode}} \qquad \text{(equation A.1)}$$

Where C_{anode} and $C_{cathode}$ represent the specific capacity of the anode and cathode, respectively. To calculate the specific capacity of either electrode material, the following formula may be used:

$$C = \frac{F\ x\ z}{3.6\ x\ M}\ mAh/g \qquad \text{(equation A.2)}$$

Where *F* is the Faraday constant, *z* the amount of charge transferred per mole of material, and M the molar mass of electrode materials. This value provides an indication for the total amount of electricity that may be stored in a given material.

In order to calculate how efficiently a material stores and releases energy, the Coulombic efficiency of a material is commonly discussed. Coulombic efficiency describes the ratio between the total lithiation capacity obtained during charging compared to the total lithiation capacity obtained during discharge (i.e. charge out vs. charge in). The Coulombic efficiency is the most common metric to gauge the reversibility of an electrode storage reaction and is negatively impacted by parasitic side reactions between electrode materials and the electrolyte. For conventional lithium-ion batteries, Coulombic efficiency is typically over 99%.

A.2 Energy Density

Unlike the capacity term described in the previous section, the energy density of a battery is a direct measurement of the work that may be obtained from an electrochemical cell. This value is a product of the operation voltage and specific capacity of a given system:

$$E = \int V dC \qquad \text{(equation A.3)}$$

Where V represents the operation voltage and dC the capacity at that voltage. When designing an electrochemical system it is important to maximize both the voltage and the capacity of a given pair of anode and cathode materials.

A.3 Thermodynamic Origin of Reaction Voltage

The voltage at which an electrochemical reaction occurs is determined by the thermodynamics of the electrochemical mechanism. For two given electrodes, the voltage measured between them is directly proportional to the difference between their electrochemical potentials – a description of the total energy of electrons in a given state. When electrons flow from one electrode to the other, the energy provided by the cell is equivalent to the energy difference of the electrons in both electrodes. During discharge, the free energy of a system is reduced while charging increases the free energy. The determining factor driving the potential for a given reaction is the difference between the free energy of the products and reactants. The cell potential may be expressed as a function of this free energy change as follows:

$$\Delta G = -nFE_{cell} \quad \text{(equation A.4)}$$

where ΔG represents the change in free energy between the initial and final states of a given reaction.

A.4 The Discharge Curve

The main metric used to measure the potential and capacity of a cell is the discharge curve. The discharge curve presents the cell voltage on the y-axis and the capacity (or total charge) on the x-axis. As current is drawn from the device, material is oxidized at the cathode and reduced at the anode thereby changing the electrochemical potential of both electrodes. Once the potential of the cell reaches the formation potential for a given reaction, the products of that reaction are generated. The total capacity of a chemical reaction is determined by the amount of material converted and may be determined from a discharge curve by measuring the amount of charge transferred at a given potential.

REFERENCES

[1] Kempener, R.; Vivero, G. Renewables and Electricity Storage, **2015**.

[2] Trigg, T.; Tellen, P. Global EV Outlook, **2013**.

[3] Xu, W.; Wang, J.; Ding, F.; Chen, X.; Nasybulin, E.; Zhang, Y.; Zhang, J.-G. Lithium metal anodes for rechargeable batteries, *Energy & Environmental Science* **2014,** 7, (2), 513-537.

[4] Gao, J.; Abruña, H. c. D. Key parameters governing the energy density of rechargeable Li/S batteries, *The Journal of Physical Chemistry Letters* **2014,** 5, (5), 882-885.

[5] Giordani, V.; Tozier, D.; Tan, H.; Burke, C. M.; Gallant, B. M.; Uddin, J.; Greer, J. R.; McCloskey, B. D.; Chase, G. V.; Addison, D. A Molten Salt Lithium–Oxygen Battery, *Journal of the American Chemical Society* **2016,** 138, (8), 2656-2663.

[6] Pashley, R. DLVO and hydration forces between mica surfaces in Li+, Na+, K+, and Cs+ electrolyte solutions: a correlation of double-layer and hydration forces with surface cation exchange properties, *Journal of Colloid and Interface Science* **1981,** 83, (2), 531-546.

[7] Donald, A. M.; Windle, A. H.; Hanna, S., *Liquid Crystalline Polymers*. Cambridge University Press: 2006.

[8] Hughes, J. M.; Aherne, D.; Bergin, S. D.; O'Neill, A.; Streich, P. V.; Hamilton, J. P.; Coleman, J. N. Using solution thermodynamics to describe the dispersion of rod-like solutes: application to dispersions of carbon nanotubes in organic solvents, *Nanotechnology* **2012,** 23, (26), 265604.

[9] Hernandez, Y.; Lotya, M.; Rickard, D.; Bergin, S. D.; Coleman, J. N. Measurement of multicomponent solubility parameters for graphene facilitates solvent discovery, *Langmuir* **2009,** 26, (5), 3208-3213.

[10] Giordani, S.; Bergin, S. D.; Nicolosi, V.; Lebedkin, S.; Kappes, M. M.; Blau, W. J.; Coleman, J. N. Debundling of single-walled nanotubes by dilution: observation of large populations of individual nanotubes in amide solvent dispersions, *The Journal of Physical Chemistry B* **2006,** 110, (32), 15708-15718.

[11] Mohanty, D.; Hockaday, E.; Li, J.; Hensley, D. K.; Daniel, C.; Wood, D. Effect of electrode manufacturing defects on electrochemical performance of lithium-ion batteries: Cognizance of the battery failure sources, *Journal of Power Sources* **2016,** 312, 70-79.

[12] Dickerson, J. H.; Boccaccini, A. R. Electrophoretic Deposition of Nanomaterials, Springer, New York, **2012**.

[13] Cheng, M. D.; Lee, D. W.; Zhao, B.; Hu, H.; Styers-Barnett, D. J.; Puretzky, A. A.; DePaoli, D. W.; Geohegan, D. B.; Ford, E. A.; Angelini, P. Formation studies and controlled production of carbon nanohorns using continuous in situ characterization techniques, *Nanotechnology* **2007,** 18, (18).

[14] Chandrakumar, K. R. S.; Readle, J. D.; Rouleau, C.; Puretzky, A.; Geohegan, D. B.; More, K.; Krishnan, V.; Tian, M. K.; Duscher, G.; Sumpter, B.; Irle, S.; Morokuma, K. High-temperature transformation of Fe-decorated single-wall carbon nanohorns to nanooysters: a combined experimental and theoretical study, *Nanoscale* **2013,** 5, (5), 1849-1857.

[15] Oakes, L.; Westover, A.; Mahjouri-Samani, M.; Chatterjee, S.; Puretzky, A. A.; Rouleau, C.; Geohegan, D. B.; Pint, C. L. Uniform, homogenous coatings of carbon nanohorns on arbitrary substrates from common solvents, *ACS Applied Materials & Interfaces* **2013,** 5, (24), 13153-13160.

[16] Puretzky, A. A.; Styers-Barnett, D. J.; Rouleau, C. M.; Hu, H.; Zhao, B.; Ivanov, I. N.; Geohegan, D. B. Cumulative and continuous laser vaporization synthesis of single wall carbon nanotubes and nanohorns, *Appl Phys a-Mater* **2008,** 93, (4), 849-855.

[17] Chen, Y.; Zhang, X.; Yu, P.; Ma, Y. W. Electrophoretic deposition of graphene nanosheets on nickel foams for electrochemical capacitors, *Journal of Power Sources* **2010,** 195, (9), 3031-3035.

[18] Chen, Z. P.; Ren, W. C.; Gao, L. B.; Liu, B. L.; Pei, S. F.; Cheng, H. M. Three-dimensional flexible and conductive interconnected graphene networks grown by chemical vapour deposition, *Nature Materials* **2011,** 10, (6), 424-428.

[19] Dong, X. C.; Ma, Y. W.; Zhu, G. Y.; Huang, Y. X.; Wang, J.; Chan-Park, M. B.; Wang, L. H.; Huang, W.; Chen, P. Synthesis of graphene-carbon nanotube hybrid foam and its use as a novel three-dimensional electrode for electrochemical sensing, *Journal of Materials Chemistry* **2012,** 22, (33), 17044-17048.

[20] Yavari, F.; Chen, Z. P.; Thomas, A. V.; Ren, W. C.; Cheng, H. M.; Koratkar, N. High Sensitivity Gas Detection Using a Macroscopic Three-Dimensional Graphene Foam Network, *Scientific Reports* **2011,** 1, 166.

[21] De Volder, M.; Tawfick, S. H.; Park, S. J.; Copic, D.; Zhao, Z. Z.; Lu, W.; Hart, A. J. Diverse 3D Microarchitectures Made by Capillary Forming of Carbon Nanotubes, *Advanced Materials* **2010,** 22, (39), 4384-4389.

[22] Zhu, S. Y.; Xu, G. B. Single-walled carbon nanohorns and their applications, *Nanoscale* **2010,** 2, (12), 2538-2549.

[23] Pagona, G.; Mountrichas, G.; Rotas, G.; Karousis, N.; Pispas, S.; Tagmatarchis, N. Properties, applications and functionalisation of carbon nanohorns, *International Journal of Nanotechnology* **2009,** 6, (1-2), 176-195.

[24] Behabtu, N.; Lomeda, J. R.; Green, M. J.; Higginbotham, A. L.; Sinitskii, A.; Kosynkin, D. V.; Tsentalovich, D.; Parra-Vasquez, A. N. G.; Schmidt, J.; Kesselman, E. Spontaneous high-concentration dispersions and liquid crystals of graphene, *Nature Nanotechnology* **2010,** 5, (6), 406-411.

[25] Bergin, S. D.; Sun, Z.; Streich, P.; Hamilton, J.; Coleman, J. N. New solvents for nanotubes: approaching the dispersibility of surfactants, *The Journal of Physical Chemistry C* **2009,** 114, (1), 231-237.

[26] Ausman, K. D.; Piner, R.; Lourie, O.; Ruoff, R. S.; Korobov, M. Organic solvent dispersions of single-walled carbon nanotubes: toward solutions of pristine nanotubes, *The Journal of Physical Chemistry B* **2000,** 104, (38), 8911-8915.

[27] Liu, W. W.; Wang, J. N.; Wang, X. X. Charging of unfunctionalized graphene in organic solvents, *Nanoscale* **2012,** 4, (2), 425-428.

[28] Mueller, S.; Llewellin, E.; Mader, H. In *The Rheology of Suspensions of Solid Particles*, Proceedings of the Royal Society of London A: Mathematical, Physical and Engineering Sciences, 2009; The Royal Society.

[29] Grady, B. P. The Use of Solution Viscosity to Characterize Single-Walled Carbon Nanotube Dispersions, *Macromolecular Chemistry and Physics* **2006,** 207, (23), 2167-2169.

[30] Anné, G.; Neirinck, B.; Vanmeensel, K.; Biest, O.; Vleugels, J. Origin of the potential drop over the deposit during electrophoretic deposition, *Journal of the American Ceramic Society* **2006,** 89, (3), 823-828.

[31] Sarkar, P.; Nicholson, P. S. Electrophoretic Deposition (EPD): Mechanisms, Kinetics, and Application to Ceramics, *Journal of the American Ceramic Society* **1996,** 79, (8), 1987-2002.

[32] Shaffer, M. S.; Fan, X.; Windle, A. Dispersion and packing of carbon nanotubes, *Carbon* **1998,** 36, (11), 1603-1612.

[33] Halelfadl, S.; Estellé, P.; Aladag, B.; Doner, N.; Maré, T. Viscosity of carbon nanotubes water-based nanofluids: Influence of concentration and temperature, *International Journal of Thermal Sciences* **2013,** 71, 111-117.

[34] Huang, Y. Y.; Terentjev, E. M. Dispersion of carbon nanotubes: mixing, sonication, stabilization, and composite properties, *Polymers* **2012,** 4, (1), 275-295.

[35] Brown, P.; Kamat, P. V. Quantum Dot Solar Cells. Electrophoretic Deposition of CdSe−C60 Composite Films and Capture of Photogenerated Electrons with n C60 Cluster Shell, *Journal of the American Ceramic Society* **2008,** 130, (28), 8890-8891.

[36] Cho, J.; Konopka, K.; Rozniatowski, K.; Garcia-Lecina, E.; Shaffer, M. S. P.; Boccaccini, A. R. Characterisation of carbon nanotube films deposited by electrophoretic deposition, *Carbon* **2009,** 47, (1), 58-67.

[37] Zhou, L. J.; Hou, Z. F.; Wu, L. M. First-Principles Study of Lithium Adsorption and Diffusion on Graphene with Point Defects, *Journal of Physical Chemistry C* **2012,** 116, (41), 21780-21787.

[38] Chan, C. K.; Peng, H. L.; Liu, G.; McIlwrath, K.; Zhang, X. F.; Huggins, R. A.; Cui, Y. High-performance lithium battery anodes using silicon nanowires, *Nature Nanotechnology* **2008,** 3, (1), 31-35.

[39] Yao, Y.; McDowell, M. T.; Ryu, I.; Wu, H.; Liu, N. A.; Hu, L. B.; Nix, W. D.; Cui, Y. Interconnected Silicon Hollow Nanospheres for Lithium-Ion Battery Anodes with Long Cycle Life, *Nano Letters* **2011,** 11, (7), 2949-2954.

[40] Cui, L. F.; Yang, Y.; Hsu, C. M.; Cui, Y. Carbon-Silicon Core-Shell Nanowires as High Capacity Electrode for Lithium Ion Batteries, *Nano Letters* **2009,** 9, (9), 3370-3374.

[41] Goodenough, J. B.; Park, K. S. The Li-ion Rechargeable Battery: A Perspective, *Journal of the American Chemical Society* **2013,** 135, (4), 1167-1176.

[42] Carter, R.; Oakes, L.; Cohn, A. P.; Holzgrafe, J.; Zarick, H. F.; Chatterjee, S.; Bardhan, R.; Pint, C. L. Solution Assembled Single-Walled Carbon Nanotube Foams: Superior Performance in Supercapacitors, Lithium-Ion, and Lithium–Air Batteries, *The Journal of Physical Chemistry C* **2014,** 118, (35), 20137-20151.

[43] Ng, S. H.; Wang, J. Z.; Wexler, D.; Konstantinov, K.; Guo, Z. P.; Liu, H. K. Highly reversible lithium storage in spheroidal carbon-coated silicon nanocomposites as anodes for lithium-ion batteries, *Angewandte Chemie-International Edition* **2006,** 45, (41), 6896-6899.

[44] Gao, B.; Yue, G. Z.; Qiu, Q.; Cheng, Y.; Shimoda, H.; Fleming, L.; Zhou, O. Fabrication and electron field emission properties of carbon nanotube films by electrophoretic deposition, *Advanced Materials* **2001,** 13, (23), 1770-1773.

[45] Tarascon, J. M.; Armand, M. Issues and challenges facing rechargeable lithium batteries, *Nature* **2001,** 414, (6861), 359-367.

[46] Xu, K. Nonaqueous liquid electrolytes for lithium-based rechargeable batteries, *Chemical Reviews* **2004,** 104, (10), 4303-4417.

[47] Liu, N. A.; Hu, L. B.; McDowell, M. T.; Jackson, A.; Cui, Y. Prelithiated Silicon Nanowires as an Anode for Lithium Ion Batteries, *ACS Nano* **2011,** 5, (8), 6487-6493.

[48] Stephenson, T.; Li, Z.; Olsen, B.; Mitlin, D. Lithium ion battery applications of molybdenum disulfide (MoS 2) nanocomposites, *Energy & Environmental Science* **2014,** 7, (1), 209-231.

[49] Share, K.; Lewis, J.; Oakes, L.; Carter, R. E.; Cohn, A. P.; Pint, C. L. Tungsten diselenide (WSe2) as a high capacity, low overpotential conversion electrode for sodium ion batteries, *RSC Advances* **2015,** 5, (123), 101262-101267.

[50] Lee, Y.-H.; Yu, L.; Wang, H.; Fang, W.; Ling, X.; Shi, Y.; Lin, C.-T.; Huang, J.-K.; Chang, M.-T.; Chang, C.-S. Synthesis and transfer of single-layer transition metal disulfides on diverse surfaces, *Nano Letters* **2013,** 13, (4), 1852-1857.

[51] Liu, N.; Kim, P.; Kim, J. H.; Ye, J. H.; Kim, S.; Lee, C. J. Large-Area Atomically Thin MoS2 Nanosheets Prepared Using Electrochemical Exfoliation, *ACS nano* **2014,** 8, (7), 6902-6910.

[52] Cunningham, G.; Lotya, M.; Cucinotta, C. S.; Sanvito, S.; Bergin, S. D.; Menzel, R.; Shaffer, M. S.; Coleman, J. N. Solvent exfoliation of transition metal dichalcogenides: dispersibility of exfoliated nanosheets varies only weakly between compounds, *ACS Nano* **2012,** 6, (4), 3468-3480.

[53] Coleman, J. N.; Lotya, M.; O'Neill, A.; Bergin, S. D.; King, P. J.; Khan, U.; Young, K.; Gaucher, A.; De, S.; Smith, R. J. Two-dimensional nanosheets produced by liquid exfoliation of layered materials, *Science* **2011,** 331, (6017), 568-571.

[54] Park, S.; Ruoff, R. S. Chemical methods for the production of graphenes, *Nature Nanotechnology* **2009,** 4, (4), 217-224.

[55] Zeng, Z.; Yin, Z.; Huang, X.; Li, H.; He, Q.; Lu, G.; Boey, F.; Zhang, H. Single-Layer Semiconducting Nanosheets: High-Yield Preparation and Device Fabrication, *Angewandte Chemie International Edition* **2011,** 50, (47), 11093-11097.

[56] Halim, U.; Zheng, C. R.; Chen, Y.; Lin, Z.; Jiang, S.; Cheng, R.; Huang, Y.; Duan, X. A rational design of cosolvent exfoliation of layered materials by directly probing liquid–solid interaction, *Nature Communications* **2013,** 4.

[57] Smith, R. J.; King, P. J.; Lotya, M.; Wirtz, C.; Khan, U.; De, S.; O'Neill, A.; Duesberg, G. S.; Grunlan, J. C.; Moriarty, G. Large-Scale Exfoliation of Inorganic Layered Compounds in Aqueous Surfactant Solutions, *Advanced Materials* **2011,** 23, (34), 3944-3948.

[58] Cohn, A. P.; Oakes, L.; Carter, R.; Chatterjee, S.; Westover, A. S.; Share, K.; Pint, C. L. Assessing the improved performance of freestanding, flexible graphene and carbon nanotube hybrid foams for lithium ion battery anodes, *Nanoscale* **2014,** 6, (9), 4669-4675.

[59] Dickerson, J. H.; Boccaccini, A. R., *Electrophoretic Deposition of Nanomaterials*. Springer: 2012; Vol. 50.

[60] Nguyen, E. P.; Carey, B.; Daeneke, T.; Ou, J. Z.; Latham, K.; Zhuiykov, S.; Kalantar-Zadeh, K. Investigation of two-solvent grinding assisted liquid phase exfoliation of layered MoS_2, *Chemistry of Materials* **2014**.

[61] Sugimoto, W.; Terabayashi, O.; Murakami, Y.; Takasu, Y. Electrophoretic deposition of negatively charged tetratitanate nanosheets and transformation into preferentially oriented TiO_2 (B) film, *Journal of Materials Chemistry* **2002,** 12, (12), 3814-3818.

[62] Zhu, Z.; Cheng, Y.; Schwingenschlögl, U. Giant spin-orbit-induced spin splitting in two-dimensional transition-metal dichalcogenide semiconductors, *Physical Review B* **2011,** 84, (15), 153402.

[63] Jariwala, D.; Sangwan, V. K.; Lauhon, L. J.; Marks, T. J.; Hersam, M. C. Emerging device applications for semiconducting two-dimensional transition metal dichalcogenides, *ACS Nano* **2014,** 8, (2), 1102-1120.

[64] Lotya, M.; Rakovich, A.; Donegan, J. F.; Coleman, J. N. Measuring the lateral size of liquid-exfoliated nanosheets with dynamic light scattering, *Nanotechnology* **2013,** 24, (26), 265703.

[65] Devlin, M. T.; Barany, G.; Levin, I. W. Conformational properties of asymmetrically substituted mono-, di-and trisulfides: solid and liquid phase Raman spectra, *Journal of Molecular Structure* **1990,** 238, 119-137.

[66] Han, S. P.; Yang, S.-M. Orientation distribution and electrophoretic motions of rod-like particles in a capillary, *Journal of Colloid and Interface Science* **1996,** 177, (1), 132-142.

[67] Muscuso, L.; Cravanzola, S.; Cesano, F.; Scarano, D.; Zecchina, A. Optical, Vibrational and Structural Properties of MoS_2 Nanoparticles Obtained by Exfoliation and Fragmentation via Ultrasound Cavitation in Isopropyl Alcohol, *The Journal of Physical Chemistry C* **2015** 119, 7, 3791-3801.

[68] Liang, X.; Hart, C.; Pang, Q.; Garsuch, A.; Weiss, T.; Nazar, L. F. A highly efficient polysulfide mediator for lithium–sulfur batteries, *Nature Communications* **2015,** 6, 5682

[69] Georgiou, T.; Jalil, R.; Belle, B. D.; Britnell, L.; Gorbachev, R. V.; Morozov, S. V.; Kim, Y.-J.; Gholinia, A.; Haigh, S. J.; Makarovsky, O. Vertical field-effect transistor based on graphene-WS2 heterostructures for flexible and transparent electronics, *Nature Nanotechnology* **2013,** 8, (2), 100-103.

[70] He, J.; Kumar, N.; Bellus, M. Z.; Chiu, H.-Y.; He, D.; Wang, Y.; Zhao, H. Electron transfer and coupling in graphene–tungsten disulfide van der Waals heterostructures, *Nature Communications* **2014,** 5, 5622.

[71] Roy, K.; Padmanabhan, M.; Goswami, S.; Sai, T. P.; Ramalingam, G.; Raghavan, S.; Ghosh, A. Graphene-MoS2 hybrid structures for multifunctional photoresponsive memory devices, *Nature Nanotechnology* **2013,** 8, (11), 826-830.

[72] Castellanos-Gomez, A.; Roldán, R.; Cappelluti, E.; Buscema, M.; Guinea, F.; van der Zant, H. S.; Steele, G. A. Local strain engineering in atomically thin MoS_2, *Nano Letters* **2013,** 13, (11), 5361-5366.

[73] He, K.; Poole, C.; Mak, K. F.; Shan, J. Experimental demonstration of continuous electronic structure tuning via strain in atomically thin MoS2, *Nano Letters* **2013,** 13, (6), 2931-2936.

[74] Liu, Z.; Amani, M.; Najmaei, S.; Xu, Q.; Zou, X. L.; Zhou, W.; Yu, T.; Qiu, C. Y.; Birdwell, A. G.; Crowne, F. J.; Vajtai, R.; Yakobson, B. I.; Xia, Z. H.; Dubey, M.; Ajayan, P. M.; Lou, J. Strain and structure heterogeneity in MoS2 atomic layers grown by chemical vapour deposition, *Nature Communications* **2014,** 5, 5246.

[75] Feng, J.; Qian, X.; Huang, C.-W.; Li, J. Strain-engineered artificial atom as a broad-spectrum solar energy funnel, *Nature Photonics* **2012,** 6, (12), 866-872.

[76] Shen, J.; He, Y.; Wu, J.; Gao, C.; Keyshar, K.; Zhang, X.; Yang, Y.; Ye, M.; Vajtai, R.; Lou, J. Liquid Phase Exfoliation of Two-Dimensional Materials by Directly Probing and Matching Surface Tension Components, *Nano Letters* **2015,** 15, (8), 5449-5454.

[77] Nicolosi, V.; Chhowalla, M.; Kanatzidis, M. G.; Strano, M. S.; Coleman, J. N. Liquid exfoliation of layered materials, *Science* **2013,** 340, (6139), 1226419.

[78] Du, M.; Cui, L.; Cao, Y.; Bard, A. J. Mechanoelectrochemical Catalysis of the Effect of Elastic Strain on a Platinum nanofilm for the ORR Exerted by a Shape Memory Alloy Substrate, *Journal of the American Chemical Society* **2015,** 137, (23), 7397-7403.

[79] Conley, H. J.; Wang, B.; Ziegler, J. I.; Haglund Jr, R. F.; Pantelides, S. T.; Bolotin, K. I. Bandgap engineering of strained monolayer and bilayer MoS2, *Nano Letters* **2013,** 13, (8), 3626-3630.

[80] Hui, Y. Y.; Liu, X.; Jie, W.; Chan, N. Y.; Hao, J.; Hsu, Y.-T.; Li, L.-J.; Guo, W.; Lau, S. P. Exceptional tunability of band energy in a compressively strained trilayer MoS2 sheet, *ACS Nano* **2013,** 7, (8), 7126-7131.

[81] Rice, C.; Young, R.; Zan, R.; Bangert, U.; Wolverson, D.; Georgiou, T.; Jalil, R.; Novoselov, K. Raman-scattering measurements and first-principles calculations of strain-induced phonon shifts in monolayer MoS2, *Physical Review B* **2013,** 87, (8), 081307.

[82] Lanzillo, N. A.; Birdwell, A. G.; Amani, M.; Crowne, F. J.; Shah, P. B.; Najmaei, S.; Liu, Z.; Ajayan, P. M.; Lou, J.; Dubey, M. Temperature-dependent phonon shifts in monolayer MoS2, *Applied Physics Letters* **2013,** 103, (9), 093102.

[83] Yeon, J.-T.; Jang, J.-Y.; Han, J.-G.; Cho, J.; Lee, K. T.; Choi, N.-S. Raman spectroscopic and X-ray diffraction studies of sulfur composite electrodes during discharge and charge, *Journal of The Electrochemical Society* **2012,** 159, (8), A1308-A1314.

[84] Sun, Z. Z.; Pint, C. L.; Marcano, D. C.; Zhang, C. G.; Yao, J.; Ruan, G. D.; Yan, Z.; Zhu, Y.; Hauge, R. H.; Tour, J. M. Towards hybrid superlattices in graphene, *Nature Communications* **2011,** 2.

[85] Xue, Y. H.; Yu, D. S.; Dai, L. M.; Wang, R. G.; Li, D. Q.; Roy, A.; Lu, F.; Chen, H.; Liu, Y.; Qu, J. Three-dimensional B,N-doped graphene foam as a metal-free catalyst for oxygen reduction reaction, *Physical Chemistry Chemistry Physics* **2013,** 15, (29), 12220-12226.

[86] Bolotin, K. I.; Sikes, K. J.; Jiang, Z.; Klima, M.; Fudenberg, G.; Hone, J.; Kim, P.; Stormer, H. L. Ultrahigh electron mobility in suspended graphene, *Solid State Communications* **2008,** 146, (9-10), 351-355.

[87] Lin, Y. C.; Lu, C. C.; Yeh, C. H.; Jin, C. H.; Suenaga, K.; Chiu, P. W. Graphene Annealing: How Clean Can It Be?, *Nano Letters* **2012,** 12, (1), 414-419.

[88] Pirkle, A.; Chan, J.; Venugopal, A.; Hinojos, D.; Magnuson, C. W.; McDonnell, S.; Colombo, L.; Vogel, E. M.; Ruoff, R. S.; Wallace, R. M. The effect of chemical residues on the physical and electrical properties of chemical vapor deposited graphene transferred to SiO2, *Appl Physical Letters* **2011,** 99, (12), 122108.

[89] Van der Biest, O. O.; Vandeperre, L. J. Electrophoretic deposition of materials, *Annual Reviews of Materials Science* **1999,** 29, 327-352.

[90] Maciel, I. O.; Anderson, N.; Pimenta, M. A.; Hartschuh, A.; Qian, H. H.; Terrones, M.; Terrones, H.; Campos-Delgado, J.; Rao, A. M.; Novotny, L.; Jorio, A. Electron and phonon renormalization near charged defects in carbon nanotubes, *Nature Materials* **2008,** 7, (11), 878-883.

[91] Girishkumar, G.; McCloskey, B.; Luntz, A.; Swanson, S.; Wilcke, W. Lithium− air battery: promise and challenges, *The Journal of Physical Chemistry Letters* **2010,** 1, (14), 2193-2203.

[92] Abraham, K.; Jiang, Z. A polymer electrolyte-based rechargeable lithium/oxygen battery, *Journal of The Electrochemical Society* **1996,** 143, (1), 1-5.

[93] Bruce, P. G.; Freunberger, S. A.; Hardwick, L. J.; Tarascon, J.-M. Li-O2 and Li-S batteries with high energy storage, *Nature Materials* **2012,** 11, (1), 19-29.

[94] Cheng, F.; Chen, J. Metal–air batteries: from oxygen reduction electrochemistry to cathode catalysts, *Chemical Society Reviews* **2012,** 41, (6), 2172-2192.

[95] Song, M.-K.; Park, S.; Alamgir, F. M.; Cho, J.; Liu, M. Nanostructured electrodes for lithium-ion and lithium-air batteries: the latest developments, challenges, and perspectives, *Materials Science and Engineering: Reports* **2011,** 72, (11), 203-252.

[96] Guo, Y.-G.; Hu, J.-S.; Wan, L.-J. Nanostructured materials for electrochemical energy conversion and storage devices, *Advanced Materials* **2008,** 20, (15), 2878-2887.

[97] Arico, A. S.; Bruce, P.; Scrosati, B.; Tarascon, J.-M.; Van Schalkwijk, W. Nanostructured materials for advanced energy conversion and storage devices, *Nature Materials* **2005,** 4, (5), 366-377.

[98] Manthiram, A.; Murugan, A. V.; Sarkar, A.; Muraliganth, T. Nanostructured electrode materials for electrochemical energy storage and conversion, *Energy & Environmental Science* **2008,** 1, (6), 621-638.

[99] Chang, Z. w.; Xu, J. j.; Liu, Q. c.; Li, L.; Zhang, X. b. Recent Progress on Stability Enhancement for Cathode in Rechargeable Non-Aqueous Lithium-Oxygen Battery, *Advanced Energy Materials* **2015,** 3, 34-48

[100] Kim, B. G.; Kim, H.-J.; Back, S.; Nam, K. W.; Jung, Y.; Han, Y.-K.; Choi, J. W. Improved reversibility in lithium-oxygen battery: Understanding elementary reactions and surface charge engineering of metal alloy catalyst, *Scientific Reports* **2014,** 4, 4225

[101] Kushima, A.; Koido, T.; Fujiwara, Y.; Kuriyama, N.; Kusumi, N.; Li, J. Charging/Discharging Nano-Morphology Asymmetry and Rate-Dependent Capacity Degradation in Li-Oxygen Battery, *Nano Letters* **2015**, 15, (12), 8260-8265.

[102] Andersen, C. P.; Hu, H.; Qiu, G.; Kalra, V.; Sun, Y. Pore-Scale Transport Resolved Model Incorporating Cathode Microstructure and Peroxide Growth in Lithium-Air Batteries, *Journal of The Electrochemical Society* **2015,** 162, (7), A1135-A1145.

[103] Liu, T.; Leskes, M.; Yu, W.; Moore, A. J.; Zhou, L.; Bayley, P. M.; Kim, G.; Grey, C. P. Cycling Li-O_2 batteries via LiOH formation and decomposition, *Science* **2015,** 350, (6260), 530-533.

[104] Yang, S.; Song, H.; Chen, X. Electrochemical performance of expanded mesocarbon microbeads as anode material for lithium-ion batteries, *Electrochemistry Communications* **2006,** 8, (1), 137-142.

[105] Gyenes, B.; Stevens, D.; Chevrier, V.; Dahn, J. Understanding Anomalous Behavior in Coulombic Efficiency Measurements on Li-ion Batteries, *Journal of The Electrochemical Society* **2015,** 162, (3), A278-A283.

[106] Hong, W. T.; Risch, M.; Stoerzinger, K. A.; Grimaud, A.; Suntivich, J.; Shao-Horn, Y. Toward the rational design of non-precious transition metal oxides for oxygen electrocatalysis, *Energy & Environmental Science* **2015,** 8, (5), 1404-1427.

[107] Sun, B.; Huang, X.; Chen, S.; Munroe, P.; Wang, G. Porous Graphene Nanoarchitectures: An Efficient Catalyst for Low Charge-Overpotential, Long Life, and High Capacity Lithium–Oxygen Batteries, *Nano Letters* **2014,** 14, (6), 3145-3152.

[108] Ma, S.; Wu, Y.; Wang, J.; Zhang, Y.; Zhang, Y.; Yan, X.; Wei, Y.; Liu, P.; Wang, J.; Jiang, K. On the Reversibility of Noble Metal-Catalyzed Aprotic Li-O_2 Batteries, *Nano Letters* **2015**, 15, (12), 8084-8090.

[109] Ren, X.; Wang, B.; Zhu, J.; Liu, J.; Zhang, W.; Wen, Z. The doping effect on the catalytic activity of graphene for oxygen evolution reaction in a lithium–air battery: a first-principles study, *Physical Chemistry Chemical Physics* **2015,** 17, (22), 14605-14612.

[110] Wang, Z.-L.; Xu, D.; Xu, J.-J.; Zhang, X.-B. Oxygen electrocatalysts in metal–air batteries: from aqueous to nonaqueous electrolytes, *Chemical Society Reviews* **2014,** 43, (22), 7746-7786.

[111] Meng, Y.; Song, W.; Huang, H.; Ren, Z.; Chen, S.-Y.; Suib, S. L. Structure–property relationship of bifunctional MnO_2 nanostructures: highly efficient, ultra-stable electrochemical water oxidation and oxygen reduction reaction catalysts identified in alkaline media, *Journal of the American Chemical Society* **2014,** 136, (32), 11452-11464.

[112] Sun, C.; Li, F.; Ma, C.; Wang, Y.; Ren, Y.; Yang, W.; Ma, Z.; Li, J.; Chen, Y.; Kim, Y. Graphene–Co_3O_4 nanocomposite as an efficient bifunctional catalyst for lithium–air batteries, *Journal of Materials Chemistry A* **2014,** 2, (20), 7188-7196.

[113] Maiyalagan, T.; Jarvis, K. A.; Therese, S.; Ferreira, P. J.; Manthiram, A. Spinel-type lithium cobalt oxide as a bifunctional electrocatalyst for the oxygen evolution and oxygen reduction reactions, *Nature Communications* **2014,** 5, 3949.

[114] Man, I. C.; Su, H. Y.; Calle-Vallejo, F.; Hansen, H. A.; Martínez, J. I.; Inoglu, N. G.; Kitchin, J.; Jaramillo, T. F.; Nørskov, J. K.; Rossmeisl, J. Universality in oxygen evolution electrocatalysis on oxide surfaces, *ChemCatChem* **2011,** 3, (7), 1159-1165.

[115] Black, R.; Lee, J. H.; Adams, B.; Mims, C. A.; Nazar, L. F. The role of catalysts and peroxide oxidation in lithium–oxygen batteries, *Angewandte Chemie* **2013,** 125, (1), 410-414.

[116] Cheng, F.; Su, Y.; Liang, J.; Tao, Z.; Chen, J. MnO2-Based Nanostructures as Catalysts for Electrochemical Oxygen Reduction in Alkaline Media, *Chemistry of Materials* **2009,** 22, (3), 898-905.

[117] Zhang, J.; Liu, J.; Peng, Q.; Wang, X.; Li, Y. Nearly monodisperse Cu_2O and CuO nanospheres: preparation and applications for sensitive gas sensors, *Chemistry of Materials* **2006,** 18, (4), 867-871.

[118] Seo, M.-H.; Yuasa, M.; Kida, T.; Huh, J.-S.; Shimanoe, K.; Yamazoe, N. Gas sensing characteristics and porosity control of nanostructured films composed of TiO_2 nanotubes, *Sensors and Actuators B: Chemical* **2009,** 137, (2), 513-520.

[119] Jiang, S. P. Nanoscale and nano-structured electrodes of solid oxide fuel cells by infiltration: advances and challenges, *International Journal of Hydrogen Energy* **2012,** 37, (1), 449-470.

[120] Boccaccini, A.; Schindler, U.; Krüger, H.-G. Ceramic coatings on carbon and metallic fibres by electrophoretic deposition, *Materials Letters* **2001,** 51, (3), 225-230.

[121] Teranishi, T.; Hosoe, M.; Tanaka, T.; Miyake, M. Size control of monodispersed Pt nanoparticles and their 2D organization by electrophoretic deposition, *The Journal of Physical Chemistry B* **1999,** 103, (19), 3818-3827.

[122] Shao, Y.; Yin, G.; Gao, Y. Understanding and approaches for the durability issues of Pt-based catalysts for PEM fuel cell, *Journal of Power Sources* **2007,** 171, (2), 558-566.

[123] Krejci, A. J.; Gonzalo-Juan, I.; Dickerson, J. H. Evolution of ordering in iron oxide nanoparticle monolayers using electrophoretic deposition, *ACS Applied Materials & Interfaces* **2011,** 3, (9), 3611-3615.

[124] Krejci, A. J.; Mandal, J.; Dickerson, J. H. Patterned substrates to facilitate long-range ordering in the formation of nanoparticle monolayers by electrophoretic deposition, *Applied Physics Letters* **2012,** 101, (4), 043117.

[125] Trau, M.; Saville, D.; Aksay, I. Field-induced layering of colloidal crystals, *Science* **1996,** 272, (5262), 706-709.

[126] Zhitomirsky, I. Cathodic electrodeposition of ceramic and organoceramic materials. Fundamental aspects, *Advances in Colloid and Interface Science* **2002,** 97, (1), 279-317.

[127] Zhitomirsky, I.; Gal-Or, L. Electrophoretic deposition of hydroxyapatite, *Journal of Materials Science: Materials in Medicine* **1997,** 8, (4), 213-219.

[128] Oakes, L.; Cohn, A. P.; Westover, A. S.; Pint, C. L. Electrophoretic stabilization of freestanding pristine graphene foams with carbon nanotubes for enhanced optical and electrical response, *Materials Letters* **2015,** 159, 261-264.

[129] Lee, D. U.; Choi, J. Y.; Feng, K.; Park, H. W.; Chen, Z. Advanced Extremely Durable 3D Bifunctional Air Electrodes for Rechargeable Zinc-Air Batteries, *Advanced Energy Materials* **2014,** 4, (6), 1301389

[130] Salehi, M.; Shariatinia, Z. An optimization of MnO2 amount in CNT-MnO2 nanocomposite as a high rate cathode catalyst for the rechargeable Li-O2 batteries, *Electrochimica Acta* **2015**, 188, 428-440.

[131] Mirzaeian, M.; Hall, P. J. Characterizing capacity loss of lithium oxygen batteries by impedance spectroscopy, *Journal of Power Sources* **2010,** 195, (19), 6817-6824.

[132] Choi, Y.-M.; Pyun, S.-I.; Bae, J.-S.; Moon, S.-I. Effects of lithium content on the electrochemical lithium intercalation reaction into LiNiO 2 and LiCoO 2 electrodes, *Journal of Power Sources* **1995,** 56, (1), 25-30.

[133] Zhang, G.; Zheng, J.; Liang, R.; Zhang, C.; Wang, B.; Hendrickson, M.; Plichta, E. Lithium–air batteries using SWNT/CNF buckypapers as air electrodes, *Journal of The Electrochemical Society* **2010,** 157, (8), A953-A956.

[134] Adams, J.; Karulkar, M.; Anandan, V. Evaluation and electrochemical analyses of cathodes for lithium-air batteries, *Journal of Power Sources* **2013,** 239, 132-143.

[135] Radin, M. D.; Rodriguez, J. F.; Tian, F.; Siegel, D. J. Lithium peroxide surfaces are metallic, while lithium oxide surfaces are not, *Journal of the American Chemical Society* **2011,** 134, (2), 1093-1103.

[136] Elia, G. A.; Park, J.-B.; Scrosati, B.; Sun, Y.-K.; Hassoun, J. Investigation of the carbon electrode changes during lithium oxygen cell operation in a tetraglyme-based electrolyte, *Electrochemistry Communications* **2013,** 34, 250-253.

[137] Choi, N. S.; Chen, Z.; Freunberger, S. A.; Ji, X.; Sun, Y. K.; Amine, K.; Yushin, G.; Nazar, L. F.; Cho, J.; Bruce, P. G. Challenges Facing Lithium Batteries and Electrical Double-Layer Capacitors, *Angewandte Chemie International Edition* **2012,** 51, (40), 9994-10024.

[138] Yin, Y. X.; Xin, S.; Guo, Y. G.; Wan, L. J. Lithium–sulfur batteries: Electrochemistry, materials, and prospects, *Angewandte Chemie International Edition* **2013,** 52, (50), 13186-13200.

[139] Ji, X.; Lee, K. T.; Nazar, L. F. A highly ordered nanostructured carbon–sulphur cathode for lithium–sulphur batteries, *Nature Materials* **2009,** 8, (6), 500-506.

[140] Wild, M.; O'Neill, L.; Zhang, T.; Purkayastha, R.; Minton, G.; Marinescu, M.; Offer, G. Lithium sulfur batteries, a mechanistic review, *Energy & Environmental Science* **2015,** 8, (12), 3477-3494.

[141] Li, D.; Han, F.; Wang, S.; Cheng, F.; Sun, Q.; Li, W.-C. High sulfur loading cathodes fabricated using peapodlike, large pore volume mesoporous carbon for lithium–sulfur battery, *ACS Applied Materials & Interfaces* **2013,** 5, (6), 2208-2213.

[142] Sahore, R.; Levin, B. D.; Pan, M.; Muller, D. A.; DiSalvo, F. J.; Giannelis, E. P. Design Principles for Optimum Performance of Porous Carbons in Lithium–Sulfur Batteries, *Advanced Energy Materials* **2016**, 6, 1600134.

[143] Du, W.-C.; Yin, Y.-X.; Zeng, X.-X.; Shi, J.-L.; Zhang, S.-F.; Wan, L.-J.; Guo, Y.-G. Wet Chemistry Synthesis of Multidimensional Nanocarbon–Sulfur Hybrid Materials with Ultrahigh Sulfur Loading for Lithium–Sulfur Batteries, *ACS Applied Materials & Interfaces* **2015**.

[144] Yang, Y.; Zheng, G.; Cui, Y. Nanostructured sulfur cathodes, *Chemical Society Reviews* **2013,** 42, (7), 3018-3032.

[145] Manthiram, A.; Fu, Y.; Chung, S.-H.; Zu, C.; Su, Y.-S. Rechargeable lithium–sulfur batteries, *Chemical Reviews* **2014,** 114, (23), 11751-11787.

[146] Lacey, M. J.; Jeschull, F.; Edström, K.; Brandell, D. Functional, water-soluble binders for improved capacity and stability of lithium–sulfur batteries, *Journal of Power Sources* **2014,** 264, 8-14.

[147] Borchardt, L.; Oschatz, M.; Kaskel, S. Carbon Materials for Lithium Sulfur Batteries—Ten Critical Questions, *Chemistry–A European Journal* **2016,** 22, (22), 7324-7351.

[148] Urbonaite, S.; Poux, T.; Novák, P. Progress towards commercially viable Li–S battery cells, *Advanced Energy Materials* **2015,** 5, 1500118.

[149] Hagen, M.; Hanselmann, D.; Ahlbrecht, K.; Maça, R.; Gerber, D.; Tübke, J. Lithium–Sulfur Cells: The Gap between the State-of-the-Art and the Requirements for High Energy Battery Cells, *Advanced Energy Materials* **2015,** 5, (16).

[150] Borchardt, L.; Oschatz, M.; Kaskel, S. Carbon Materials for Lithium Sulfur Batteries—Ten Critical Questions, *Chemistry–A European Journal* **2016**.

[151] Hagen, M.; Hanselmann, D.; Ahlbrecht, K.; Maca, R.; Gerber, D.; Tubke, J. Lithium-Sulfur Cells: The Gap between the State-of-the-Art and the Requirements for High Energy Battery Cells, *Advanced Energy Materials* **2015,** 5, 1401986.

[152] Cheng, X. B.; Huang, J. Q.; Zhang, Q.; Peng, H. J.; Zhao, M. Q.; Wei, F. Aligned carbon nanotube/sulfur composite cathodes with high sulfur content for lithium-sulfur batteries, *Nano Energy* **2014,** 4, 65-72.

[153] Du, W. C.; Yin, Y. X.; Zeng, X. X.; Shi, J. L.; Zhang, S. F.; Wan, L. J.; Guo, Y. G. Wet Chemistry Synthesis of Multidimensional Nanocarbon-Sulfur Hybrid Materials with Ultrahigh Sulfur Loading for Lithium-Sulfur Batteries, *ACS Applied Materials and Interfaces* **2016,** 8, (6), 3584-3590.

[154] Helen, M.; Reddy, M. A.; Diemant, T.; Golla-Schindler, U.; Behm, R. J.; Kaiser, U.; Fichtner, M. Single step transformation of sulphur to Li2S2/Li2S in Li-S batteries, *Scientific Reports* **2015,** 5, 12146.

[155] Xin, S.; Gu, L.; Zhao, N. H.; Yin, Y. X.; Zhou, L. J.; Guo, Y. G.; Wan, L. J. Smaller Sulfur Molecules Promise Better Lithium-Sulfur Batteries, *Journal of the American Chemical Society* **2012,** 134, (45), 18510-18513.

[156] Xu, Y. H.; Wen, Y.; Zhu, Y. J.; Gaskell, K.; Cychosz, K. A.; Eichhorn, B.; Xu, K.; Wang, C. S. Confined Sulfur in Microporous Carbon Renders Superior Cycling Stability in Li/S Batteries, *Advanced Functional Materials* **2015,** 25, (27), 4312-4320.

[157] Zhang, B.; Qin, X.; Li, G. R.; Gao, X. P. Enhancement of long stability of sulfur cathode by encapsulating sulfur into micropores of carbon spheres, *Energy and Environmental Science* **2010,** 3, (10), 1531-1537.

[158] Ji, L. W.; Rao, M. M.; Zheng, H. M.; Zhang, L.; Li, Y. C.; Duan, W. H.; Guo, J. H.; Cairns, E. J.; Zhang, Y. G. Graphene Oxide as a Sulfur Immobilizer in High Performance Lithium/Sulfur Cells, *Journal of the American Chemical Society* **2011,** 133, (46), 18522-18525.

[159] Stobinski, L.; Lesiak, B.; Kover, L.; Toth, J.; Biniak, S.; Trykowski, G.; Judek, J. Multiwall carbon nanotubes purification and oxidation by nitric acid studied by the FTIR and electron spectroscopy methods, *Journal of Alloy Compounds* **2010,** 501, (1), 77-84.

[160] Zhou, W. D.; Wang, C. M.; Zhang, Q. L.; Abruna, H. D.; He, Y.; Wang, J. W.; Mao, S. X.; Xiao, X. C. Tailoring Pore Size of Nitrogen-Doped Hollow Carbon Nanospheres for Confining Sulfur in Lithium-Sulfur Batteries, *Advanced Energy Materials* **2015,** 5, (16).

[161] Yao, H. B.; Yan, K.; Li, W. Y.; Zheng, G. Y.; Kong, D. S.; Seh, Z. W.; Narasimhan, V. K.; Liang, Z.; Cui, Y. Improved lithium-sulfur batteries with a conductive coating on the separator to prevent the accumulation of inactive S-related species at the cathode-separator interface, *Energy & Environmental Science* **2014,** 7, (10), 3381-3390.

[162] He, B.; Li, W.-C.; Yang, C.; Wang, S.-Q.; Lu, A.-H. Incorporating Sulfur Inside the Pores of Carbons for Advanced Lithium–Sulfur Batteries: An Electrolysis Approach, *ACS Nano* **2016,** 10, (1), 1633-1639.

[163] Sun, L.; Li, M.; Jiang, Y.; Kong, W.; Jiang, K.; Wang, J.; Fan, S. Sulfur nanocrystals confined in carbon nanotube network as a binder-free electrode for high-performance lithium sulfur batteries, *Nano Letters* **2014,** 14, (7), 4044-4049.

[164] Evers, S.; Nazar, L. F. Graphene-enveloped sulfur in a one pot reaction: a cathode with good coulombic efficiency and high practical sulfur content, *Chemical Communications* **2012,** 48, (9), 1233-1235.

[165] Wang, Y.; Chen, L.; Scudiero, L.; Zhong, W. H. The beauty of frost: nano-sulfur assembly via low pressure vapour deposition, *Chemical Communications* **2015,** 51, (88), 15967-15970.

[166] Cui, Y.; Wu, M.; Scott, C.; Xie, J.; Fu, Y. A binder-free sulfur/carbon composite electrode prepared by a sulfur sublimation method for Li–S batteries, *RSC Advances* **2016,** 6, 52642-52645.

[167] Evers, S.; Nazar, L. F. New Approaches for High Energy Density Lithium Sulfur Battery Cathodes, *Accounts of Chemical Research* **2012,** 46, (5), 1135-1143.

[168] Meyer, B. Elemental sulfur, *Chemical Reviews* **1976,** 76, (3), 367-388.

[169] Li, J.; Armstrong, B. L.; Daniel, C.; Kiggans, J.; Wood, D. L. Optimization of multicomponent aqueous suspensions of lithium iron phosphate (LiFePO 4) nanoparticles and carbon black for lithium-ion battery cathodes, *Journal of Colloid and Interface Science* **2013,** 405, 118-124.

[170] Chen, H.; Qiu, X.; Zhu, W.; Hagenmuller, P. Synthesis and high rate properties of nanoparticled lithium cobalt oxides as the cathode material for lithium-ion battery, *Electrochemistry Communications* **2002,** 4, (6), 488-491.

[171] Yu, S. H.; Lee, B.; Choi, S.; Park, S.; Hong, B. H.; Sung, Y. E. Enhancement of electrochemical properties by polysulfide trapping in a graphene-coated sulfur cathode on patterned current collector, *Chemical Communications* **2016,** 52, (15), 3203-3206.

[172] Li, Z.; Huang, Y. M.; Yuan, L. X.; Hao, Z. X.; Huang, Y. H. Status and prospects in sulfur-carbon composites as cathode materials for rechargeable lithium-sulfur batteries, *Carbon* **2015,** 92, 41-63.

[173] Wang, D.-W.; Zeng, Q.; Zhou, G.; Yin, L.; Li, F.; Cheng, H.-M.; Gentle, I. R.; Lu, G. Q. M. Carbon–sulfur composites for Li–S batteries: status and prospects, *Journal of Materials Chemistry A* **2013,** 1, (33), 9382-9394.

[174] Wang, Z.; Dong, Y.; Li, H.; Zhao, Z.; Wu, H. B.; Hao, C.; Liu, S.; Qiu, J.; Lou, X. W. D. Enhancing lithium–sulphur battery performance by strongly binding the discharge products on amino-functionalized reduced graphene oxide, *Nature Communications* **2014,** 5.

[175] Li, X.; Cao, Y.; Qi, W.; Saraf, L. V.; Xiao, J.; Nie, Z.; Mietek, J.; Zhang, J.-G.; Schwenzer, B.; Liu, J. Optimization of mesoporous carbon structures for lithium–sulfur battery applications, *Journal of Materials Chemistry* **2011,** 21, (41), 16603-16610.

[176] Sun, F.; Wang, J.; Chen, H.; Li, W.; Qiao, W.; Long, D.; Ling, L. High efficiency immobilization of sulfur on nitrogen-enriched mesoporous carbons for Li–S batteries, *ACS Applied Materials & Interfaces* **2013,** 5, (12), 5630-5638.

[177] Zhang, L.; Ji, L.; Glans, P.-A.; Zhang, Y.; Zhu, J.; Guo, J. Electronic structure and chemical bonding of a graphene oxide–sulfur nanocomposite for use in superior performance lithium–sulfur cells, *Physical Chemistry Chemical Physics* **2012,** 14, (39), 13670-13675.

[178] Kim, J. W.; Ocon, J. D.; Kim, H. S.; Lee, J. Improvement of Energy Capacity with Vitamin C Treated Dual-Layered Graphene–Sulfur Cathodes in Lithium–Sulfur Batteries, *ChemSusChem* **2015,** 8, (17), 2883-2891.

[179] Park, J.; Moon, J.; Kim, C.; Kang, J. H.; Lim, E.; Park, J.; Lee, K. J.; Yu, S.-H.; Seo, J.-H.; Lee, J. Graphene quantum dots: structural integrity and oxygen functional groups for high sulfur/sulfide utilization in lithium sulfur batteries, *NPG Asia Materials* **2016,** 8, (5), e272.

[180] Liu, J.; Li, W.; Duan, L.; Li, X.; Ji, L.; Geng, Z.; Huang, K.; Lu, L.; Zhou, L.; Liu, Z. A Graphene-like Oxygenated Carbon Nitride Material for Improved Cycle-Life Lithium/Sulfur Batteries, *Nano Letters* **2015,** 15, (8), 5137-5142.

[181] Li, R.; Zhang, M.; Li, Y.; Chen, J.; Yao, B.; Yu, M.; Shi, G. Mildly reduced less defective graphene oxide/sulfur/carbon nanotube composite films for high-performance lithium–sulfur batteries, *Physical Chemistry Chemical Physics* **2016,** 18, (16), 11104-11110.

[182] Song, J.; Xu, T.; Gordin, M. L.; Zhu, P.; Lv, D.; Jiang, Y. B.; Chen, Y.; Duan, Y.; Wang, D. Nitrogen-Doped Mesoporous Carbon Promoted Chemical Adsorption of Sulfur and Fabrication of High-Areal-Capacity Sulfur Cathode with Exceptional Cycling Stability for Lithium-Sulfur Batteries, *Advanced Functional Materials* **2014,** 24, (9), 1243-1250.

[183] Song, J.; Gordin, M. L.; Xu, T.; Chen, S.; Yu, Z.; Sohn, H.; Lu, J.; Ren, Y.; Duan, Y.; Wang, D. Strong Lithium Polysulfide Chemisorption on Electroactive Sites of Nitrogen-Doped Carbon Composites For High-Performance Lithium–Sulfur Battery Cathodes, *Angewandte Chemie International Edition* **2015,** 54, (14), 4325-4329.

[184] Wu, W.; Zhao, Y.; Wu, C.; Guan, L. Single-walled carbon nanohorns with unique horn-shaped structures as a scaffold for lithium–sulfur batteries, *RSC Advances* **2014,** 4, (54), 28636-28639.

[185] Bergin, S. D.; Nicolosi, V.; Streich, P. V.; Giordani, S.; Sun, Z.; Windle, A. H.; Ryan, P.; Niraj, N. P. P.; Wang, Z. T. T.; Carpenter, L. Towards Solutions of Single-Walled Carbon Nanotubes in Common Solvents, *Advanced Materials* **2008,** 20, (10), 1876-1881.

[186] Oakes, L.; Hanken, T.; Carter, R.; Yates, W.; Pint, C. L. Roll-to-roll nanomanufacturing of hybrid nanostructures for energy storage device design, *ACS Applied Materials & Interfaces* **2015,** 7, (26), 14201-14210.

[187] Kaban, I.; Nowak, R.; Bruzda, G.; Xi, L.; Sobczak, N.; Eckert, J.; Giebeler, L. Wettability and work of adhesion of liquid sulfur on carbon materials for electrical energy storage applications, *Carbon* **2016,** 98, 702-707.

[188] Picher, M.; Anglaret, E.; Arenal, R.; Jourdain, V. Self-deactivation of single-walled carbon nanotube growth studied by in situ Raman measurements, *Nano Letters* **2009,** 9, (2), 542-547.